DTU Library

CFD Modeling of Non-Neutral Atmospheric Boundary Layer Conditions

Koblitz, Tilman

Publication date:
2013

Document Version
Publisher's PDF, also known as Version of record

[Link back to DTU Orbit](#)

Citation (APA):
Koblitz, T. (2013). *CFD Modeling of Non-Neutral Atmospheric Boundary Layer Conditions*. DTU Wind Energy. DTU Wind Energy PhD No. 0019(EN)

CFD Modeling of Non-Neutral Atmospheric Boundary Layer Conditions

Tilman Koblitz

Author (s): Tilman Koblitz

Title: CFD Modeling of Non-Neutral Atmospheric Boundary Layer Conditions

Department: Department of Wind Energy

Summary (max 2000 characters):

For wind resource assessment, the wind industry is increasingly relying on Computational Fluid Dynamics models that focus on modeling the airflow in a neutrally stratified surface-layer. Physical processes like the Coriolis force, buoyancy forces and heat transport, that are important to the atmospheric boundary-layer, are mostly ignored so far.

In order to decrease the uncertainty of wind resource assessment, the present work focuses on atmospheric flows that include atmospheric stability and the Coriolis effect.

Within the present work a RANS model framework is developed and implemented into the DTU Wind Energy flow solver EllipSys3D.

The high Reynolds number flows considered in this work are based on the solution of the Reynolds-Averaged Navier-Stokes equations. Together with a two-equation closure method the flow within the whole boundary-layer can be computed at a much lower computational cost than e.g. using large-eddy simulations.

The developed ABL model is successfully validated using a range of different test cases with increasing complexity. Data from several large scale field campaigns, wind tunnel experiments, and previous numerical simulations is presented and compared against model results. A method is developed how to simulate the time-dependant non-neutral ABL flow over complex terrain: a precursor simulation is used to specify unsteady inlet boundary conditions on complex terrain domains.

The advantage of the developed RANS model framework is its general applicability. All implementations in the ABL model are tuning free, and except for standard site specific input parameters, no additional model coefficients need to be specified before the simulation. In summary the results show that the implemented modifications are applicable and reproduce the main flow characteristics of neutral and non-neutral ABL flow. The developed ABL model significantly improves the predicted flow fields over both flat and complex terrain, when compared against neutral models and measurements.

Summary (English)

For wind resource assessment, the wind industry is increasingly relying on Computational Fluid Dynamics models that focus on modeling the airflow in a neutrally stratified surface-layer. Physical processes like the Coriolis force, buoyancy forces and heat transport, that are important to the atmospheric boundary-layer, are mostly ignored so far. In order to decrease the uncertainty of wind resource assessment, the present work focuses on atmospheric flows that include atmospheric stability and the Coriolis effect. Within the present work a RANS model framework is developed and implemented into the DTU Wind Energy flow solver EllipSys3D.

The high Reynolds number flows considered in this work are based on the solution of the Reynolds-Averaged Navier-Stokes equations. Together with a two-equation closure method the flow within the whole boundary-layer can be computed at a much lower computational cost than e.g. using large-eddy simulations.

The developed ABL model is successfully validated using a range of different test cases with increasing complexity. Data from several large scale field campaigns, wind tunnel experiments, and previous numerical simulations is presented and compared against model results. A method is developed to simulate the time-dependant non-neutral ABL flow over complex terrain: a precursor simulation is used to specify unsteady inlet boundary conditions on complex terrain domains.

The advantage of the developed RANS model framework is its general applicability. All implementations in the ABL model are tuning free, and except for standard site specific input parameters, no additional model coefficients need to

be specified before the simulation. In summary, the results show that the implemented modifications are applicable and reproduce the main flow characteristics of neutral and non-neutral ABL flow. The developed ABL model significantly improves the predicted flow fields over both flat and complex terrain, when compared against neutral models and measurements.

Summary (Danish)

Vindmølleindustrien benytter i stigende grad Computational Fluid Dynamics modeller til vind ressourcevurderinger; men de er typisk begrænset til at modellere vinden i det neutrale atmosfæriske grænselag. Hidtil er vigtige atmosfæriske processer som Coriolis kraft, termiske effekter og varmetransport, blevet ignoreret i de fleste modeller. For at mindre usikkerheden ved vind ressourcevurderinger, fokuserer det nuværende arbejde på atmosfærisk vinde der inkluderer stabilitet og Coriolis effekter. For at undersøge indflydelsen af disse effekter er der blevet udviklet en RANS model ramme, og de udviklede modeller er blevet implementeret i DTU Vindenergi CFD løser EllipSys3D. På grund af de høje Reynolds tal er beregningerne baseret på RANS ligningerne. Sammen med en to-lignings turbulens model kan vinden i hele det atmosfæriske grænselag beregnes for meget lavere beregningsmæssige omkostninger end for eksempelvis med LES.

Den udviklede ABL model er med succes valideret for en række forskellige testcases af stigende kompleksitet. Data fra flere målekampagner, vindtunnel eksperimenter, og tidligere numeriske simuleringer præsenteres og sammenlignes med modelresultater. En metode til at simulere den tidsafhængige ikke-neutrale atmosfæriske vind over komplekst terræn er udviklet: en indledende simulering bruges til at bestemme de tidsafhængige indløbsbetingelser, der benyttes til simulering af det komplekse terræn.

Fordelen ved den præsenterede RANS model er dens generelle anvendelighed. Alle implementeringer i modellen er tuning fri, og med undtagelse af standard input parametre behøves der ingen yderligere model koefficienter. Sammenfattende viser resultaterne, at de vigtigste karakteristika for både neutrale og ikke-

neutral atmosfæriske vinde kan simuleres med de gennemførte ændringer. Den udviklede model forbedrer de forudsagte strømningsfelter over fladt og komplekst terræn, når man sammenligner mod neutrale modeller og målinger.

Preface

This thesis was prepared mainly at the department of Wind Energy at the Technical University of Denmark (DTU), and partially at the National Renewable Energy Centre (CENER) in Pamplona, Spain, in fulfilment of the requirements for acquiring the Ph.D. degree. The work as a whole is unpublished, and was carried out by the author, T. Koblitz, under the supervision of Prof. N. Sørensen and Senior scientists A. Bechmann and A. Sogachev.

The central goal of the work was to implement the effect of atmospheric stability into the existing in-house CFD code EllipSys3D. All necessary modifications to the solver were implemented independently by the author. The implementation of the energy equation, that was available from previous work, was validated and tested for its applicability using a standard CFD test case (see appendix). Throughout the work, different turbulence models have been implemented and tested by the author (Apsley and Castro, 1997; Sogachev and Panferov, 2006; Sogachev et al., 2012), which finally led to the choice of the turbulence closure developed by Sogachev et al. (2012).

Several numerical issues connected to the implementation of the turbulence model and the energy equation had to be resolved. Minimum (ambient) values for the turbulence variables are imposed in order to improve convergence and to prevent eddy viscosity values close to or even below zero. The implementation and the choice of the ambient turbulence values was done by the author. The buoyancy volume forces are treated using an algorithm for allocating discrete forces to avoid pressure/velocity oscillations, which was developed and implemented by Réthoré and Sørensen (2012).

Additionally to the model modifications, a method was developed to simulate

transient non-neutral ABL flows over complex terrain. This computational procedure determines transient boundary conditions from precursor simulations, and enables to simulate non-neutral ABL flows efficiently at relatively low computational cost. The method was developed and implemented independently by the author.

The experimental dataset of the Benakanahalli field campaign, that was used for model validation, was available from a database. All data selection, filtering and post-processing of the measurements was done by the author.

Parts of the work have been published in conference proceedings and in a scientific journal:

- Parts of chapter 4 and section 4.3 have been published in a peer-reviewed conference paper (Koblitz et al., 2012c)

- Section 8.1 has been published in a conference paper (Koblitz et al., 2010)

- Section 4.4 has been similarly published in a conference poster (Koblitz et al., 2012b)

- Sections 4, 4.4 and 5.1 are part of a research article that has been accepted for publication in the Wind Energy journal

- Preliminary measurement results from section 5.2.2 have been published in a conference poster (Berg et al., 2012)

- Section 5.2.3.2 has been published in a peer-reviewed conference paper (Koblitz et al., 2012a)

Roskilde, 21-October-2013

Tilman Koblitz

Acknowledgements

Contents

List of Figures

List of Tables

Nomenclature

Abbreviations

ABL   atmospheric boundary-layer

ASL   atmospheric surface-layer

CFD   computational fluid dynamics

DTU   Denmark's Technical University

LDC   lid-driven cavity

LES   large-eddy simulation

MOST   Monin-Obukhov similarity theory

RANS   Reynolds-Averaged Navier-Stokes

Roman Symbols

B	buoyancy source/sink term for k-ϵ turbulence model	$[\frac{\text{m}}{\text{s}^3}]$
c_p	specific heat capacity of air at a constant pressure	$[\frac{\text{J}}{\text{K}}]$
$C_{\epsilon 1}$	model coefficient for k-ϵ turbulence model	[-]
$C_{\epsilon 1}^*$	modified $C_{\epsilon 1}$ model coefficient	[-]
$C_{\epsilon 2}$	model coefficient for k-ϵ turbulence model	[-]
$C_{\epsilon 3}$	model coefficient for k-ϵ turbulence model	[-]
C_μ	model coefficient for k-ϵ turbulence model	[-]

D	diffusion term for k-ϵ turbulence model	$[\frac{\text{m}}{\text{s}^3}]$
f_c	Coriolis parameter	$[\frac{\text{rad}}{\text{s}}]$
Fr	Froude number	[-]
G	geostrophic wind speed	$[\frac{\text{m}}{\text{s}}]$
g_i	gravitational acceleration	$[\frac{\text{m}}{\text{s}^2}]$
H	heat flux	$[\frac{\text{W}}{\text{m}^2}]$
h	height of terrain or obstacle	[m]
k	turbulent kinetic energy	$[\frac{\text{m}}{\text{s}^2}]$
L	Obukhov length	[m]
l	mixing length scale	[m]
l_0	maximum global turbulent mixing length scale for neutral ABL	[m]
l_e	maximum global turbulent mixing length scale	[m]
l_t	local turbulent mixing length scale	[m]
l_{MY}	maximum global turbulent mixing length scale for non-neutral ABL	[m]
M	molar mass	$[\frac{\text{g}}{\text{mol}}]$
N_{bv}	Brunt–Väisälä frequency	$[\frac{1}{\text{s}}]$
P	pressure	[Pa]
P_0	atmospheric standard pressure	[Pa]
P_k	rate of shear production of k	$[\frac{\text{m}}{\text{s}^3}]$
Pr	Prandtl number	[-]
R	universal gas constant	$[\frac{\text{J}}{\text{molK}}]$
Re	Reynolds number	[-]
Ri_b	Richardson number	[-]
Ri_g	gradient Richardson number	[-]
S_θ	volume heat source	$[\frac{\text{kgK}}{\text{sm}^3}]$
S_v	volume force	[N]
T	temperature	[K]

t	time	[s]
u, v, w	wind speed compoment along x,y,z	$[\frac{\text{m}}{\text{s}}]$
u_*	friction velocity	$[\frac{\text{m}}{\text{s}}]$
u_G	geostrophic wind component in x-direction	$[\frac{\text{m}}{\text{s}}]$
U_i	mean wind speed components	$[\frac{\text{m}}{\text{s}}]$
v_G	geostrophic wind component in y-direction	$[\frac{\text{m}}{\text{s}}]$
x, y, z	Cartesian coordinates	[m]
x_i	space coordinates	[m]
z_0	roughness length	[m]
$\hat{P}$	pressure in which the hydrostatic pressure is absorbed	[Pa]

Greek Symbols

α	empirical constant for length scale determination	[-]
α_B	stability-related turbulence model coefficient	[-]
Δ	error	[-]
δ_m	empirical coefficient from MOST	[-]
ϵ	dissipation	$[\frac{\text{m}}{\text{s}^3}]$
Γ_d	dry adiabatic lapse rate	$[\frac{\text{K}}{\text{m}}]$
Γ_m	moist adiabatic lapse rate	$[\frac{\text{K}}{\text{m}}]$
γ_m	empirical coefficient from MOST	[-]
κ	van Karman constant	[-]
λ	latitude	[rad]
μ	dynamic viscosity	$[\frac{\text{Ns}}{\text{m}^2}]$
μ_t	turbulent eddy viscosity	$[\frac{\text{Ns}}{\text{m}^2}]$
Ω	vorticity	$[\frac{1}{\text{s}}]$
Ω_E	earth's rotation rate	$[\frac{\text{rad}}{\text{s}}]$
ϕ	numerical residual	[-]
ϕ_m	stability function from MOST	[-]

Ψ	stream function	$[\frac{\text{m}}{\text{s}}]$
Ψ_m	stability function from MOST	$[\text{-}]$
ρ	air density	$[\frac{\text{kg}}{\text{m}^3}]$
ρ_o	reference air density	$[\frac{\text{kg}}{\text{m}^3}]$
σ_ϵ	Schmidt number for ϵ	$[\text{-}]$
σ_θ	turbulent Prandtl number	$[\text{-}]$
σ_k	Schmidt number for k	$[\text{-}]$
τ	shear stress	$[\text{Pa}]$
θ	potential temperature	$[\text{K}]$
ζ	dimensionless height from MOST	$[\text{-}]$

Sub- and superscripts

$'$	fluctuating part of a quantity
0	surface value
$1, 2, 3$	longitudinal, lateral and vertical directions
ϵ	parameters associated to dissipation rate ϵ
k	parameters associated to turbulent kinetic energy k
t	turbulent property

Introduction

1.1 Motivation

For many applications knowledge about the flow properties within the atmospheric boundary-layer (ABL) are important. They range from engineering (loads on buildings, bridges, vehicles or other structures) to atmospheric sciences (pollutant transport, gas dispersion, urban climate, weather prediction). In the field of wind energy, information about the wind field is crucial to design wind turbines and to estimate their power production. During the process of wind resource assessment the on-site wind power potential of a wind turbine or a wind farm is estimated, and the accuracy of this process is crucial for the successful development of a wind farm. The wind flow at a given site can vary considerably in space due to changes of the topography. Especially in complex terrain (hills, mountains, escarpments) and for roughness changes (height of vegetation or buildings) the wind can significantly change in direction and magnitude, and turbulence levels can vary greatly. Therefore site-specific information of the wind field is needed. Traditionally, measurement campaigns at full scale are conducted to gather information on the flow field. Theoretical and empirical relations exist only for simplified flows, and are of limited value for real world scenarios, since the underlying assumptions are only met for idealized cases. Also, wind tunnel experiments can usually not satisfactorily reproduce the wind flow across a potential wind farm site with an extent

of several kilometers. Therefore on-site measurements are needed to assess the wind resource, but are kept to a minimum due to the high cost. To supplement measurements wind flow modeling can be used to extrapolate the flow field to locations where poor or no measurements were taken. Modeling the air flow across a site makes it possible to get an insight into the flow behavior at a high resolution, and certain parameters can be studied under controlled conditions, while during measurement campaigns different effects are mostly superimposed. Once properly validated, these so called microscale models can be generally applied for various topographies at a fraction of the cost and time that a full scale field campaign requires. Today, wind flow modeling software is widely used for wind resource assessment, and mostly based on either the linear approach like e.g. WAsP (Mortensen et al., 2005) or the Computational Fluid Dynamics (CFD) approach. They focus primarily on modeling of the neutrally stratified atmospheric surface-layer (ASL) which typically covers the bottom 10% of the atmospheric boundary-layer (ABL). Here the logarithmic wind profile is a justified approximation and the models account for the effects of roughness and topography changes. Atmospheric stability and Coriolis effects are mostly ignored, or like in WAsP are treated as small perturbations to the neutral background flow that can be added after solving the model equations (see section 1.2 for more).

In order to decrease the uncertainty of predictions, it is necessary to describe all relevant physical processes in the whole ABL appropriately. This is especially relevant in complex terrain, where the ABL flow is highly variable depending on the location. Any atmospheric process that occurs within the area of interest and influences the on-site wind conditions should be accounted for. Instead of adding these effects as corrections to the model solution, they should ideally be included within the model equations. The influences of Coriolis force and atmospheric stability have been identified as highly relevant for the wind flow in the ABL. The aim of this work is to develop and validate a Reynolds-Averaged Navier-Stokes (RANS) ABL model framework describing the whole ABL that can be applied for neutral and non-neutral flows over complex terrain and captures the influences of the Coriolis force and varying atmospheric stabilities.

The next section briefly summarizes the physics within the ABL. Basic physical processes and the vertical structure of the ABL are presented. The following sections explain the background of the present study and give an overview of previous work available in literature.
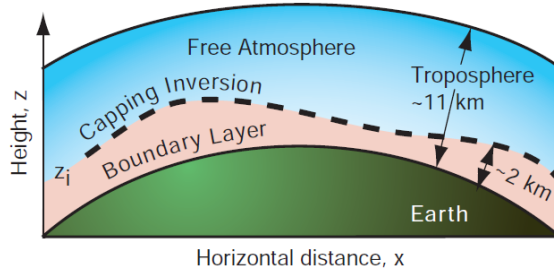
Figure 1.1: Vertical structure of the earth's atmosphere. The lowest portion is directly influenced by the earth's surface, and is separated from the rest of the troposphere by a capping inversion. Figure taken from (Wallace and Hobbs, 2006).

1.1.1   The atmospheric boundary-layer

The ABL is defined as the portion of the atmosphere that is influenced by the earth's surface. The air flow within the ABL adapts to the varying conditions at the surface where turbulence is effective at communicating the drag from the ground throughout the entire ABL. The ABL typically responds to changes in surface forcing at a time scale of about one hour or less (Stull, 1988; Wallace and Hobbs, 2006). The resulting thickness and the vertical structure of the ABL is therefore variable in space and time as seen in figure 1.1 and 1.2.

The ABL typically occupies the bottom 10-20% of the troposphere (Wallace and Hobbs, 2006) and ranges from tens of meters up to 3 km or more (often defined as the height where turbulence drops to small values, e.g. 5% of the surface value). The ABL is separated into two regions: the atmospheric surface-layer (ASL) close to the ground and a region above. Typically the ASL occupies about 10% of the ABL (see also section 4.5.1). In the ASL steep vertical gradients of the wind speeds and temperature are present and the vertical structure is mainly governed by surface friction and the vertical temperature gradient. Heat and momentum fluxes are approximately constant and the Coriolis force is negligible.

Above the ASL the air flow is still influenced by the earth's surface, but vertical gradients of wind speed and temperature typically decrease compared to in the ASL. Coriolis effects become increasingly important and lead to a turning of the wind with height.

Above the ABL the temperature typically increases, which is known as a temperature or capping inversion that is separating the ABL from the rest of the troposphere above.
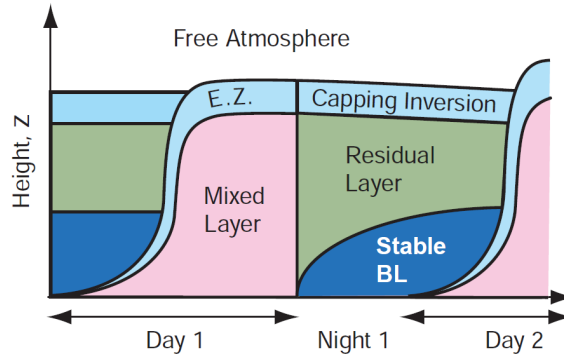
Figure 1.2: Typical evolution of the vertical ABL structure during fair weather
conditions over land in summer. E.Z.: entrainment zone. Figure
taken from (Wallace and Hobbs, 2006).

During fair-weather conditions over land (no precipitation, no clouds, moderate
wind speeds), the ABL changes continuously during day and night. This diurnal
(daily) cycle of variations is induced by alternating heating and cooling of the
earth's surface: incoming solar radiation heats the ground during daytime, and
emitted longwave radiation cools the ground at night. The turbulent wind field
quickly adapts and evolves in response to the changing conditions, and figure 1.2
shows the typical evolution of the ABL during fair weather conditions over
rough flat ground in summer (Wallace and Hobbs, 2006). Some distinct states
can be defined: conditions when the surface is warmer than the surrounding
air are called unstable (typically during daytime), while they are called stable
when the surface is colder than the air (typically during nighttime). Conditions
where the potential temperature is constant with height are called neutral (see
section 1.3-1.4). During unstable conditions at daytime heated air rises from
the warm surface, enhancing the production of turbulence, and results in a
well mixed layer (called mixed layer or convective boundary-layer). The ABL
continuously grows throughout the day due to buoyancy forces and increased
turbulent mixing, which leads to a process called entrainment: the capping
inversion is not a solid boundary, and the rising thermals can overshoot a small
distance into the inversion, and due to the strong convective turbulence, air
parcels from above are mixed into the mixed layer (this area is called entrainment
zone). The maximum ABL height is reached at late afternoon and for a short
period the ABL is neutrally stratified.

Shortly after sunset the declining surface temperatures start to form a shallow
stable layer close to the ground (called the nocturnal boundary-layer), while
above the nearly neutral layer from late afternoon (now called the residual layer)
still exists with the capping inversion on top. Within the nocturnal boundary-
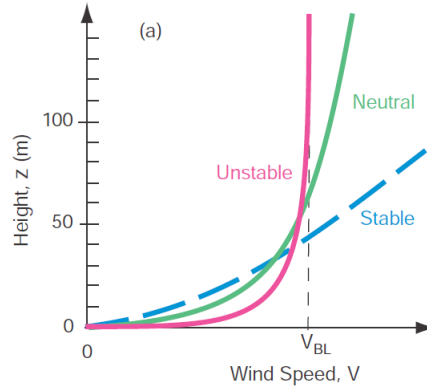
Figure 1.3: Typical variation of wind speed with atmosperic stability: wind
profiles for neutral, stable and unstable conditions are shown. Fig-
ure taken from (Wallace and Hobbs, 2006).

layer turbulence production is suppressed and cold air sinks to the ground.
During the night the nocturnal boundary-layer increases slowly with height but
is significantly shallower than the mixed layer during daytime. At the end of
the night when the sun rises again, unstable conditions close to the ground will
quickly erode the nocturnal inversion above and the cycle repeats itself day after
day as long as the weather remains fair.

Close to the ground the wind speeds respond quickly to the changing surface
conditions that occur throughout the day. Generally, the wind profile is assumed
to be nearly logarithmic (based on similarity theory; see section 4.5.1), and wind
speeds reduce to zero at the ground due to friction. However, due to atmospheric
stability, the wind profile can deviate significantly from the logarithmic profile
that is a valid approximation during neutral conditions only. Figure 1.3 shows
typical wind profiles for neutral, stable and unstable conditions. During unstable
conditions, high turbulence levels are effective in mixing momentum downward
to the ground, where the wind speeds increase rapidly with height. Further away
from the surface, the flow is well-mixed which results in small vertical gradients
and a flat wind profile. Stable conditions, on the other hand, are characterized
by low turbulence levels. Here the drag from the ground is not communicated
through the surface-layer, which leads to less mixing and an increase in wind
shear. More details about the interplay of temperature, turbulence and wind
speed are given in chapter 4.

1.2   Literature review of existing ABL models

The present section gives an overview of the history and the state of the art in numerical modeling of ABL flows. The focus is on microscale numerical modeling for micrositing purposes and its importance for wind resource assessment. The present review does not claim to be a exhaustive description of all methodologies and models available. It rather gives an overview over the most commonly used models and focuses on describing their capabilities and limitations.

To get a complete description of the spatial and temporal variability of the wind field, measurements are increasingly supplemented by advanced numerical flow models. The development of models dedicated to wind resource assessment has now been going on for three decades, starting with the development of linear models by Walmsley et al. (1986) and Troen et al. (1987). This approach has the potential to significantly lower the costs for wind resource assessment, since installing and operating meteorological masts is expensive and can only be done at selected positions, which is especially relevant in complex terrain (Berge et al., 2006).

Atmospheric processes take place on a scale from less than a centimeter up to several kilometers or even hundreds or thousands of kilometers. To model ABL flows, atmospheric processes need to be parameterized and translated into model equations that can be solved numerically. Depending on the application, certain scales are more relevant than others, and modeling approaches for ABL flows differ significantly. They can roughly be divided in two categories: microscale engineering models and mesoscale meteorological models. They both have an equally long history (Schonfeld, 1980; Anthes et al., 1982), and all of the models have limitations that restrict their applicability. Typical inputs for the models are the terrain topography and the surface roughness. Together with observational data the wind resource can then be estimated in areas where no measurements were taken.

On larger scales, mesoscale weather prediction models represent a well established methodology to simulate a broad range of meteorological phenomena over wide areas of the earth's surface (see Yamada and Koike (2011) for a list). Together with global datasets from satellite observations and climatological data collected by measurement stations, they are increasingly being used for regional wind resource assessment, especially for offshore locations (see Bergström (2001) or Badger et al. (2006) for examples and Sempreviva et al. (2008) for a review). This approach allows the assessment of the wind resource over large areas.

When a promising location for a future wind farm is determined, a more detailed investigation of the wind resource on a local scale has to be carried out. Here

microscale models are extensively being used. Microscale modeling typically focuses on scales up to around 20 km. Micrositing is particular relevant in complex terrain, where the wind resource greatly varies spatially and the resulting wind field is highly three dimensional. To resolve these effects, more and more sophisticated flow models are being developed.

Models for micrositing can roughly be divided into linearized and full CFD models (see Probst and Cárdenas (2010) for a review). Linear models provide simplified steady-state solutions of the linearized versions of the Navier-Stokes equations. Most such models are based on the theory of Jackson and Hunt (1975), and more details are given in Troen and Petersen (1989). The two most popular microscale modeling products are WAsP (Troen and Petersen, 1989) and MS3DJH/Ms-Micro (Walmsley et al., 1986; Taylor et al., 1983). Similar products available in the market are for example the WindFarm package from ReSoft, where MsMicro is implemented (Kiranoudis et al., 2001), WinPRO from EMD (uses wind flow modeling inputs from WAsP or CFD), WindFarmer from GL Garrad Hassan (also uses modeling inputs from WAsP) or MSFD (Beljaars et al., 1987). These models are very popular due to the moderate complexity of necessary model inputs and their fast execution times. Due to the linearization of the governing equations, these models are not well suited for calculating the flow field in highly complex terrain (Walmsley et al., 1986), and their applicability is limited to areas with gentle terrain slopes below 25 % (Probst and Cárdenas, 2010). However, simple terrain corrections, so called RIX-analysis (Mortensen et al., 2006), have been applied with success to the WAsP simulation for quite complicated terrain. Although these models have limitations, they are capable of providing good and robust results if applied correctly.

In recent years, full CFD models are increasingly being used in wind engineering to study a wide variety of processes in the ABL (Sørensen, 1995; Castro et al., 2003; Undheim et al., 2006; Blocken et al., 2007; Hargreaves and Wright, 2007; Yang et al., 2008; Beaucage et al., 2012). Full 3-D CFD modeling allows the flow to be modeled more realistically compared to linear models, especially for very complex terrain where non-linear effects become significant. CFD models can handle flow separation, give important information about the turbulent kinetic energy field and resolve unsteadiness (Probst and Cárdenas, 2010).

Most CFD models are based on the RANS equations, where all turbulence is modeled. Several commercial CFD packages are available and widely used. General purpose CFD packages are capable of modeling flows of interest for wind energy. Examples are Star-CCM+ (CD-adapco, 2006), Fluent (ANSYS, 2011) or CFX (ANSYS, 2010) for commercial packages and OpenFOAM that provides an open source simulation platform (OpenFOAM-Foundation, 2013). In practice, a lot of effort has to be put in the setup of the simulation and the extraction of the results. As a result, numerous CFD tools specific to the analysis of wind

flows for wind resource assessment have been developed. WindSim (Gravdahl and Harstveit, 2000), Meteodyn (Clarenc et al., 2007) or VENTOS (Castro et al., 2003; Maurizi et al., 1998), for example, provide tools specific to wind flow over terrain, where topographical input information can be combined with wind data. WindSim was among the first commercial CFD models available for micrositing.

To get a more accurate solution of the turbulent flow field, Large-Eddy Simulations (LES) are increasingly used in atmospheric research (Basu and Porté-Agel, 2006). LES is solved unsteady and resolves large turbulent eddies, while only modeling small turbulent eddies using a subgrid-scale model. This represents a promising approach, but it is at least one order of magnitude more computationally expensive compared to RANS and still relatively immature.

1.3   Literature review of RANS modeling of ABL flows

This section gives an overview of how the physics and dynamics of turbulent ABL flow are modeled using CFD. The literature review is mostly limited to the RANS approach, with special focus on the different turbulence parametrizations that are being used among modelers.

Turbulence modeling represents a major challenge in CFD, and a large number of turbulence models have been developed. Different approaches exist, and they range from simple first-order to more complex higher order models. Higher order models are able to simulate the turbulence quantities more accurately, but are computationally more expensive (Wyngaard et al., 1974; Launder et al., 1975). Additionally, the values of required constants lack agreement in existing literature (Wichmann and Schaller, 1986; Sogachev et al., 2012). When detailed knowledge of higher order turbulence statistics is not important, simpler turbulence closures can represent a good compromise between computational cost and accuracy. The most popular approach is based on the closure hypothesis proposed by Boussinesq (Schlichting, 1968), who introduced the concept of an eddy viscosity coefficient: unknown second-moment quantities that are not solved in the model equations are parameterized based on the known mean wind gradients. The challenge is to obtain realistic expressions for the eddy viscosity, in order to reproduce atmospheric processes. In order to successfully apply these models to ABL flows, the turbulent length scale, l, must be calculated as a dynamic variable (Ayotte et al., 1999; Finnigan, 2007; Rodi, 1987). Two-equation models which determine the length scale from a transport equation provide such a variable length-scale formulation (Duynkerke, 1988).

One of the most popular two-equation turbulence models is the k-ϵ model (Launder and Spalding, 1974), where two coupled transport equations for the turbulent kinetic energy, k, and the dissipation rate, ϵ, are solved. Over the last three decades different variants of this model have been proposed (see Hargreaves and Wright (2007) for a list, and Stathopoulos (2002) for a review), and the k-ϵ model is widely used in wind engineering models. The availability of meteorological data (Panofsky and Dutton, 1984) makes it possible to calibrate the necessary constants and determine appropriate boundary conditions specific to ABL flow. The performance of the model is largely dependent on the choice of the model constants, and large differences exist in the published literature (Alinot and Masson, 2005). The k-ϵ model has been successfully applied to a range of different applications: wind flow around structures (Blocken et al., 2007; Yang et al., 2008), urban environments (Riddle et al., 2004; Hanna et al., 2006; Thanh et al., 2002; Blocken et al., 2012; Franke et al., 2011), and flow over flat and complex terrain (Sørensen, 1995; Undheim et al., 2006; Huser and Jahre, 1997; Apsley and Castro, 1997; Castro et al., 2003; Parente and Gorlé, 2011; Hargreaves and Wright, 2007). The k-ϵ model has shown a number of well-known deficiencies when applied to ABL flow and many studies emphasize that even for simplified cases of uniformly rough terrain, it is difficult to obtain horizontally homogenous flows (Riddle et al., 2004; Pieterse and Harms, 2013; Hargreaves and Wright, 2007; Yang et al., 2008). Therefore appropriate boundary conditions are very important (Blocken et al., 2007).

ABL simulations documented in literature are often limited to neutrally stratified flows (Wyngaard et al., 1974; Mason and Thomson, 2007; Hargreaves and Wright, 2007; Blocken et al., 2007; Yang et al., 2008). Atmospheric stability, however, can play a significant role (Stull, 1988; Wallace and Hobbs, 2006), and previous simulations of atmospheric and oceanic flows have shown large uncertainties due to stability and vegetation effects (Duynkerke, 1988; Apsley and Castro, 1997; Sogachev and Panferov, 2006; Vendel et al., 2010; Sogachev et al., 2012). However, the implementation of these atmospheric processes are avoided in most microscale models, as neutral steady-state flows are much easier to handle (Meissner et al., 2009; Beaucage et al., 2012).

To consider atmospheric stability, an equation for the conservation of energy has to be included in the model and coupled with the governing equations (Pope, 2000). To account for buoyancy forces, typically the Boussinesq approximation for buoyancy is used, and density variations are introduced only into the gravity terms of the momentum equations (Alinot and Masson, 2005; Meissner et al., 2009; Pontiggia et al., 2009). For more details see section 2.3.1.

The energy equation is often solved in terms of the potential temperature, θ, which is a useful parameter in atmospheric thermodynamics, since it removes the typical rate of change of temperature with height (the adiabatic lapse rate).

This, however, is based on the assumption of dry air. The effect of moisture in the air has an impact on ABL flow: when moist air rises, adiabatic cooling takes place which results in additional heat exchange processes (latent heat) (Lutgens and Tarbuck, 2013). Based on the amount of moisture, a moist adiabatic lapse rate, Γ_m, and a dry adiabatic lapse rate, Γ_d, can be defined. This results in more complex stability criteria: absolutely stable, $(\Gamma < \Gamma_m)$, conditionally stable, $(\Gamma_m < \Gamma < \Gamma_d)$, and absolutely unstable, $(\Gamma_m < \Gamma_d < \Gamma)$. The present work assumes dry air. Additional information on how to account for moisture via an additional equation for water vapour can be found in literature (Thanh et al., 2002; Arya, 2001).

Additionally to buoyancy forces, thermal stratification has a significant impact on the turbulence characteristics in the ABL. The standard k-ϵ model therefore has to be modified to account for the generation and destruction of turbulence due to buoyancy. This is typically done via additional source/sink terms in the two transport equations for k and ϵ. Different approaches exist in the literature, and the formulations of buoyancy related terms and their numerical treatment differ greatly. Rodi (1987) proposes a buoyancy extended k-ϵ model and points out the lack of universality of the standard form of the ϵ equation for stratified flows. Duynkerke (1988) proposes to modify the model constants of the k-ϵ model in order to simulate neutral and stable ABL conditions. Huser and Jahre (1997), however, find that when using this parametrization, turbulence profiles are not maintained and inconsistent with the transport equations in stable conditions, and Vendel et al. (2010) conclude that this is due to the missing buoyancy source terms in the turbulent kinetic energy equation. Wyngaard (1975) and Brost and Wyngaard (1978) present results of stable ABL flows over flat terrain by imposing a constant cooling rate at the surface to obtain quasi-steady conditions. Huser and Jahre (1997) use a similar approach to simulate pollution dispersion in an idealized stable ABL over complex terrain, while neglecting the Coriolis force and buoyancy forces in the momentum equations due to numerical problems connected to the pressure treatment. Apsley and Castro (1997) proposes a new formulation for the closure coefficient, $C_{\epsilon 1}$ (see equation 2.4), specific for ABL flows, that limits the maximum turbulent length-scale, l, determined by the ϵ equation. Thanh et al. (2002) present simulation results of the non-neutral ABL for urban climate simulations including temperature and humidity. Alinot and Masson (2005) present results over uniform flat terrain under various thermal stratifications and neglect the Coriolis effect. Pontiggia et al. (2009) and Freedman and Jacobson (2003) address the problem of inconsistent turbulence profiles, as pointed out by Huser and Jahre (1997), by deriving a formulation that enforces consistency with Monin-Obukhov Similarity Theory (MOST) and modify the coefficient $C_{\epsilon 1}$. The problem of inconsistency has also been stated in other works (Meissner et al., 2009; Pontiggia et al., 2009).

The lack of a consistent formulation of the length scale determining equation

for ϵ has limited the practical use of these kind of closures for many applications (Sogachev et al., 2012), and many different approaches have been suggested in the literature. In recent literature, especially the value for the buoyancy related closure coefficient, $C_{\epsilon 3}$, is unclear, and values range from -4.4 for unstable conditions to 3.4 for stable conditions (Alinot and Masson, 2005; Sogachev et al., 2012; Sogachev and Panferov, 2006).

Several recent works focus on implementing atmospheric stability into CFD solvers following the approaches mentioned above:

- CFX: Huser and Jahre (1997)

- Fluent: Alinot and Masson (2005); Vendel et al. (2010)

- Meteodyn: Texier et al. (2012)

- Star-CCM+: Pieterse and Harms (2013)

- VENTOS: Castro et al. (2008); Ely et al. (2012)

- WindSim: Meissner et al. (2009)

Note that the exact implementation of stability into Meteodyn is unclear from the available literature (Texier et al., 2012). The other attempts rely mostly on the well established MOST (see section 4.5.1 for details). Except for Castro et al. (2008) and Ely et al. (2012) who use a micro-mesoscale model coupling, all of the above studies describe the inlet profiles for wind speed, temperature and turbulence parameters at the boundaries by analytical profiles obtained from MOST (Huser and Jahre, 1997; Meissner et al., 2009; Alinot and Masson, 2005; Vendel et al., 2010; Pieterse and Harms, 2013). Additionally, Alinot and Masson (2005) relate MOST directly to the k-ϵ model by using modified coefficients for C_μ, $C_{\epsilon 1}$ and $C_{\epsilon 3}$, by introducing MOST expressions into the model equations.

Relying on MOST to validate ABL models is popular, but can be problematic, since it is only valid in the surface-layer, and the underlying assumptions of horizontal homogenity and stationarity are only true for idealized cases. Mc-Naughton (2009) points out the differences between ideal conditions required by MOST versus real conditions encountered during field experiments. A recent study by Sogachev et al. (2012) emphasizes that MOST is not applicable for significant amounts of ABL conditions throughout the day, due to the unsteady behavior of the real ABL. In their study, Sogachev et al. (2012) develop a consistent closure method for the k-ϵ model that includes buoyancy and vegetation effects. Contrary to many of the approaches presented earlier, their modeling approach is not relying on MOST and is therefore not limited to homogeneous

surfaces and steady-state ABL conditions. This represents a promising approach to predict non-neutral ABL flows over complex terrain with lower uncertainty, while still being computationally feasible, and their model has therefore been used in the present study.

1.4 The present study

The aim of this work is to develop a RANS ABL model framework that appropriately describes the flow within the whole ABL over complex terrain. Such a numerical tool can help to get a better understanding of the physical processes that are included, like the Coriolis force and atmospheric stability, and eventually aims at reducing uncertainties for wind resource assessment. The starting point for the present study is the existing EllipSys3D flow solver (Michelsen, 1992, 1994; Sørensen, 1995) and its neutral ASL model that is based on the RANS equations and a k-ϵ turbulence model.

As seen in figure 1.2 the vertical structure of the ABL highly depends on the surface conditions that continuously change in time. To simulate this transient behavior, unsteady RANS (URANS) can be used, where the unsteady term is retained in the RANS equations (see chapter 2). Transient RANS together with a two-equation closure method provides the possibility to simulate the unsteady phenomena of a diurnal cycle in the ABL, and is basically the only option besides the more computationally expensive LES approach (Bechmann, 2006).

In a previous study, Sogachev et al. (2012) developed an atmospheric model for flows over flat terrain that accounts for the effects of Coriolis force and atmospheric stability: the energy equation in terms of the potential temperature is solved parallel to the RANS equations and a consistent two-equation turbulence model is used to close the equations. Following his work the present study focuses on developing, implementing and validating an ABL model for the finite-volume flow solver EllipSys3D that uses curvilinear coordinates, which provides the possibility to model complex terrain.

To simulate the flow within the ABL simplifications are necessary. For microscale models the computational domain is typically in the range of several kilometers. For the present study a typical domain is about 30 km in the horizontal direction and up to around 7 km in the vertical direction. Atmospheric processes on greater scales can therefore not be captured (for more see chapter 7). The flow is driven by a pressure gradient that is constant in space and time and that is applied throughout the whole computational domain. On the ABL top, where the Coriolis force and the pressure gradient force are in balance,

this results in a constant geostrophic wind speed. In reality, the geostrophic wind is difficult to determine and never perfectly constant neither in space nor time. This has to be kept in mind when comparing numerical and experimental results (see section 4.4).

The turbulence within the ABL covers a wide range of scales (from less than a cm up to several km). Resolving all turbulent scales within the model would require to solve the full Navier-Stokes equations, and is not computationally feasible. Therefore the high Reynolds number ABL flows of the present study are based on the solution of the incompressible RANS equations. They are closed using a two-equation k-ϵ turbulence model that models turbulence as isotropic. The horizontal mesh resolution is in the range of several meters (typically 10-20 m), and the individual roughness elements at the surface cannot be resolved. The effect of the surface roughness is therefore averaged and modeled using wall-functions for turbulent high Reynolds number flow over rough walls (Sørensen, 1995).

To capture temperature effects, the energy equation in terms of the potential temperature, θ, is solved parallel to the RANS equations. The potential temperature is modeled by a scalar transport equation, that couples with the RANS equations via additional terms (see chapter 2). Using the potential temperature formulation removes the typical rate of change of temperature with height (known as the dry adiabatic lapse rate, Γ_d) and is a useful parameter in atmospheric thermodynamics. Stable ($\partial\theta/\partial z > 0$) and unstable ($\partial\theta/\partial z < 0$) conditions are now easily recognized. To model different atmospheric stability conditions the surface temperature, θ_0, is prescribed at the lower boundary (or alternatively the surface heat flux, H_0), and the heat transfer between soil and air is not modeled. Also radiation that is emitted from the earth's surface, the atmosphere and from clouds is not modeled. Furthermore, the effects of humidity, condensation, clouds and precipitation are omitted in the model.

The central goal of the present study is to develop and validate a RANS ABL model framework that can be applied using the EllipSys3D solver to model neutral and non-neutral flows over complex terrain more appropriately. Improvements over existing neutral ASL models are, that the influences of the Coriolis force and atmospheric stability are now included in the model, and that transient effects governing the diurnal ABL evolution are captured. The aim is to present a tuning free ABL model that can be generally applied for neutral and non-neutral flows over complex terrain.

1.4.1 Background

The current work is carried out at the Wind Energy department of the Technical university of Denmark (DTU) within the Aeroelastic Design (AED) section. Core research activities are on the development of aero-servo-elastic simulation methods, computational fluid dynamics (CFD) codes and software design tools for analysis of airfoils, blades, and wind turbines. The present work is focusing on predicting atmospheric boundary-layer flows and was carried out in close collaboration with DTU Wind Energy's Meteorology section (MET), where research activities focus on e.g. the siting of wind turbines and potential power production. The PhD project is part of the WAUDIT project. WAUDIT is an Initial Training Network of the European Commission and focuses on wind resource assessment. The current PhD project is part of work package 2: microscale numerical modeling.

The starting point for the present work is the existing in-house (DTU Wind Energy) CFD solver EllipSys3D (Michelsen, 1992, 1994; Sørensen, 1995). The solver was initially developed for simulating the near-ground surface-layer flow inside a neutrally stratified domain and has under these conditions been validated against field experiments (Bechmann et al., 2011; Sørensen et al., 2007). The solver is based on the solution of the RANS equations in finite-volume discretization. To accurately model complex terrain flows, the solver uses curvilinear coordinates and a k-ϵ turbulence parameterization. The EllipSys3D code is robust and was previously successfully applied to assess the wind power potential for a range of different sites, where the mean wind speeds and turbulence levels are calculated across the area of interest.

1.4.2 Overview

The thesis is divided into two main parts. The first part describes the modeling approach and implementation aspects of the ABL model into the EllipSys3D flow solver (chapter 2 - 3) and the second part presents results of the developed ABL model applied to several test cases (chapter 4 - 5).

In chapter 2 the governing equations for neutral ASL flow are presented. Then the modifications necessary to model the Coriolis effect and atmospheric stability are shown. The modified k-ϵ turbulence model is shown, and necessary model constants are explained. In chapter 3, implementation aspects of the ABL model into the EllipSys3D solver are summarized. The solution method together with initial and boundary conditions are explained. The setup of the used computational grids is shown, and the methodology to simulate neutral

and non-neutral flows over flat and complex terrain is explained.

Chapters 4 to 5 present several test cases that are used to validate the ABL model. First, chapter 4 focuses on neutral and non-neutral ABL flow over rough flat ground: simulation results are compared against experimental data from the Leipzig wind profile (Lettau, 1950) and the Cabauw site (van Ulden and Holtslag, 1980). After showing that the ABL model is able to reproduce the effect of ground roughness and Coriolis force over flat terrain, non-neutral ABL flows are considered. Experimental data from the GABLS test case and simulation data from a model intercomparison study, both presented by Svensson et al. (2011), are used to validate the ABL model for non-neutral conditions. In chapter 4.5.1 Monin-Obukhov similarity theory is briefly described and used to compare simulation results for non-neutral ABL flow against experimental data from several large scale field campaigns (Businger et al., 1971; Li et al., 2008; Klipp and Mahrt, 2004).

After demonstrating the modifications necessary to model non-neutral ABL flows over flat terrain, the ABL model is used to analyse the combined effects of atmospheric stability and complex terrain in chapter 5. In section 5.1 a wind-tunnel experiment analysing neutral and stably stratified ABL flow over a steep hill (Ross et al., 2004) is used to assess the applicability of the ABL model for non-neutral flows over well defined terrain. Simulation results over the hill are presented and compared against measurements and previous simulations (Ross et al., 2004; Wan and Porté-Agel, 2011). Finally, in section 5.2 non-neutral flow over complex terrain at full scale is considered. Measurements from the Benakanahalli field experiment in India are used to assess the models performance over complex terrain. The field experiment was specifically designed to capture the combined effects of atmospheric stability and the Coriolis force (Berg et al., 2012).

Concluding remarks are given in chapter 6, and possible future work is discussed in chapter 7

CHAPTER 2

Modeling ABL flows

In this section the governing equations that describe the physics and dynamics of turbulent ABL flow are presented. The aim is to provide approximate solutions for the wind speed, direction and temperature, supplemented with a parametrization for turbulence. Atmospheric processes like radiation, humidity (clouds and precipitation) and heat transfer between soil and air are omitted in the modeling approach. The focus is on microscale phenomena in the ABL and atmospheric processes on greater scales are not included (see chapter 7 for a list).

First, the basic set of governing equations for neutral incompressible ASL flow are presented, together with the standard high Reynolds number k-ϵ turbulence closure. Second, adaptations of the governing equations are presented in order to describe the flow in the whole ABL, capturing stability and Coriolis effects.

The derivation of the discretized governing equations is not shown, and details can be found in Sørensen (1995).

2.1 Governing equations

Turbulence within the ABL covers a wide range of scales from less than a centimeter up to several kilometers (Jacobson, 2005). To fully describe these motions, the full Navier-Stokes equations need to be solved. Since this is computationally not feasible, high Reynolds number flows can instead be based on the solution of the RANS equations. Together with a two-equation closure method the flow within the whole ABL can be computed at a much lower computational cost than e.g. using LES (Bechmann, 2006). The high Reynolds number atmospheric flows considered in this study are based on the solution of the RANS equations, and the continuity and momentum equations read:

$$
\frac{\partial}{\partial x_i}(\rho U_i) = 0 \ . \tag{2.1}
$$

$$
\frac{\partial \rho U_i}{\partial t} + \frac{\partial \rho U_i U_j}{\partial x_j} - \frac{\partial}{\partial x_j}\left[(\mu + \mu_t)\left(\frac{\partial U_i}{\partial x_j} + \frac{\partial U_j}{\partial x_i}\right)\right] + \frac{\partial \hat{P}}{\partial x_i} = S_v \ , \tag{2.2}
$$

where x_i ($x_1 = x$, $x_2 = y$, $x_3 = z$) are the longitudinal, lateral and vertical directions. U_i is the mean velocity component along x_i, μ_t is the turbulent eddy viscosity and $\hat{P}$ is the pressure. The hydrostatic pressure, $\rho_0 g_i$, is absorbed in this pressure formulation and more details are given in section 2.3.1. In order to obtain a closed expression for the Reynolds stresses, they are modeled using the eddy viscosity hypothesis by Boussinesq (Schlichting, 1968):

$$
\rho \overline{u_i' u_j'} = -\mu_t \left(\frac{\partial U_i}{\partial x_j} + \frac{\partial U_j}{\partial x_i}\right) + \frac{2}{3}\rho k \partial_{ij} \ , \tag{2.3}
$$

where the latter term, $2/3\rho k \partial_{ij}$, is absorbed into the pressure term (Sørensen, 1995).

Since the unsteady term is retained in equation 2.2, it is possible to simulate transient phenomena with RANS. This is based on the assumption that time averaging of the RANS equations is performed on a time scale similar to the turbulent fluctuations, while the low frequency variations of the mean flow (e.g. diurnal simulations of stratified flows in the ABL, as considered in this study) can be properly resolved by the unsteady RANS equations. Transient RANS provides the possibility to simulate the unsteady phenomena of a diurnal cycle in the ABL, and is basically the only option besides the more computationally expensive LES approach.

2.2 Basic RANS closure for neutral ASL flows

The RANS equations can be used to describe the air flow in the neutral ASL. Here, in the lowest part of the ABL, the logarithmic wind profile (equation 3.1) is often a justified approximation when the flow is assumed to be neutrally stratified. Therefore stability and Coriolis effects are neglected. To close the given set of equations the popular k-ϵ turbulence model is used (Launder and Spalding, 1974). The eddy viscosity is obtained by solving the two partial differential transport equations for the turbulent kinetic energy k and the dissipation rate ϵ:

$$\frac{\partial k}{\partial t} + U_i \frac{\partial k}{\partial x_i} - \frac{\partial}{\partial x_i}\left(\frac{\mu_t}{\sigma_k}\frac{\partial k}{\partial x_i}\right) \;=\; P_k - \epsilon \;, \tag{2.4}$$

$$\frac{\partial \epsilon}{\partial t} + U_i \frac{\partial \epsilon}{\partial x_i} - \frac{\partial}{\partial x_i}\left(\frac{\mu_t}{\sigma_\epsilon}\frac{\partial \epsilon}{\partial x_i}\right) \;=\; \frac{\epsilon}{k}\left(C_{\epsilon 1} P_k - C_{\epsilon 2}\epsilon\right) \;, \tag{2.5}$$

where σ_k and σ_ϵ are the Schmidt numbers for k and ϵ respectively. $C_{\epsilon 1}$ and $C_{\epsilon 2}$ are model coefficients (see section 2.5). P_k is the rate of shear production of k:

$$P_k = -\rho \overline{u_i' u_j'} \frac{\partial u_j}{\partial x_i} = \mu_t \left(\frac{\partial U_i}{\partial x_j} + \frac{\partial U_j}{\partial x_i}\right) \frac{\partial u_j}{\partial x_i} \;. \tag{2.6}$$

The resulting mixing length, l_t, and the eddy viscosity, μ_t, are expressed in terms of k and ϵ as:

$$l_t = C_\mu^{3/4}\frac{k^{3/2}}{\epsilon} \;, \tag{2.7}$$

$$\mu_t = \rho C_\mu \frac{k^2}{\epsilon} = \rho C_\mu^{1/4} k^{1/2} l_t \;. \tag{2.8}$$

2.3 Adaptation of governing equations for ABL flows

The large-scale dynamics within the ABL are subjected to thermal stratification and the Coriolis effect (caused by the rotation of the earth and the inertia of

mass), and these should be included when modeling the flow within the whole ABL at full scale. These effects are introduced into the RANS equation system through additional source/sink terms that are added explicitly to the right hand side of the momentum equations 2.2 as an external force:

$$S_v = g_i(\rho - \rho_0) + \varepsilon_i f_c \rho U_i + S_{vol} \ , \tag{2.9}$$

where g_i is the gravitational acceleration, $g_i^T = (0, 0, -g)$, ρ is the varying density and ρ_0 is a reference density. $\varepsilon_i^T = (-1, 1, 0)$ and $f_c = 2\Omega_E \sin\lambda$ is the Coriolis parameter (with the earth's rotation rate Ω_E and the latitude λ). Only the component of the Coriolis force that acts perpendicular to the direction of the wind is considered, when viewed from a rotating reference frame. This force causes the air to deflect from its path and causes the wind to veer with height. The Coriolis force in vertical direction is neglected, since in atmospheric flows the vertical component of the Coriolis acceleration is small compared to the gravitational acceleration.

2.3.1 Boussinesq approximation for buoyancy

The term $g_i(\rho - \rho_0)$ in equation 2.9 accounts for density variations due to temperature changes in the ABL. The Boussinesq approximation for buoyancy states that density variations are small enough to be neglected in all model equations, except where they appear together with the gravitational acceleration. The formulation of the buoyancy term is based on a series of approximations which are described in some detail in the present section. The approach is based on a combination of the hydrostatic relation, the ideal gas law and the definition of potential temperature.

The flow in the present study is treated as incompressible. Therefore pressure changes due to density changes are by definition negligible, and a separate energy equation is not necessary (which would be needed for compressible flow). The assumption of incompressibility does not necessarily require constant density: if density changes are relatively small and appear at low speeds (compared to the speed of sound), the flow can still be treated as incompressible.

In the ABL, pressure, density and temperature are linked over a wide range of conditions via the ideal gas law. Assuming incompressible flow, density is not a function of pressure, and the ideal gas law can be simplified. The molar form

of the ideal gas law is approximated by:

$$\rho = \frac{MP}{RT} \approx \frac{MP_0}{RT} \ , \tag{2.10}$$

and temperature, T, and density, ρ, vary linearly, as required by the Boussinesq approximation for buoyancy. $M = 29$ g/mol is the estimated average molar mass of dry air and $R = 8.313$ J/mol K is the universal gas constant. The pressure, P, is replaced by the standard atmospheric pressure, P_0, approximated by $P_0 \approx 1 \times 10^5$ Pa.

Relative changes in temperature are now inversely proportional to changes in density, which together with the gravitational acceleration results in vertical buoyancy forces. The Boussinesq approximation for buoyancy only accounts for density changes via a buoyancy term in the vertical component of the momentum equation, and neglects them in all other equations. For the assumption of horizontally homogeneous flow, the vertical component of the momentum equations including the buoyancy term reduces to:

$$\rho \frac{\partial w}{\partial t} = -\frac{\partial P}{\partial z} - \rho g_z = -\frac{\partial P}{\partial z} - \rho_0 g_z - (\rho - \rho_o) g_z \ , \tag{2.11}$$

where ρ_0 is a reference density. The term, $\rho_0 g_z$, corresponds to the hydrostatic pressure and is absorbed into the pressure formulation, assuming the ABL is in hydrostatic balance:

$$\rho \frac{\partial w}{\partial t} = -\frac{\partial \hat{P}}{\partial z} - (\rho - \rho_0) g_z, \tag{2.12}$$

where $\hat{P} = P + \rho_0 g_z z$. The density variations in the buoyancy term, $(\rho - \rho_0) g_z$, are written in terms of temperature variations by inserting equation 2.10 into 2.12:

$$\rho \frac{\partial w}{\partial t} = -\frac{\partial \hat{P}}{\partial z} - \frac{MP_0}{R} \left(\frac{1}{\theta} - \frac{1}{\theta_0} \right) g_z. \tag{2.13}$$

Note that the absolute temperature, T, is replaced by the potential temperature, θ. The potential temperature is defined as the temperature that an air parcel

at pressure P would acquire if adiabatically brought to the reference pressure P_0:

$$\theta = T \left(\frac{P_0}{P} \right)^{\frac{R}{c_p}} , \qquad (2.14)$$

where $c_p \approx 1$ J/gK is the specific heat capacity of dry air at a constant pressure. The potential temperature is a useful parameter in atmospheric thermodynamics, since the negative change of temperature with height (the dry adiabatic lapse rate $\Gamma_d = -\partial T/\partial z = g/c_p \approx 9.8$ °K/km) is removed. Stable ($\partial\theta/\partial z > 0$) and unstable ($\partial\theta/\partial z < 0$) conditions are now easily recognized.

To model temperature changes, an equation for the energy in terms of the potential temperature is solved in addition to the RANS equations. The scalar transport equation reads:

$$\frac{\partial}{\partial t}(\rho\theta) + \frac{\partial}{\partial x_i}(\rho U_i \theta) - \frac{\partial}{\partial x_i}\left[\left(\mu + \frac{\mu_t}{\sigma_\theta}\right)\frac{\partial\theta}{\partial x_i}\right] = S_\theta . \qquad (2.15)$$

In the ABL, density variations are usually assumed to be small $(\rho - \rho_0)/\rho_0 \ll 1$, and the Boussinesq approximation for buoyancy is justified. Note that it is not necessary to limit the density variations to the vertical momentum equation. In the present study the variable density, ρ, replaces the reference density, ρ_0, in all momentum and transport equations. Note that the term 'Boussinesq approximation' is also used for different approximations than the one presented here (eddy-viscosity concept in turbulence models, shallow water equations).

2.4   Adaptation of RANS turbulence closure for ABL flows

The k-ϵ turbulence model in its standard form, given in section 2.2, is not capable of representing non-neutral conditions. To take stability effects into account, a modified version is employed to close the given set of equations. Recently Sogachev et al. (2012) developed a consistent closure method for the two-equation turbulence model by considering the behavior of the ϵ equation in homogeneous turbulent flow when using a source/sink term associated with stability. The potential temperature equation now couples with the turbulence model via an additional source/sink term B that is added to the two turbulent

transport equations (Pope, 2000; Pielke, 2002). The two modified transport equations for the turbulent kinetic energy k and the dissipation ϵ read:

$$\frac{\partial k}{\partial t} + U_i \frac{\partial k}{\partial x_i} - \frac{\partial}{\partial x_i}\left(\frac{\mu_t}{\sigma_k}\frac{\partial k}{\partial x_i}\right) = P_k - \epsilon + B \ , \tag{2.16}$$

$$\frac{\partial \epsilon}{\partial t} + U_i \frac{\partial \epsilon}{\partial x_i} - \frac{\partial}{\partial x_i}\left(\frac{\mu_t}{\sigma_\epsilon}\frac{\partial \epsilon}{\partial x_i}\right) = \frac{\epsilon}{k}\left(C_{\epsilon 1}^* P_k - C_{\epsilon 2}\epsilon + C_{\epsilon 3}B\right) + D \ . \tag{2.17}$$

$C_{\epsilon 1}^*$ is a modified $C_{\epsilon 1}$ coefficient (see section 2.4.1) and D is an additional diffusion term (see section 2.4.2). An additional buoyancy source/sink term B is added to the turbulent kinetic energy equation and also appears in the dissipation equation together with the coefficient $C_{\epsilon 3}$ (see section 2.5.2) and depends on the eddy viscosity, μ_t, the gravitational acceleration, g_i, and the density gradient:

$$B = -\mu_t g_i \frac{\partial \rho}{\partial x_i} \ . \tag{2.18}$$

In unstable conditions, B is positive and supports the generation of turbulent kinetic energy, while B turns negative in stable conditions and suppresses turbulence. Details about the specification of the coefficient $C_{\epsilon 3}$ are given in section 2.5.2.

2.4.1 Length-scale limitation

The standard k-ϵ model, when applied to ABL flows, is known to be too diffusive, leading to a strongly overestimated turbulent length scale, l_t, that grows continuously with height and results in a very large ABL height (Spalart and Rumsey, 2007; Apsley and Castro, 1997; Detering and Etling, 1985). In real ABL flows, the maximum size of turbulent eddies is limited e.g. by the finite ABL height or by stratification (Zilitinkevich and Esau, 2002). In the present study, a length-scale-limitation is used, as initially proposed by Apsley and Castro (1997), which effectively reduces the global maximum mixing length in the model and the resulting ABL height. The modified $C_{\epsilon 1}^*$ coefficient in the length scale determining equation 2.17 is described by:

$$C_{\epsilon 1}^* = C_{\epsilon 1} + (C_{\epsilon 2} - C_{\epsilon 1})\frac{\ell_t}{\ell_e} \ . \tag{2.19}$$

Apart from the maximum global mixing length, l_e, no additional coefficients are introduced. When the local mixing length, l_t, reaches the specified global maximum mixing length, l_e, $C_{\epsilon 1}^*$ equals $C_{\epsilon 2}$ and the production and destruction terms in the dissipation equation are in balance, which limits the local length scale, l_t, to l_e. On the other end, when $l_t << l_e$, $C_{\epsilon 1}^*$ equals $C_{\epsilon 1}$ and the modification still satisfies the logarithmic wind profile in the surface-layer close to the ground.

For neutrally stratified ABL flows over a flat rough surface, l_e is estimated by an expression from Blackadar (1962). To provide a suitable solution for stratified flows, an expression from Mellor and Yamada (1974) is used that depends on the vertical distribution of turbulent kinetic energy k in the ABL, and reflects variations in ABL depth induced by thermal stratification:

$$l_e = \begin{cases} l_0 & = 0.00027\frac{G}{f_c} & \text{, constant in neutral ABL} \\ l_{MY} & = \alpha\frac{\int_0^\infty z\sqrt{k}dz}{\int_0^\infty \sqrt{k}dz} & \text{, reflecting variable ABL depth} \end{cases} , \qquad (2.20)$$

where G is the geostrophic wind. The coefficient α is chosen so that both length scales are identical for a neutrally stratified ABL flow ($l_{MY} = l_0$). For several test cases an empirical value of $\alpha = 0.075$ results in both length scales to agree reasonably well ($l_{MY} \approx l_0$) (Sogachev et al., 2012). To calculate l_{MY} with the above expression, the turbulent kinetic energy, k, needs to be integrated over the domain height. For horizontally homogeneous flow, it is sufficient to perform this integration every time step at one location. For complex terrain domains with a curvilinear grid, this integration would have to be performed at every location individually. This is computationally not feasible, and instead a precursor simulation over flat terrain can be used to determine the time varying values of l_{MY}, that are then used within a complex terrain domain (for details see section 3.6.2).

2.4.2 Diffusion term

An additional diffusion type term D is introduced into the dissipation equation 2.17 of the k-ϵ model as proposed by Sogachev et al. (2012). Numerical experiments have shown some differences in the behavior of the standard k-ϵ model of Launder and Spalding (1974) and the k-ω model of Wilcox (1998). Sogachev and Panferov (2006) reported that for example in forest canopies, the k-ω model is performing slightly better than the k-ϵ model. The ABL model in the present study uses the k-ϵ model, and to obtain consistent results between

the two closures, the k-ϵ model can be transformed to behave similarly to the k-ω model, by including an additional diffusion term:

$$D = C_\mu \left[\left(\frac{1}{\sigma_k} - \frac{1}{\sigma_\epsilon} \right) k \frac{\partial^2 k}{\partial x_i^2} - \left(\frac{1}{\sigma_k} + \frac{1}{\sigma_\epsilon} \right) \frac{k}{\epsilon} \frac{\partial \epsilon}{\partial x_i} \frac{\partial k}{\partial x_i} + \frac{2}{\sigma_k} \frac{\partial k}{\partial x_i} \frac{\partial k}{\partial x_i} \right] \ . \quad (2.21)$$

2.5 Model coefficients

2.5.1 Specification of general constants

The model constants $C_{\epsilon 1}$ and $C_{\epsilon 2}$ in equations 2.5 and 2.17 are chosen to be consistent with experimental observations for decaying, homogeneous, isotropic turbulence. To ensure that the model solution agrees with the constant-stress logarithmic wind profile near the ground the relation below has to be satisfied, which follows from considering constant-flux flow with $\partial k / \partial z = 0$ (Hanjalic and Launder, 1972; Richards and Hoxey, 1993):

$$\sigma_\epsilon = \frac{\kappa^2}{C_\mu^{1/2}(C_{\epsilon 2} - C_{\epsilon 1})} \ , \quad (2.22)$$

where κ is the van Karman constant, and the constant C_μ is found by considering equilibrium turbulence near a wall:

$$C_\mu = \left(\frac{u_{*0}^2}{k} \right)^2 = \left(\frac{\tau_0}{k} \right)^2 \ , \quad (2.23)$$

where τ_0 is the wall stress. For neutral flows, the constant C_μ is typically adjusted to set a desired turbulence level. $C_\mu = 0.09$ is a typical value for industrial flows (Launder and Spalding, 1974) while in atmospheric research a value of $C_\mu = 0.03$ is often used (Katul et al., 2004). u_{*0} is the friction velocity at the wall. The friction velocity, u_*, can be written using the kinematic momentum fluxes as:

$$u_* = \left(\overline{u_i' u_k'}^2 + \overline{u_j' u_k'}^2 \right)^{1/4} \ . \quad (2.24)$$

Table 2.1: Typical values for the coefficients in the k-ϵ turbulence model for industrial flows ($C_\mu = 0.09$) and for atmospheric flows ($C_\mu = 0.03$).

Flow	C_μ	κ	$C_{\epsilon 1}$	$C_{\epsilon 2}$	$C_{\epsilon 3}$	σ_k	σ_ϵ	σ_θ
Standard (Launder and Spalding, 1974)	0.09	0.40	1.42	1.92	0	1.00	1.30	0.71
ASL (Katul et al., 2004)	0.03	0.40	1.21	1.92	0	1.00	1.30	0.71
ABL (Sogachev et al., 2012)	0.03	0.40	1.52	1.83	eq. 2.25	2.95	2.95	eq. 2.27

2.5.2 Specification of stability related coefficients

The additional coefficient $C_{\epsilon 3}$ in the dissipation equation 2.17 has to be specified, but an optimal value is unknown (Sogachev, 2009). Using the recently developed consistent closure method for two-equation turbulence models from Sogachev et al. (2012), $C_{\epsilon 3}$ is modeled using a stability-related coefficient α_B (see table 2.1):

$$C_{\epsilon 3} = (C_{\epsilon 1} - C_{\epsilon 2})\alpha_B + 1 \ . \tag{2.25}$$

α_B is specified based on the standard coefficients $C_{\epsilon 1}$ and $C_{\epsilon 2}$ of the production and destruction terms in the ϵ equation respectively:

$$\alpha_B = \begin{cases} 1 - \frac{\ell_t}{\ell_{MY}} & \text{for } Ri_g > 0 \\ 1 - [1 + \frac{C_{\epsilon 2} - 1}{C_{\epsilon 2} - C_{\epsilon 1}}]\frac{\ell_t}{\ell_{MY}} & \text{for } Ri_g < 0 \end{cases} \ , \text{ with } Ri_g = B/P_k \ . \tag{2.26}$$

α_B now depends on the local gradient Richardson number Ri_g and on the local ratio of l_t/l_{MY}, and hence is a function of stability.

In the model, the turbulent Prandtl number, σ_θ, in equation 2.15 is approximated as a function of a slightly modified gradient Richardson number, Ri_G:

$$\sigma_\theta = \begin{cases} 0.74 & \text{for } Ri_g > 0 \\ 0.74(1 - 15Ri_G)^{-1/4} & \text{for } Ri_g < 0 \end{cases} \ , \text{ with } Ri_G = B/(P_k + |\tfrac{\alpha_B}{\sigma_\theta}B|) \tag{2.27}$$

The additional term in the denominator of the gradient Richardson number, Ri_G, is used to stabilize equation 2.27: Ri_G and the resulting turbulent Prandtl number, σ_θ, are now limited during convective cases where P_k approaches zero.

Sogachev et al. (2012) have shown numerically that the developed model framework is suitable for three flow regimes: grid turbulence, wall-bounded flow and homogeneous shear flow. In contrast to an earlier proposed description of $C_{\epsilon 3}$ (Sogachev, 2009), the form given in equation 2.26 is universal and needs not to be specified for each case. Compared to the ASL model no additional coefficients are introduced into the ABL model that need to be calibrated. The formulation does not allow for any tuning of the model and only depends on the closure coefficients given in table 2.1.

2.6 Temperature relaxation

In real ABL flow, the surface heating changes throughout the day due to incoming solar radiation at day, and emitted longwave radiation at night. In the model, this process is simplified by prescribing a varying surface temperature at the wall boundary. Radiation at the surface is therefore indirectly taken into account. However, radiation (thermal-infrared) is an important energy transfer process within the whole ABL (Jacobson, 2005), and both the ground and the air above cool down at night by radiating energy. To take temperature variations on top of the ABL into account, a temperature relaxation is used, as e.g. suggested by Sogachev (2009). The temperature is relaxed towards an initial stable vertical temperature profile (typically using a vertical gradient of 3.5K/km), using a relaxation time of 24 h. During this period all characteristics should return to their initial state in the absence of any forcing. The relaxation is performed at every time step after solving the energy equation 2.15:

$$\theta^*(z,t) = \theta(z,t) - max\left(0, \frac{\theta(z,t) - \theta(z,0)}{24 \ h}\Delta t\right) \ , \qquad (2.28)$$

where Δt is the time step (typically 10 s) and the max-limiter ensures that the temperature is only relaxed towards stable conditions. Due to the long relaxation time, the relaxation terms are very small and negligible close to the ground, where mechanical and buoyant turbulence are governing the temperature evolution. The relaxation only affects the top of the ABL. During daytime the ABL reaches the capping inversion. The inversion acts as a lid, suppressing vertical motion, but is not a solid boundary: each day the computed ABL overshoots a small distance into the capping inversion (called entrainment in real ABL flow). This is a one-way process that results in an ABL that grows after each diurnal cycle. The temperature relaxation limits this process, and the computed ABL reaches a constant maximum height. It also ensures that

the temperature at the ABL top reaches a constant level, while without the relaxation the temperature between two days is slightly but constantly increasing. Using a temperature relaxation is a simplification of the real physical processes involved, but has shown to improve results. The main effect is the stabilization of the ABL growth, which is needed to obtain a cyclical solution when simulations of diurnal cycles are continued for several days.

Simulating ABL flows

To simulate neutral ASL flow over flat terrain, initial conditions for the wind speed are typically specified by the logarithmic wind profile. This is a justified approximation and typically inlet/outlet boundary conditions are used where the incoming flow is specified by the logarithmic wind profile according to a specific surface roughness, z_0. The flow problem is then solved steady-state.

When simulating the whole ABL including the Coriolis effect, the resulting wind profile is not known prior to solving the flow problem. Therefore a separate simulation is used to determine appropriate inlet conditions for complex terrain domains. Such a precursor simulation is typically performed on a small flat domain with periodic lateral boundary conditions, since the resulting flow is horizontally homogeneous. The computational domain height is usually larger than what is typically used in flow simulations, to ensure that the whole ABL is fully resolved by the model. Introducing the effect of non-neutral stratification on the flow further complicates the problem. When considering diurnal variations in the ABL, the flow is now time-dependent and the unsteady solution is not known in advance. Therefore transient precursor simulations are used to compute the time-varying vertical structure of the whole ABL. The computed flow profiles can then be used to describe the unsteady incoming flow for terrain simulations.

The following section describes how the modified ABL model equations pre-

sented in chapter 2 are implemented into the EllipSys3D solver (Michelsen, 1992, 1994; Sørensen, 1995), that is used for all computations. Sections 3.2 and 3.3 explain the initial and boundary conditions used. Section 3.4 describes how the resulting flow problems are solved numerically. Section 3.5 presents the computational grids that are typically used to simulate neutral and non-neutral ABL flow over flat and complex terrain, and finally section 3.6 gives details about the developed simulation methodology for ABL flows.

3.1 Implementation aspects of ABL equations

3.1.1 Force allocation model

The buoyancy volume force, $g_i(\rho - \rho_0)$, in the momentum equation 2.2 is added explicitly as an external volume force. When implemented into the solver, this will create numerical problems. The EllipSys3D solver uses a non-staggered pressure/velocity arrangement (collocated variable method) and a Rhie-Chow pressure correction algorithm (Rhie and Chow, 1982) to avoid the pressure-velocity decoupling. The implementation of buoyancy forces is identified to cause oscillations in the solution, especially close to boundaries and under strongly stratified conditions. This is due to an inconsistency with the original body forces that are applied in the cells. To avoid this, an algorithm for allocating discrete forces is used following Réthoré and Sørensen (2012). This approach solves the problem by applying an equivalent pressure jump at the cell faces and by spreading the force on the direct neighbouring cells.

3.1.2 Ambient turbulence values

In order to improve convergence for small mixing lengths, ambient floor values for the turbulence variables are imposed. Especially during strongly stable conditions the mixing length, l_t, and the eddy viscosity, μ_t, approach values close to zero or even negative values. This typically occurs within the stable temperature layer (inversion) in the upper part of the ABL. To avoid numerical convergence issues, k and ϵ are not allowed to drop below a predefined limit. The ambient values, k_{amb} and ϵ_{amb}, are defined a priori and set a minimum turbulent mixing length via equation 2.7. They are set using a minimum limiter on the turbulence variables: $\epsilon = max(\epsilon, \epsilon_{amb})$ and $k = max(k, k_{amb})$. Values below the ambient level are simply overwritten. Instead, the ambient values can also be added explicitly into the turbulent transport equations for k and

ϵ, as suggested by Spalart and Rumsey (2007). For the present ABL model both approaches give the same result, and for reason of simplicity the former approach is used. Using this approach is numerically less elegant, but ensures that the modification is only active on top where the turbulence variables approach their ambient values. The approach of Spalart and Rumsey (2007) needs an additional blending function since adding the ambient values throughout the whole domain would distort the wall boundary condition.

Note that the ambient values have to be chosen carefully, such that the flow in the lower part of the domain is not influenced by the constrained turbulence variables in the upper parts. For the present study the ambient turbulence values are chosen to be $k_{amb} = 1 \cdot 10^{-4}$ m^2/s^2 and $\epsilon_{amb} = 7.208 \cdot 10^{-8}$ m^2/s^3. Together with the model constants in table 2.1 and equation 2.8 and 2.7 this leads to a moderate eddy viscosity on top and a minimum turbulent mixing length of 1 m. The modification is physically justified since it is only active in the upper part of the ABL where the turbulence variables approach their predefined ambient levels, and does not influence the flow in lower heights or distort the wall boundary condition.

3.2 Boundary conditions

Before numerically solving the equations presented in chapter 2 the boundary conditions need to be specified. For the flow problems in the present study general Dirichlet and Neumann conditions are mainly used, and either the cell value or the gradient is described at the cell faces respectively. This is used for the lateral inlet/outlet boundaries, and for the symmetric top boundary. The bottom of the domain is treated differently, and for the ABL flow problems considered in this study, wall boundaries are used. For the lateral boundaries periodic boundary conditions can be used, and details are given in the following sections. Note that the presented boundary conditions do not include the treatment of the pressure, and details can be found in Sørensen (1995).

3.2.1 Wall boundary

A rough wall boundary condition is used at the bottom of the domain (Sørensen et al., 2007). For the high Reynolds number flows considered in this study, the laminar viscous sub-layer is therefore neglected. Instead of resolving the laminar sub-layer, wall-functions for the velocity and the turbulence variables are used.

The derivation of the wall-functions is based on equilibrium assumptions (see Sørensen (1995) for details). The resulting logarithmic profiles for the wind speed, U, and the turbulent kinetic energy, k, are:

$$U = \frac{u_{*0}}{\kappa} \ln\left(\frac{z + z_0}{z_0}\right) \ , \tag{3.1}$$

$$k = \frac{u_{*0}^2}{C_\mu^{1/2}} \ . \tag{3.2}$$

The first cell is placed on top of the roughness elements, as seen in equation 3.1: $U=0$ for $z=0$. Displacing the first model level by z_0 has the advantage that in case of large roughness changes (e.g. sea to land) there are no minimum height restrictions for the first cell.

The wall-function for the velocity is implemented through the wall shear stress τ_0:

$$\tau_0 = \frac{\rho \kappa C_\mu^{1/4} k^{1/2} U(z_p)}{\ln\left(\frac{\Delta z}{z_0} + 1\right)} \ , \tag{3.3}$$

where Δz is the distance from the bottom face of the cell to the cell centre, z_p.

For the turbulent kinetic energy, k (equation 2.4), a von Neumann boundary condition is used. The production term in the first cell is replaced by an equilibrium value, that results from considering a balance between the production, P_k (equation 2.6), and dissipation, ϵ:

$$P_k = \frac{\tau_0}{2\Delta z} \frac{\ln\left(2\Delta z z_0^{-1} + 1\right)}{\ln\left(\Delta z z_0^{-1} + 1\right)} U(z_p) \ . \tag{3.4}$$

The dissipation term in the turbulent kinetic energy equation is set to the average equilibrium value in the wall cell:

$$\epsilon = \frac{C_\mu^{1/2} k U(z_p)}{2\Delta z} \frac{\ln\left(2\Delta z z_0^{-1} + 1\right)}{\ln\left(\Delta z z_0^{-1} + 1\right)} \ . \tag{3.5}$$

The dissipation of turbulent kinetic energy in the first cell is specified according to the balance between the production and dissipation obtained for the fully developed flow:

$$\epsilon = \frac{C_\mu^{3/4} k^{3/2}}{\kappa \left(\Delta z + z_0\right)} \ . \tag{3.6}$$

For the potential temperature a Dirichlet boundary condition is used at the wall boundary. In the present study the boundary temperature, $\theta_0(t)$, is given as a

model input, and no additional equations are required. If instead the boundary heat flux, H_0, is given, a Neumann boundary condition is used and more details are given by Patankar (1980).

3.2.2 Inlet boundary

At inlet boundaries a Dirichlet conditions is used and all flow variables (wind speed, temperature, turbulence variables) need to be known in advance and specified at the cell faces. For neutral ASL flow the logarithmic wind profile is typically used to describe the incoming flow. When ABL flows including stability and/or the Coriolis effect are considered, the incoming flow is not known in advance and theoretical profiles are often not satisfying. For more details how inlet boundaries for these flow problems are specified in the present study see section 3.6.

3.2.3 Outlet boundary

At outlet boundaries the flow that leaves the domain is typically not known before solving the problem. Therefore outlet boundaries are not specified prior to the simulation, and are defined during the solution by extrapolating the relevant flow variables from inside the domain onto the boundary cell faces. This results in zero normal gradients which introduces an error for not fully developed flows. Therefore the outlet boundaries are placed far downstream of the area of interest in order to minimize the effect of the introduced error.

3.2.4 Symmetry boundary

At the top boundary a symmetry condition (no-gradient) is used. Fluxes across the top of the domain are zero for all flow variables. Therefore all normal gradients and the shear stress is zero on top.

3.2.5 Periodic boundary

For horizontally homogeneous flow over flat terrain periodic conditions are used on the lateral boundaries. The computational domain can therefore be very

small, since the horizontal extend of the domain is irrelevant. Periodic boundaries are placed opposite of each other, and the flow variables on one side of the domain are handled directly by the multiblock framework and moved to the cell faces on the other side.

3.3 Initial conditions

For neutral ASL flows initial conditions for the wind speed are typically specified by the logarithmic wind profile according to a specific surface roughness, z_0 (equation 3.1). However, since periodic boundary conditions are used for the present flat terrain simulations, the final results do not depend on their initial conditions. The temperature field is initialized with an inversion layer. The vertical potential temperature field is described by: $\theta(z, 0) = \theta_0 + 3.5$ K/km, and extends over the whole domain. For the simulation of diurnal cycles, the initial wall temperature, θ_0, is usually chosen to be the average value of the diurnally varying surface temperature.

3.4 Solution methods in EllipSys3D

The EllipSys3D code is a multiblock finite volume discretization of the incompressible Navier-Stokes equations. All equations are transformed into general curvilinear coordinates. This allows the model to be applied to complex geometries, like ABL flow over terrain, where the use of Cartesian or rectangular coordinates is often not possible.

The code uses a collocated variable arrangement where all flow variables are defined in the center of the control volume. To avoid the appearance of pressure oscillations, a Rhie/Chow interpolation is used (Rhie and Chow, 1982). The pressure is solved using the SIMPLE algorithm of Patankar and Spalding (1972).

The EllipSys3D code is parallelized with MPI for execution on distributed memory machines, using a non-overlapping domain decomposition technique. To solve the convection-diffusion equations, the third-order accurate QUICK differencing scheme is used. Central differences are used for the remaining terms. The three momentum equations are solved decoupled using a red/black Gauss-Seidel point solver, and the solution of the Poisson system from the pressure correction equation is accelerated using a multi-grid method.

To ensure that the grid resolution is sufficient for the given flow problem, simulations are solved using multi-level grid sequencing. Coarser meshes are constructed from the original mesh by removing every second grid point in all three directions. This reduces the number of cells between grid levels by a factor of eight. This technique provides the possibility to solve the flow problem without the need of very accurate initial conditions. The solution is started on a coarse grid level and continued on a finer grid level once a given convergence criterion is fulfilled. For steady-state simulations a convergence criterion of $RES < 10^{-5}$ is used. For each flow variable the residual is defined by the difference between the left and right hand side of the respective dicretized equation. The absolute sum of the residuals at every cell is normalized by the initial residual: RES_k/RES_0. This value is used as an indicator of convergence, and iterations are terminated when a value of 10^{-5} is reached.

For the transient simulations considered in this study, a time step of 10 s is used. For the simulation of diurnal cycles, the variations of the computed flow field are on a time scale of several minutes or more, so that the chosen time step is small enough to capture the transient behavior. This time step is used for all cells in the domain and the numerical solution is advanced in time using a second order accurate backward time-stepping method using the previous two time steps.

3.5 Computational domain

Depending on the flow that is to be simulated, different computational domains are chosen. ABL flow over flat terrain with a uniform roughness is horizontally homogeneous. Therefore the horizontal extend of the grid is irrelevant, and a small domain with periodic lateral boundaries can be used, since all flow variables only depend on height. Such a grid is described below in section 3.5.1. To simulate ABL flow over complex terrain, the grid needs to cover all relevant terrain features with a sufficient resolution. Such a mesh is described in section 3.5.2, and table 3.1 summarizes some key parameters of the two different grids. If other meshes than the ones presented in this section are used, they are specified in the relevant section.

3.5.1 Flat terrain

For all flat terrain simulations the same type of computational domains is used: it is 6 km high and uses a grid of 192 stretched cells in vertical direction. The

Table 3.1: Computational domain properties

Test case	Flat terrain	Benakanahalli
Domain length x-dir [km]	1	30
Domain length y-dir [km]	1	30
Domain height z-dir [km]	6	4
Grid type	regular	block structured
Cell type	regular (rectilinear cells)	curvilinear (hexahedral cells)
Total cell count	1.1×10^5	7.1×10^6
Near-wall cell height [m]	z_0	0.1

bottom cell is equal to the size of the specific roughness length, z_o, at the wall, and the mesh is expanding hyperbolically towards the top, resulting in cell heights of about 70 m at the top boundary. In horizontal directions the domain is 1 x 1 km long with a grid of 24 evenly distributed cells. However, as the modeled flow over flat surfaces is horizontally homogeneous, the horizontal grid structure is irrelevant as the flow variables should become functions of the height z alone. Rough wall boundary conditions are used at the bottom of the domain (Sørensen et al., 2007), and a symmetry condition (no-gradient) is used on top. All vertical boundaries are periodic. Note that grid independent results could already be obtained using a grid of around 100 cells in the vertical direction. In figure 3.1 a side an top view of the grid are shown.
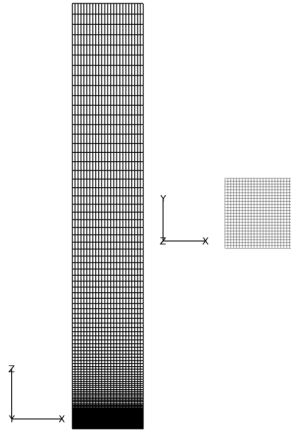
Figure 3.1: Grid used for flat terrain simulations. Left: side view; right: top view. Lateral boundaries are periodic, top boundary is symmetric and bottom boundary is a rough wall.

3.5.2   Complex terrain

Since the Ellipsys3D code uses terrain-following coordinates, it is possible for the lower boundary of the computational mesh to follow the topography. To generate the computational grid, a surface grid is first constructed using an in-house 2D surface grid generator. Instead of projecting the grid vertically onto the terrain, the surface grid is generated by growing the grid directly on the terrain surface model. This results in grids with good resolution in areas of steep terrain and avoids highly skewed cells. The volume grid is generated using the enhanced hyperbolic grid generator HypGrid3D (Sørensen, 1998). The result is a 3D structured hexahedral volume mesh with cells of low skewness, and there is no constraint on the cell aspect ratio.

For the present terrain simulations a polar computational domain is chosen, which enables the same mesh to be used for different wind directions. The computational domain has a radius of about 15 km and is about 4 km high. This height is larger than what is typically used for neutral flows, and ensures that the domain is high enough to cover the whole ABL. If the maximum terrain height difference within the modeled area is large, the domain can be even higher (as a rule of thumb the domain height is usually set to be at least seven times the maximum height difference). In vertical direction, a grid of 96 vertically stretched cells is used. The cell height at the wall is similar to the roughness length, z_0, and the cell height at the top boundary can be larger than 100 m, depending on the absolute domain height. In horizontal direction, the grid is expanding towards the lateral boundaries, while in the area of interest (usually a 4x4 km square in the middle of the domain) the horizontal resolution is around 20 m. The lateral walls have inlet/outlet boundary conditions, the top boundary is symmetric (no-gradient) and at the bottom a rough wall boundary condition is used (Sørensen et al., 2007).

In total, the computational grid has typically around seven million cells (grid level 1). To assure that the flow is sufficiently resolved, simulation results have been compared on coarser grid levels. The grid convergence study showed that grid level 2 (about 0.85 million cells) gave near identical results to grid level 1 for the terrain considered here. Note that this has to be determined individually for the specific type of terrain considered in each case. Especially in highly complex terrain, it is difficult to obtain agreement between grid levels, since the change of resolution between grid levels will always slightly alter the resolved terrain.

In figure 3.2 the surface grid of the Benakanahalli hill in India (see section 5.2) is shown. Towards the boundaries, the horizontal resolution is reduced. The terrain features are smoothed towards the boundaries, in order to have horizontally homogeneous inflow conditions. In figure 3.3 the multiblock volume grid

generated with HypGrid3D is shown.

3.6 Simulation Methodology

The typical method to simulate neutral ASL flow over flat terrain is briefly described in the beginning of this chapter (logarithmic inlet profiles, steady-state solution). The focus of the present work is on non-neutral ABL flow. Different stability conditions can be induced in the ABL model by either applying a vertically varying temperature at an inlet boundary (free stream stability), or by varying the surface temperature in time (surface stability). Alternatively, the wall heat flux can be prescribed. In this study, different stabilities are always induced via the wall temperature, which represents an unsteady boundary condition.

Non-neutral ABL flow (section 2.3) is always computed transient in order to capture the time-dependent behavior of the flow. This is possible since the unsteady term is retained in the RANS equations (for more see section 2.1). The described model setup is used for all test cases (unless stated otherwise), and was tested and validated by means of grid sensitivity and convergence studies. All presented calculations use the set of consistent closure coefficients for ABL flows stated in table 2.1. Parameters like roughness length, z_0, geostrophic wind, G, Coriolis parameter, f_c, and surface temperatures, θ_0, are site specific and summarized in tables in the specific sections.

The following two sections briefly describe the method that was developed to simulate non-neutral ABL flow over flat and complex terrain respectively.

3.6.1 Flat terrain

When simulating diurnal cycles over flat terrain, a simple forcing is applied: a constant pressure gradient results in a constant geostrophic wind speed and a prescribed surface temperature or heat-flux at the wall boundary imposes different stabilities.

The wall temperature varies in time and is repeated cyclically every 24 h. Simulations are continued for several days, until a cyclical solution is obtained. This ensures that all flow variables are in equilibrium with the model equations, and that the solution does not depend on the initial conditions anymore. Usually, calculations are proceeded for six days, while typically after about three

consecutive days an approximately cyclic solution is obtained.

To drive the flow, a constant pressure gradient is applied throughout the domain. On top of the ABL, away from the surface-layer, frictional forces vanish and the Coriolis force is balancing the pressure gradient force. This results in a constant geostrophic wind speed, G, on top (free stream atmosphere). In reality, the geostrophic wind changes its direction and magnitude in time and throughout the ABL. In the present study the pressure gradient that is used as a model input is constant in space and time, and therefore possible influences of large scale pressure systems are not taken into account. The resulting geostrophic wind velocity components are determined by the horizontal pressure gradient: $(u_G, v_G) = 1/(\rho f_c) \left(\partial P/\partial \mathrm{y} , \partial P/\partial \mathrm{x} \right)$. The Coriolis force balances the pressure gradient force at the ABL top, where friction by definition is zero. Closer to the ground, the pressure gradient force is balanced by the sum of the Coriolis force and the frictional force.

3.6.2 Complex terrain

Simulations of non-neutral ABL flow over terrain are divided in two parts. First, a precursor simulation simulates a typical diurnal cycle over flat terrain following the approach described above. The goal is to obtain the horizontally homogeneous flow field for different stabilities that would be observed over flat terrain. In a second step, the results obtained from the precursor simulation are used to specify the initial and transient boundary conditions for the complex terrain domain. This allows the flow to be computed at much lower cost, since the necessary spin-up time of several days is reduced to just a few hours (physical time in the simulation domain).

3.6.2.1 Precursor simulation

To simulate a site specific diurnal cycle, the flat computational domain is used (see section 3.5.1) together with a site specific roughness length, Coriolis parameter and surface temperature variation. A transient simulation is continued for several days until a cyclical solution is obtained. The resulting time-varying vertical profiles of wind speed, temperature, turbulence variables and the global maximum mixing length are stored every 10 min (physical time in the simulation domain), and provide the initial and transient boundary conditions for the complex terrain simulation. The transient complex terrain simulation is typically run for 24 h starting at midnight and using a 10 s time step. The wall boundary condition and the lateral inlet boundary conditions are unsteady. The

values for wind speed, temperature, turbulence variables and maximum global mixing length are all set according to the results obtained from the precursor simulation and are updated at every time step. To determine the values for the flow variables at the inlet boundaries, the results from the precursor simulation are interpolated linearly in both space and time. No spatial variations in surface heating are considered and the surface temperature is therefore a function of time alone. When starting a terrain simulation, the whole flow field is initialized with the horizontally homogeneous flow field obtained from the precursor simulation. Convergence studies have shown that it typically takes up to 2 h (physical time in the simulation domain) until the flow field in the domain has converged, and reflects the effects of the terrain correctly. After this time the flow field in the domain is the same than the flow field obtained from a simulation using a longer spin-up time ($\gg$2 h).
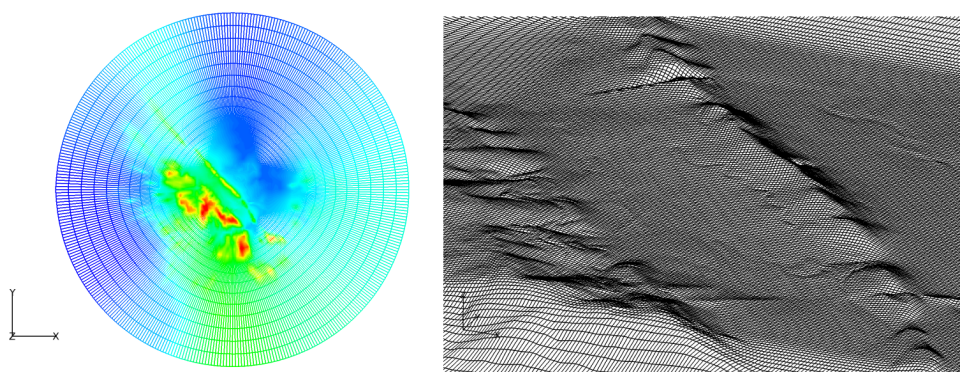
Figure 3.2: Surface grid of the Benakanahalli hill in India. Left: top view; right: detailed view of the grid at the instrumented hill (seen from southern direction). Note that for better illustration the polar grid on the left is only shown on grid level 2.
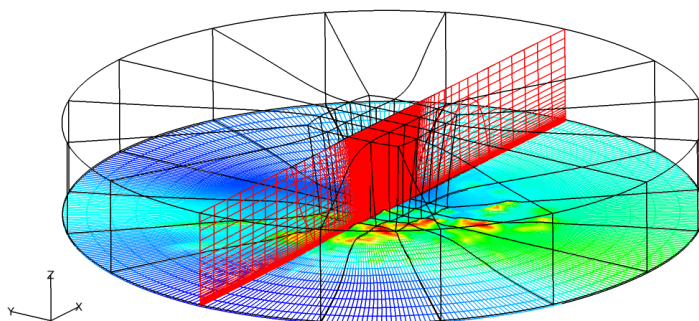
Figure 3.3: Volume grid of the Benakanahalli hill in India. Note that for better illustration the grid is only shown on grid level 2. Red lines show a vertical cross section of the cells and black lines show the block structure.

CHAPTER 4

Simulation of ABL flow over flat terrain

This chapter focuses on assessing how well the developed ABL model performs in representing ABL flows over flat homogeneous terrain. The flow variables are therefore functions of the height, z, alone.

First, two test cases considering neutral ABL flow are considered. The aim is to test the implementation of the length-scale limiter (section 2.4.1), the Coriolis effect (section 2.3) and the ambient turbulence values (section 3.1.2). Measurements of the neutral ABL are considered and results are compared against two datasets: the Leipzig profile (Lettau, 1950) and measurements from the Cabauw site in the Netherlands (van Ulden and Holtslag, 1980). The flow in the neutral ABL is assumed to be stationary, so that the ASL and the ABL model are both run steady-state. The necessary simulation parameters for both test cases are given in table 4.1 and the computational grid from section 3.5.1 is used.

Second, non-neutral ABL flow is considered. Non-neutral conditions in the ABL are typically induced by diurnal variations of the surface conditions (see section 4.5.1). To get a better understanding of the influences of the different stability classes on the resulting shear flow in the ABL, and to validate the ABL model, simulations of the diurnal cycle in the ABL are considered in this chapter.

Before simulating turbulent ABL flow at full scale, the implementation of the temperature equation 2.15 into the EllipSys3D solver is tested using laminar flow at small scale. Therefore 2D simulations of a differentially heated lid-driven square cavity (LDC) are conducted. The differentially heated LDC is an excellent candidate to gain insight into the involved fluid mechanical phenomena and to validate incompressible flow solvers. This standard CFD test case is dynamically very complex and displays the coupled convective heat transfer problem. It has been studied extensively and a vast amount of benchmark literature is available. The resulting flow includes the effect of thermal stability and computed results are compared against previous benchmark simulations (Babu and Korpela, 1993; Iwatsu and Hyun, 1995; Erturk and Gokcol, 2004; Ghia et al., 1982; Zhang, 2000; Botella and Peyret, 1998; Bruneau and Saad, 2005; Cheng and Liu, 2010). Results of this preliminary test case are shown in the Appendix (section 8).

Two test cases of non-neutral ABL flow over flat terrain at full scale are considered. The resulting high Reynolds number flow is now fully turbulent and subjected to the Coriolis effect. Turbulence is modeled using the modified k-ϵ turbulence model (equation 2.17) and the ABL model accounts for Coriolis and stability effects (see section 2.3). The considered test cases focus on the diurnal cycle in the ABL. First, a study from Mellor and Yamada (1974) is used, where diurnal cycles are simulated using a time-varying surface temperature. The diurnal cycles are based on experiments from the Wangara experiment, presented by Clarke (1971), but have been simplified. The aim of this test case is to understand the effect of time-varying surface temperatures on the computed flow, and to see how well the ABL model performs in representing the diurnal cycle in the ABL. Results from the ABL model are compared against simulations from Mellor and Yamada (1974). Next, observations from the GABLS2 test case held in Kansas, USA (Svensson et al., 2011) with a strong diurnal cycle are chosen to validate the ABL model. In their model intercomparison study Svensson et al. (2011), this case has shown to be a challenging test for ABL models, and the numerical and observational data presented by them are compared against results from the ABL model.

4.1 Test case: Leipzig

In this case the famous Leipzig wind profile is modeled and compared to measurement data from Lettau (1950). Results are shown in figure 4.1 together with the measurements. The left plot shows the wind speed component, u, parallel to geostrophic wind, G, plotted over height, and the middle plot shows the wind speed component, v, perpendicular to geostrophic wind, G, plotted over height.

Table 4.1: Values for the simulation parameters associated with the model runs: geostrophic wind speed, G, roughness length, z_0, Coriolis parameter, f_c, maximum global mixing length scale, l_e, and potential surface temperature, θ_0.

Test case	Stratification	Solution method	G [m/s]	z_0 [m]	f_c [1/s]	l_e [m]	θ_0 [K]
Leipzig	neutral	steady-state	17.5	0.30	1.13×10^{-4}	41.8	-
Cabauw	neutral	steady-state	10.0	0.15	1.15×10^{-4}	23.6	-
GABLS2	non-neutral	transient	9.5	0.03	8.87×10^{-5}	eq. 2.20	Fig. 4.5a
M&Y	non-neutral	transient	18	0.05	8.8×10^{-5}	eq. 2.20	Fig. 4.5a

In the right plot, the turbulent mixing length scale, l_t (see equation 2.7), is plotted over height.

Comparison of the ASL and ABL model results shows the influence of the Coriolis effect: the additional body force in the ABL model induces a velocity component, v, perpendicular to the direction of the geostrophic wind, G, and causes the wind to veer with height. In the ABL model, also the height of the ABL is now limited to about 1300 m. This can be seen in the middle of figure 4.1, where the velocity component, v, approaches zero. This is due to the applied length-scale limiter, which now limits the global maximum mixing length to $l_e = 41.8$ m, as seen in the right plot in figure 4.1. With the chosen value of $l_e = 41.8$ m the ABL height is however slightly overpredicted. This length scale is slightly larger than the one suggested by Apsley and Castro (1997) who used $l_0 = 36$ m for their simulation. It is generally accepted that the Leipzig experiment was actually conducted in slightly stable conditions (Zilitinkevich and Esau, 2002), and when using a lower length scale of $l_0 = 28$ m, the measured and simulated profiles agree perfectly (not shown here). However, the goal was not to match the simulation to a single observation, and the ABL model predicts the flow reasonably well, and simulated results are significantly improved compared to the neutral ASL model.

4.2   Test case: Cabauw

The neutral ABL over flat terrain at the Cabauw site in the Netherlands is simulated (van Ulden and Holtslag, 1980), and results are shown in figure 4.2. The non-dimensional geostrophic wind components, $(u - u_g)/u_{*0}$ and $(v - v_g)/u_{*0}$, are shown as functions of the non-dimensional height, $z f_c/u_{*0}$, plotted with a logarithmic scale, where $u_{*,0}$ is the friction velocity at the surface. Annual
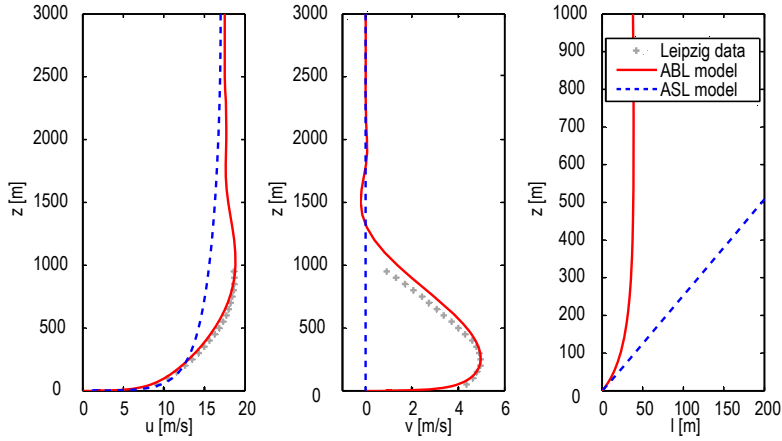
Figure 4.1: Wind speed components and turbulent mixing length scale l_t of the Leipzig test case using the ASL model (dashed blue) and the ABL model (solid red) shown together with the measurements from Lettau (1950) (grey symbols).

averages from the Cabauw site (van Ulden and Holtslag, 1980) are shown for three classes of the geostrophic wind ($G = 5, 10, 15$ m/s) at heights 10, 80 and 200 m, together with simulation results using $G = 10$ m/s. When plotted using above non-dimensional form, the simulation results for other geostrophic winds are indistinguishable. The right plot of figure 4.2 shows the turbulent mixing length scale, l_t (see equation 2.7), plotted over height.

As for the Leipzig test case, the turning of the wind with height induced by the Coriolis force, and the limitation of the ABL height by the length-scale limiter, can be seen when comparing the results of the ABL model with the ASL model. Results from the ABL model agree well with the measurements (van Ulden and Holtslag, 1980) and the chosen modifications prove applicable.

4.3 Test case: Mellor and Yamada

In this test case the diurnal cycle is simulated using the diurnally varying surface temperature taken from the study of Mellor and Yamada (1974), as shown in figure 4.3. In their study, numerical results from model runs using three different turbulence closures of varying complexity are presented. Here, only comparisons against results from their level 2 turbulence closure are presented, which neglects
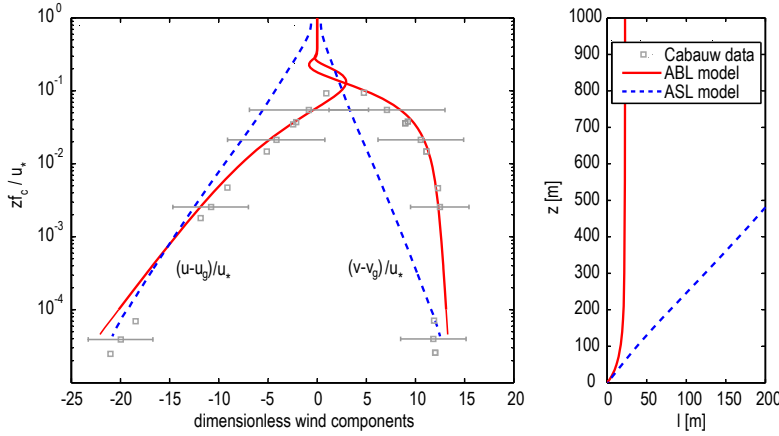
Figure 4.2: Dimensionless wind components and turbulent mixing length scale
l_t of the Cabauw test case using the ASL model (dashed blue) and
the ABL model (solid red) shown together with annual averages
of the Cabauw measurements from van Ulden and Holtslag (1980)
(grey symbols). Bars denote standard deviations.

second order terms, and is closest to the two-equation k-ϵ model of the present
ABL model.

The necessary simulation parameters and the computational grid are given in
table 4.1 and section 3.5. Non-neutral conditions are induced by the prescribed
time-varying ground temperature given in figure 4.3, and the initial temperature
profile is given by $\theta(z, 0) = 285$ for $z \leq 1$ km and $\theta(z, 0) = 285$ K+3.5 K/km
$(z - 1$ km) for $z > 1$ km. Calculations are proceeded for seven days, while
after three days an approximately cyclical solution is obtained. Note that the
coefficient α in the length-scale determining equation 2.20 is set to $\alpha = 0.1$
instead of $\alpha = 0.075$ in the present calculations to be consistent with Mellor
and Yamada (1974). Using $\alpha = 0.1$ yields a slightly greater ABL height for
neutral conditions compared to $\alpha = 0.075$.

4.3.1   Results

Results of the ABL model are compared against previous simulations of Mellor
and Yamada (1974) in figure 4.4. The plots in the left and middle column show
the computed evolution of the potential temperature, the velocity components,
and the turbulent kinetic energy, and plots in the right column compare profiles
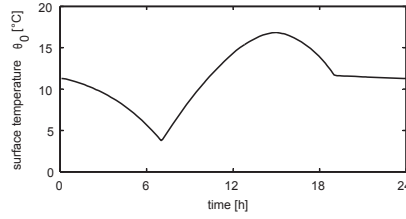
Figure 4.3: Surface temperature θ_0 from Mellor and Yamada (1974) that is given as input to the ABL model.

from both models at different times of the day.

Generally, the agreement is good and within the whole domain similar flow patterns are visible. The potential temperature shown in the first line evolves similarly in both models. Between 18:00 and 7:00 the flow below 500 m is stably stratified due to buoyancy forces that suppress vertical motion. After 7:00 the surface temperature increases until about 14:00 (see figure 4.3) accounting for solar radiation. Now an unstable layer starts to develop near the ground and warm air starts to rise upwards. The resulting convective turbulence is effective in homogenizing the flow: the stable layer is eroded and the ABL continues to grow. This results in near neutral conditions between 15:00 and 18:00. The flow within the whole ABL is well mixed and it is during this period that the ABL reaches its maximum of about 1800 m (one common definition for the ABL height is the level where the turbulent kinetic energy reaches 5 % of its surface value). In the top left plot of figure 4.4a, mean temperature difference between the present results and the results from Mellor and Yamada (1974) of about 1 K are visible in the middle of the ABL. One obvious reason for this are the different turbulence closures that are employed within the models. The model of Mellor and Yamada is found to be more dissipative, leading to larger turbulent length scales, l_t, when compared to the ABL model (not shown here). Due to the higher amount of turbulent mixing during daytime, warm air close to the surface penetrates higher up, resulting in slightly higher temperatures within the middle part of the ABL. The velocity component parallel to the geostrophic wind, shown in the second line of figure 4.4, shows the same distribution of minima and maxima. During stable conditions at night and early morning velocity maxima of about 22 m/s exist well below 500 m, corresponding to a low-level jet. At about 7:00 the low-level jet reaches its minimum height, which agrees well with the simulations from Mellor and Yamada. Also the velocity component normal to the geostrophic wind, shown in the third line of figure 4.4, show similar patterns for both models. Maximum values of around 8 m/s can be found close to the ground just before sunrise at 8:00, while values drop to around 5 m/s during daytime. Also the behavior of the turbulent

kinetic energy, shown in the bottom of figure 4.4, agrees well between both models. In summary, the computed vertical distributions of velocity, potential temperature and turbulence values show similar general patterns as the results from Mellor and Yamada. The ABL model performs well in representing the diurnally varying ABL when time-varying surface temperatures are applied at the bottom wall.
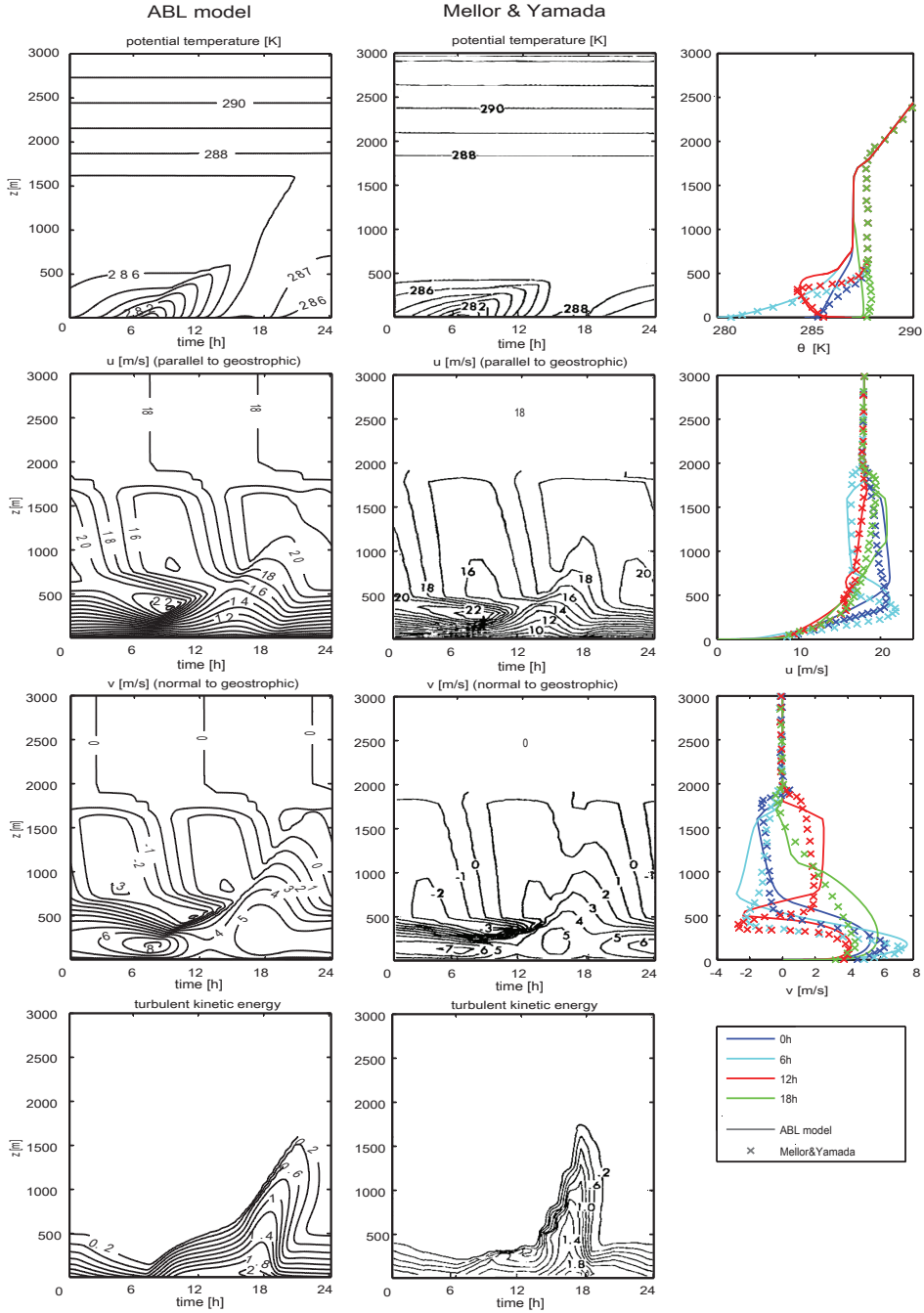
Figure 4.4: Evolution of potential temperature, velocity components, and turbulent kinetic energy over 24 h plotted over height. left column: ABL model results, middle colum: results from Mellor and Yamada (1974), right column: comparison of profiles from both models at different times of the day.

4.4   Test case: GABLS2

The GABLS2 test case held in Kansas, USA (Svensson et al., 2011) with a strong diurnal cycle is simulated with the ABL model and compared to observations. In the study of Svensson et al. (2011), the observational dataset is compared against simulation results from 30 different models. Simulating the described diurnal cycle has shown to represent a challenging test case for ABL models.

The simulation uses the computational grid described in section 3.5.1 and the ABL is simulated with the ABL model run transient. The necessary simulation parameters are chosen according to Svensson et al. (2011) and summarized in table 4.1. Non-neutral conditions are induced by the time-varying ground temperature given in figure 4.5a. A time step of 1 s with 8 subiterations is used. The initial conditions for the simulation of the diurnal cycle are given in Svensson et al. (2011).

4.4.1   Results

Results are shown in figure 4.5. Figure 4.5a shows the time varying ground temperature that is given as input to the ABL model. The resulting potential temperature field within the first 300 m adopts to the changing surface conditions, and the computed temperature field is also shown in figure 4.5a. The surface stability conditions are influencing the generation of turbulence and the turbulent mixing. Figure 4.5b shows the variation of the friction velocity at the surface on the left axis, and the velocity variation at the 10 m level on the right axis. Also shows are the measurements (symbols) and the spread of the different model results from the intercomparison study of Svensson et al. (2011) (shaded region).

In both plots, 4.5a and 4.5b, a clear transition between day- and nighttime is visible after sunrise around 8:00 and after sunset around 18:00. Stable nighttime conditions before 8:00 are characterized by small turbulence levels and a low ABL depth. The stable stratification suppresses the generation of turbulence, and results in turbulent kinetic energy values close to zero. The flow is effectively decoupled from the ground, and therefore the friction velocity at the surface is small, as shown in figure 4.5b. The air close to the ground is colder then the air above, and due to the small amount of mixing, only penetrates up to heights of about 100 m, where a steep temperature gradient is visible in figure 4.5a.

During daytime, between 12:00 and 18:00, unstable conditions are induced by the heating of the ground. Large amounts of convective turbulence lead to a

well mixed ABL with a greater depth. Due to convection, warm air is rising upwards and penetrates the strong stable temperature gradient that is capping the ABL during night. After 12:00, the stable gradient is not existent anymore and the ABL continues to grow in height. It is during this period that the turbulent length scales reach their maximum values. At around 14:00 the maximum temperature is reached, and before returning to the stable nighttime regime, the ABL is close to neutral at around 18:00, where the potential temperature is nearly constant with height.

Also shown in figure 4.5b is the evolution of the wind speed at the 10 m level. Higher wind speeds are observed during daytime, where the increased turbulence is effective at mixing momentum downward close to the ground and vice versa. The shaded areas indicate the model spread of the 30 models that were intercompared within the study of Svensson et al. (2011). Computed results generally are within the observed range and a clear diurnal pattern is visible. Svensson et al. (2011) report that all models underestimate the 10 m wind speed after the morning transition, and tend to overestimate the wind speed towards the end of the day. One obvious reason for this is that the geostrophic wind during the simulations is kept constant in space and time, while both, observations and mesoscale simulations shown in Svensson et al. (2011) show a decrease of the geostrophic wind during the observational period. Also note that the measured turbulent kinetic energy shows a sudden increase at about 3:00 which was reported to be a local disturbance not included in the model forcing, and therefore not present in the computed results.

Figure 4.5c shows the computed wind profiles in the first 100 m at different times of the day compared against the observations and the standard logarithmic profiles from the ASL model. Also shown are the theoretical profiles provided by MOST (see section 4.5.1) where the computed surface heat flux, H_0, together with equations 4.2 and 4.6 is used to determine the Obukhov length, L, and the modified logarithmic wind profile. Stable conditions at night are characterized by less mixing and higher shear. The small amount of turbulent mixing is not effective in mixing momentum downward, resulting in smaller wind speeds close to the ground and higher wind speeds above, when compared against the logarithmic profile. During daytime, unstable conditions enhance the generation of turbulence which results in a well mixed surface-layer with a rapid increase of wind speed over the first few meters, and an almost constant velocity above. The agreement is good, and the developed model captures the observed and theoretical non-neutral behavior.
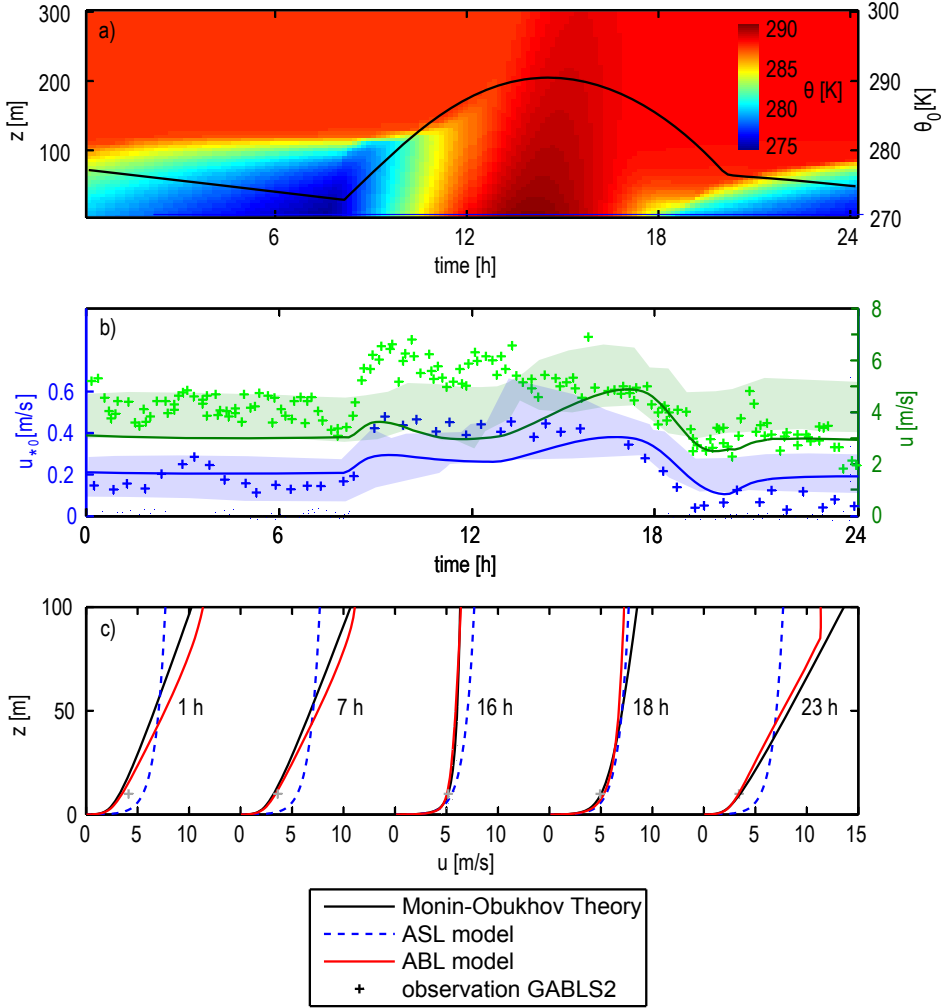
Figure 4.5: Evolution of modeled (a) surface temperature θ_0 (black line) and resulting potential temperature field within the first 300 m, (b) wind speed at 10 m (green) and friction velocity at the surface (blue) together with measurements (symbols) and spread of other models (shaded), (c) wind profiles of the ASL model and ABL model compared against analytical profiles from MOST.

4.5   Test case: MOST

In this test case MOST is used to assess the performance of the ABL model. First MOST is briefly described in 4.5.1, and the resulting analytical solutions are then compared to observations and model results in 4.5.2.

4.5.1   Monin-Obukhov similarity theory

Non-neutral conditions influence the resulting wind profiles, and they deviate significantly from the idealized logarithmic profile (see e.g. figure 1.3). Monin-Obukhov Similarity Theory (Monin and Obukhov, 1954) accounts for stability effects and expresses the vertical structure of the horizontally homogeneous non-neutral ASL as dimensionless universal functions. It is often used to validate numerical models for atmospheric flow. Based on dimensional analysis, all non-dimensionalized mean flow properties within the ASL only depend on a reduced set of key scaling parameters: the friction velocity at the surface, $u_{*,0}$, the height above ground, z, and the vertical turbulent heat flux, H:

$$H \equiv \overline{w'\theta'} \approx \frac{\mu_t}{\sigma_\theta} \frac{\partial \theta}{\partial z}. \tag{4.1}$$

From these parameters a universal length scale, the Obukhov length, L, can be formed that describes the exchange processes in the surface-layer:

$$L = -\frac{u_{*0}^3 \theta_0}{\kappa g H_0} \ , \tag{4.2}$$

where θ_0 is the potential temperature at the surface and H_0 is the near-surface value of the vertical turbulent heat flux, H. L is proportional to the vertical potential temperature gradient and describes the height at which buoyant production of turbulence first exceeds mechanical production due to shear. The dimensionless height, $\zeta = z/L$, is used as a stability parameter and has the same sign as the Richardson number, Ri: positive in stable conditions and negative in unstable conditions. Based on the assumptions that the flow within the surface-layer is stationary, horizontally homogeneous, and that fluxes are independent of height, ζ is now constant throughout the surface-layer (in contrast to Ri), and the normalized wind speed depends on the universal function ζ alone:

$$\phi_m\left(\zeta\right) = \frac{\partial u}{\partial z}\left(\frac{\kappa z}{u_*}\right). \tag{4.3}$$

For ideal conditions of stationary and horizontally homogeneous flow MOST is valid in the ASL where the Coriolis effect is negligible. The form of the stability

function ϕ_m is not known from dimensional analysis and is obtained empirically from field experiments over flat terrain: measurements for different values of ζ are substituted into equation 4.3, and curves are fitted to the resulting data. Despite numerous field experiments there are still discrepancies in the literature for the exact form of ϕ_m. The formulation chosen here is widely used and known as the Businger-Dyer relation (Businger et al., 1971; Dyer, 1974):

$$\phi_m = \begin{cases} 1 + \partial_m \zeta & \text{for } \zeta \geq 0 \\ (1 - \gamma_m \zeta)^{-1/4} & \text{for } \zeta < 0 \end{cases} . \tag{4.4}$$

In the literature the coefficient ∂_m ranges from 4 to 10, and γ_m ranges from 15 to 28 (Högström, 1996; Li et al., 2008). During ideal conditions, the relation 4.3 between dimensionless wind shear and dimensionless height ζ is valid for any wind speed, height, roughness and stability condition in the surface-layer. Ideally vertical profiles will then collapse on one line.

Integration of equation 4.3 for the velocity gradient yields a modified logarithmic wind profile for the wind speed U:

$$U = \frac{u_*}{\kappa} \left[\ln\left(\frac{z}{z_0}\right) - \Psi_m(\zeta) \right] , \tag{4.5}$$

where Ψ_m is a stability function. Using the Dyer stability functions (Panofsky and Dutton, 1984), Ψ_m is defined as:

$$\Psi_m = \begin{cases} -5\zeta & \text{for } \zeta \geq 0 \\ \ln\left[\left(\frac{1+x^2}{2}\right) \left(\frac{1+x}{2}\right)^2 \right] - 2atan(x) + \frac{\pi}{2} & \text{for } \zeta < 0 \end{cases} \quad \text{with } x = (1-16\zeta)^{1/4} . \tag{4.6}$$

Examples of the resulting analytical profiles are shown in section 4.4.

4.5.2   Results

In figure 4.6 MOST is used to assess the performance of the ABL model. Theoretical ϕ_m functions are shown together with simulation results from the GABLS2 test case and experimental data from several field campaigns (Businger et al., 1971; Li et al., 2008; Klipp and Mahrt, 2004). Results from the ABL model are shown for $z < 50$ m (red symbols). The shown analytical expression for ϕ_m is based on equation 4.4 with $\partial_m = 5$ and $\gamma_m = 15$ (solid black). A range of
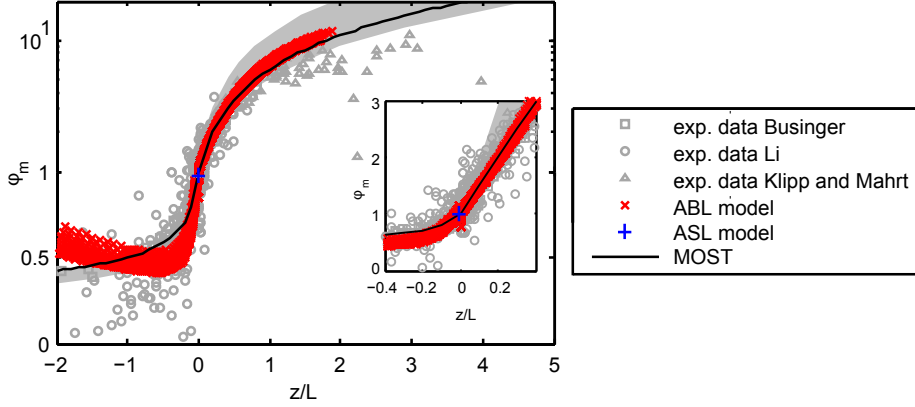
Figure 4.6: Stability function ϕ_m from observations (grey symbols), range of analytical expressions from MOST (solid black and shaded) and results from the ABL (red) and ASL model (blue).

analytical solutions where ∂_m varies from 4 to 10 and γ_m varies from 15 to 28 (Sogachev et al., 2012) is also shown (shaded area).

To decrease the spread of the experimental ϕ_m values the data needs to be selected carefully. Especially during transitional periods in the morning and evening the assumptions underlying MOST (stationary and horizontally homogeneous flow with constant ζ over height) are violated in real ABL flows. The shown simulation results are therefore selected accordingly: only cases for fully developed flow away from the transitional periods are shown, and results during transitional regimes around 8:00 (sunrise) and 18:00 (sunset) are omitted. MOST was derived for the range $|\zeta| < 2$ (Businger et al., 1971) and for higher values experimental and simulation results start to deviate from MOST.

In the left plot in figure 4.7 the stability function ϕ_m is shown for one full diurnal cycle (24 h), without filtering transitional regimes. ϕ_m is determined in three different heights (2, 10 and 50 m) and ζ is determined based on the surface heat flux, H_0. Model results are shown together with observational data from Businger et al. (1971), Li et al. (2008) and Klipp and Mahrt (2004). The solid black line represents the analytical MOST expression from equation 4.4 with $\partial_m = 5$ and $\gamma_m = 15$, and the shaded area represents the range of analytical solutions where ∂_m varies from 4 to 10 and γ_m varies from 15 to 28 (Sogachev et al., 2012). Especially during transitional regimes after sunrise at 8:00 and after sunset around 18:00 model results deviate significantly from MOST and z/L is not constant with height, which is a necessary assumption for MOST to be valid. During these periods the flow in the ABL is not in equilibrium with

the underlying surface conditions. The heat flux at the surface changes quickly, and the response of the ABL to adopt to those changing conditions is delayed. Because of the atmosphere's inertia, the flow in greater height takes longer time to respond to the changes in surface heat flux. This can be seen in the right plot in figure 4.7, where the heat flux, H, is plotted over height for different times of the day. During the transitional regimes at 9:00 and 19:00 the heat flux is not constant with height. Solid blue and red lines denote fully developed stable and unstable flow respectively, while the dashed lines represent transitional regimes. At 9:00 the heat flux decreases with height and has different signs: close to the surface the increasing temperatures have started to erode the stable nighttime layer (positive heat flux), while the flow above has not adopted to the new surface condition yet, and the flow is still stably stratified.

Note that for the cases shown here the ABL model is run for several days, cyclically repeating the surface temperature from the GABLS2 test case, until a cyclical solution is reached. This ensures that the whole flow field is in equilibrium with the model equations, and that the solution is independent of the initial conditions. For the GABLS2 model intercomparison, the spin-up time of the models given in Svensson et al. (2011) (time before numerical and observational data is compared) is only 8 h. It was found that after just 8 h, at least for the present model, the solution is still significantly dependent on the initial temperature field, and when compared against MOST, the agreement is not as good as for the fully converged results. This indicates that the flow field in the ABL after 8 h of spin-up time is not yet in equilibrium with the surface forcing at the ground. In a recent study, Sogachev (2009) also found that a spin-up time of several days is needed, depending on the initial conditions.

4.6   Summary

This section assesses the applicability and performance of the ABL model that accounts for Coriolis and stability effects. Five test cases are considered. The first two test cases considered in the section are similar, and focus on neutral ABL flow. The computed flow profiles agree well with the two datasets, and the implementation of the length-scale limiter, the Coriolis effect and ambient turbulence values prove applicable. Results from the ABL model are significantly improved compared to the neutral ASL model: the length-scale limiter effectively limits the ABL height and the Coriolis effect induces the Ekman spiral.

The following test cases focus on non-neutral ABL flow. Before considering ABL flow at full scale, a preliminary study was used to validate the effect of
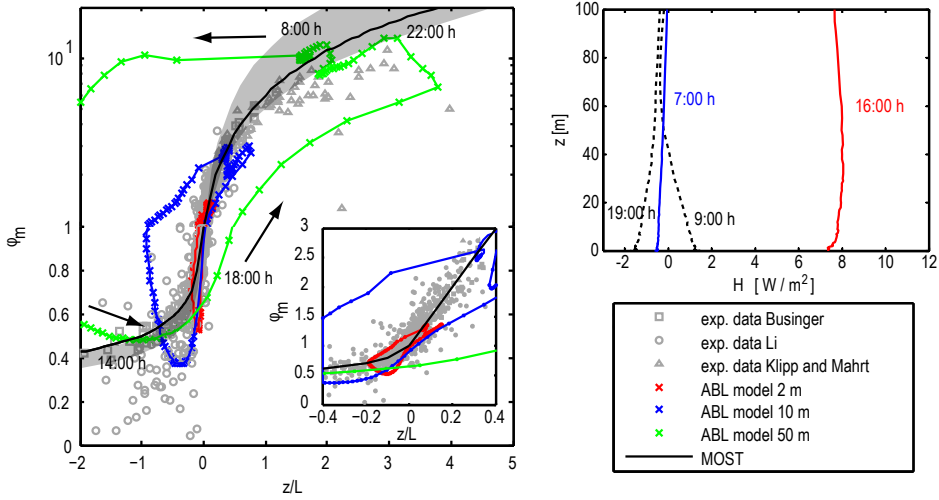
Figure 4.7: Left: Stability function ϕ_m from the ABL model (colored lines and symbols), observations (grey symbols), and MOST expressions (solid black and shaded) shown for one 24 h cycle. Right: modeled heat flux H plotted over height for stable (blue), unstable (red) and transitional regimes (dashed).

thermal stratification by solving the incompressible Navier–Stokes equations of the coupled convective heat transfer problem in a differentially heated LDC. The good agreement shows that the solver is adequate to solve the mixed convection problem like the one presented (see appendix 8).

Two test case with ABL flow at full scale are considered, where diurnal cycles are simulated using time-varying surface temperatures. For the Mellor and Yamada test case, the resulting vertical distributions of velocity, potential temperature and turbulent kinetic energy of the models agree well, and the diurnal variation of the ABL structure is satisfactorily reproduced. For the GABLS2 test case, the ABL model is able to reproduce the diurnal flow pattern. Simulated results generally compare well with measurements and the results of other models. During early morning, however, agreement with measurements is less good. One obvious reason for this is the decrease of the geostrophic wind during the observational period, while the model forcing is kept constant. Finally, MOST is used to assess the model, and results agree well with the theory, for cases where the underlying assumptions of horizontal homogeneity and stationarity are approximately true.

In summary, the model results agree best with MOST when allowing the solu-

tion to fully converge to a cyclical solution. Agreement with the measurements from the GABlS2 test case is best, when following the instructions from Svensson et al. (2011). This indicates that if information on a large scale (like the geostrophic wind or the vertical temperature profile) is available from measurements, those conditions should be used in the model to compare numerical and observational data. However, conditions in the real ABL are often non-stationary and horizontally non-homogeneous, and are therefore not necessarily in agreement with empirical theories like MOST or with the model equations of numerical models.

The advantage of the developed ABL model is its general applicability, as no new model coefficients are necessary. All modifications in the k-ϵ turbulence model depend only on the local flow and are determined locally within the domain during the simulation. The modeled solution is therefore solely determined by the variation of the surface temperature and the standard model parameters summarized in table 4.1.

Simulation of non-neutral ABL flow over complex terrain

Having demonstrated the modifications necessary to model the non-neutral ABL over flat terrain, the aim of the present chapter is to analyze the combined Coriolis and stability effects over complex terrain and to validate their representation in the model.

Changes in surface elevation (hills, mountains, escarpments) can occupy a significant fraction of the ABL height and disturb the otherwise horizontally homogeneous and stationary shear flow. Also changes in surface roughness (buildings, obstacles, vegetation) cause the local profiles of wind speed, temperature and turbulence to be out of equilibrium. The flow responds to the changing conditions and the resulting flow structure is fully three dimensional and more complex than flow over flat terrain. Now the flow depends upon the position, and wind speed, temperature and turbulence values vary locally (acceleration on hilltop, deceleration in wake region, possibly flow separation).

Additional effects occur when the flow is thermally stratified. During unstable conditions, warm air rises along slopes due to positive buoyancy forces (anabatic wind), while during stable conditions cold heavy air tends to sinks downslope

Table 5.1: Values for the simulation parameters associated with the model run: geostrophic wind speed, G, roughness length, z_0, Coriolis parameter, f_c, maximum global mixing length scale, l_e, and potential surface temperature, θ_0. Due to the small scale of the wind-tunnel flow l_e and f_c are not applicable.

Test case	Stratification	Solution method	G [m/s]	z_0 [m]	f_c [1/s]	l_e [m]	θ_0 [K]
wind-tunnel	neutral	steady-state	2.5	2.30×10^{-3}	-	-	-
	stable	transient	1.0	2.30×10^{-3}	-	-	300.5
Benakanahalli	non-neutral	transient	10-18	0.1	8.87×10^{-5}	eq. 2.20	fig. 5.8

and settle in areas of lower elevation (katabatic wind). For strong stably stratified flow, changes in elevation can also trigger vertical oscillations (gravity waves, mountain waves).

Generally, the assumptions of horizontally homogeneous and stationary shear flow, upon which MOST is based (chapter 4.5.1), are violated for terrain flows. Therefore atmospheric experiments on full scale are necessary, to get a better understanding of the physical processes involved, and to validate ABL models. Various experiments that focus on neutral flow over complex terrain are available, e.g. the Askervein Hill experiment (Taylor and Teunissen, 1987), or more recently the Bolund experiment (Berg et al., 2010; Bechmann et al., 2011). Existing benchmark literature for non-neutral ABL flows mostly focuses on flat terrain (Businger et al., 1971; Li et al., 2008; Klipp and Mahrt, 2004), and test cases for complex terrain are scarce. The Benakanahalli field experiment was specifically designed to provide such a benchmark dataset (Berg et al., 2012). The field experiment took place in India in early 2010, and the topography and location of the site is well suited to study the combined non-linear effects of stability and Coriolis force over complex terrain.

Before considering non-neutral ABL flow at full scale, a wind-tunnel study from Ross et al. (2004) is considered. Neutral and stably-stratified boundary-layer flow over a steep hill is simulated and compared against simulations and wind-tunnel measurements (Ross et al., 2004; Wan and Porté-Agel, 2011). The wind-tunnel experiment was designed to represent realistic ABL flow over a two-dimensional steep hill. Wind-tunnel flows cannot fully resemble real ABL flow at full scale, and the Coriolis effect is negligible. However, this test case provides the possibility to study stability effects under controlled conditions, and is chosen to test the applicability and performance of the ABL model for flows over terrain. In the following section the Benakanahalli field experiment is presented and the resulting dataset is then used to validate the ABL model.
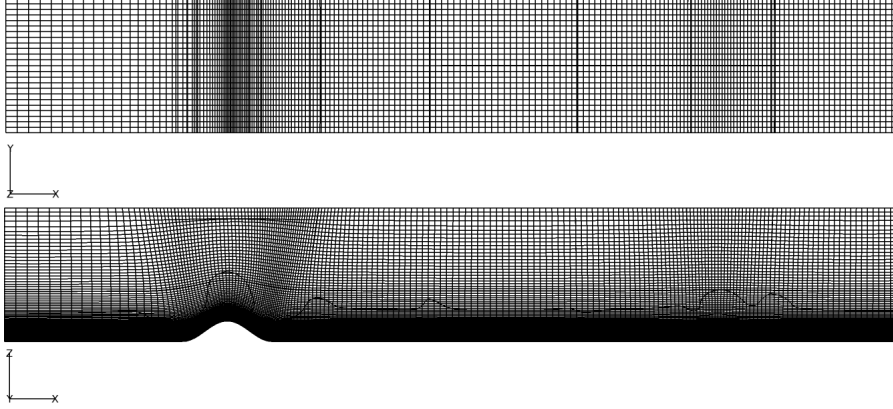
Figure 5.1: Computational domain to model the wind tunnel of the Environmental Flow Research Laboratory (EnFlo), University of Surrey, U.K.

5.1 Test case: neutral and stable flow over a steep hill

The hill in the wind tunnel study of Ross et al. (2004) is steep enough to induce flow separation, and represents a challenging test case for the developed ABL model. The simulation is run in transient mode with a time step of 0.1 s and 8 subiterations.

Due to the small scale of the wind-tunnel, the Coriolis effect is neglected in the model, hence equation 2.20 to determine a maximum length scale, l_e, cannot be applied, and no length-scale limitation is used.

The necessary input parameters to simulate the wind-tunnel flow are summarized in table 5.1. Two cases are simulated: neutral and stably stratified flow with a relatively weak stratification of about 10 K/m in the lowest 0.5 m and a much stronger stratification of about 40 K/m above. The neutral simulations are solved steady-state and the stable simulations are run transient for 150 s of model time (equivalent to 15 tunnel flow-through times) after which the computed flow has reached a quasi-steady state.

The wind-tunnel experiments were conducted at the Environmental Flow Research Laboratory (EnFlo), University of Surrey, U.K. The wind tunnel has a working section of 20 m length, 3.5 m width and 1.5 m height and the shape of

the two-dimensional steep hill is given by:

$$z = \begin{cases} h\cos^2(\pi x/l) & \text{, for } -l/2 \leq x \leq l/2 \\ 0 & \text{, elsewhere} \end{cases} \quad , \qquad (5.1)$$

where $h = 0.229$ m is the maximum hill height, x is the distance from the centre of the hill and $l = 1$ m is the width of the hill. The computational domain covers 10 m of the wind-tunnel test section, and is 1.5 m high and wide and the hill is placed 2.5 m behind the upstream boundary. The wind-tunnel flow is solved by the EllipSys3D solver and therefore the domain is 3-D, although the shape of the model hill and the resulting flow is 2-D. The grid has 192 grid points in the horizontal, 24 in the lateral and 96 in the vertical direction. Stretched cells are used in the vertical direction with a height of 0.27 mm at the wall and 5 cm at the top of the domain. In horizontal direction the mesh is refined on top of the hill with cells of 1.5 cm length and is stretched towards the inlet and outlet where cells are about 10 cm long. In lateral direction the mesh is equally spaced with the cells being 6 cm wide. At the upstream and top boundaries, inlet conditions are used, and at the downstream boundary outlet conditions are used.

The initial conditions for the neutral simulation are specified by the logarithmic wind profile with a surface roughness of $z_0 = 0.23$ mm (see table 5.1). For the stably stratified flow the inlet profiles at the upstream boundary are generated by running a precursor simulation: the experimental velocity and temperature profiles from the wind-tunnel given in Ross et al. (2004) are run through the ABL model using the wind tunnel specified below in absence of the hill. This ensures that the inlet profiles are in equilibrium with the model equations.

5.1.1 Results

Computed wind speed and turbulence properties of the neutral and stably stratified flow are compared against experimental results (Ross et al., 2004) and simulation results (Ross et al., 2004; Wan and Porté-Agel, 2011). Figure 5.2 shows contour plots of the streamwise velocity u in a vertical plane and figure 5.3 shows contour plots of the momentum flux $\overline{u'w'}$. Results for neutral flow are shown in the left column, and results for stable flow are shown on the right. In both cases flow separation occurs at the lee side of the hill. For the stable case, the depth of the wake region is slightly increased, because the stable stratification acts to suppress vertical motion. Above 0.5 m the strong temperature gradient of about 40 K/m is effectively capping the flow and turbulence is limited to the lower part of the domain. Compared to the neutral case, the turbulence level

is significantly reduced and the momentum fluxes are an order of magnitude
smaller. The ABL model captures the general effects induced by stratification,
although the size of the wake is different. For both, neutral and stably stratified
flow the recirculation region in the lee side of the hill is significantly overpre-
dicted compared to the wind-tunnel experiment, while it agrees well with the
LES results of Wan and Porté-Agel (2011). The velocity above of the hill is
generally predicted well. Also the $\overline{u'w'}$ values in figure 5.3 are predicted well
and agree with both wind-tunnel and LES results from Wan and Porté-Agel
(2011). However, for the neutral case the $\overline{u'w'}$ values upstream of the hill are
found to be too high when compared to the wind-tunnel values. Similar find-
ings were reported by Wan and Porté-Agel (2011): the model is found to be too
dissipative in this region which leads to an increased upwards deflection of the
flow induced by the hill and leads to a slower velocity recovery downstream of
the hill, and hence an overestimated wake region.

Since the ABL model was developed for ABL flows at full scale, one cannot
expect the model to reproduce the wind-tunnel measurements perfectly. Due
to the small scale of the wind-tunnel the Coriolis effect is neglected and the
length-scale limiter is not applied. The implemented turbulence closure has been
developed for steady ABL flows, and it cannot be expected that the unsteady
wake region in the lee of the hill is predicted correctly. The wake region has
shown to be sensitive to changes in the model constants. No coefficients were
adjusted and all test cases are run with the same set of constants from table 5.1.
Although this test case is of limited value to verify the developed ABL model,
it is shown that the model can be applied on curvilinear grids without any
modification, and that general effects of stratification on the flow are captured
correctly.

5.2   Test case: Benakanahalli hill

In early 2010 a yet unpublished field experiment took place close to the village of
Benakanahalli in the region of Karnataka, India, focusing on micro meteorologi-
cal properties important for wind energy. The field experiment is in many ways
the natural successor to the Bolund hill experiment (Bechmann et al., 2011).
Bolund, a 12 m sharp edged hill, proved suitable for validation of flow models
in neutral conditions, while the measurements at Benakanahalli can be used to
study the influence of non-neutral stratification and Coriolis force on the flow.
The experiment was planned and conducted as a joint collaboration between
DTU Wind Energy and Vestas Technology R&D.
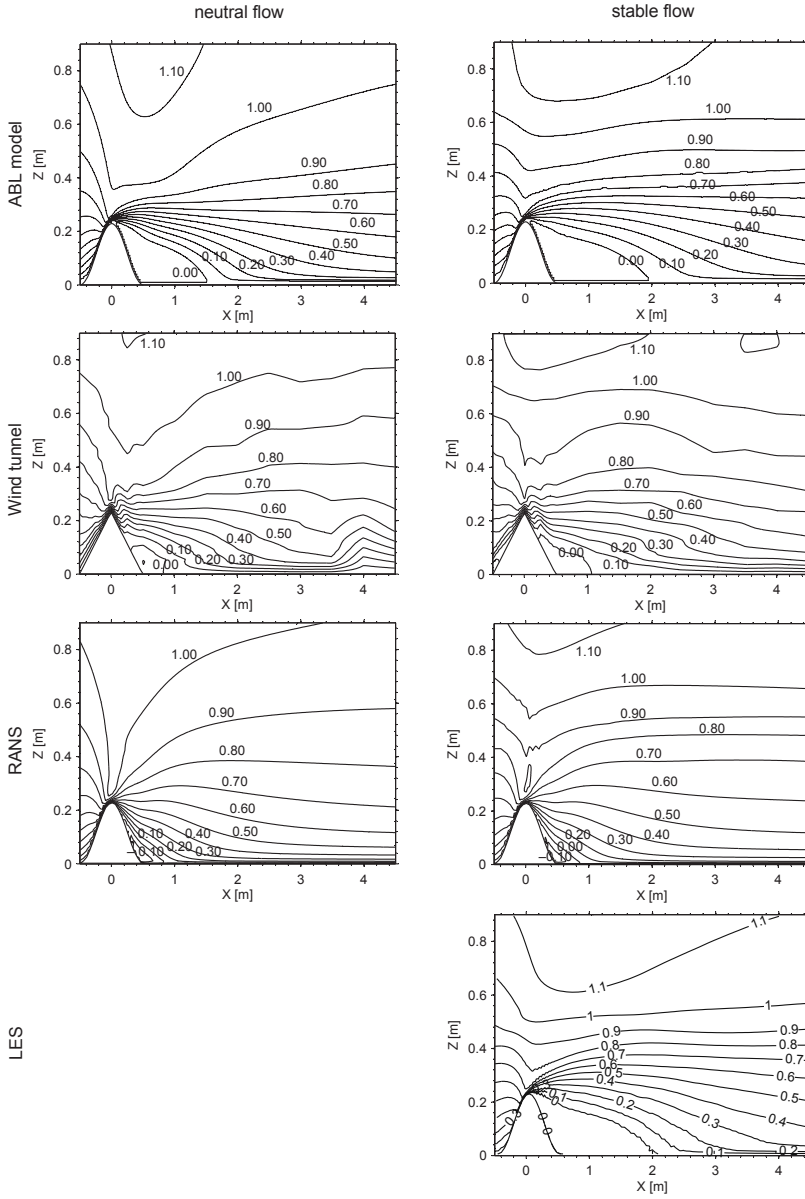
Figure 5.2: Contour plots of non-dimensional streamwise velocity u/u_f in a vertical plane across the hill for neutral (left column) and stable flow (right column). Simulation results are shown along with measurements and RANS results from Ross et al. (2004) and LES results from Wan and Porté-Agel (2011).
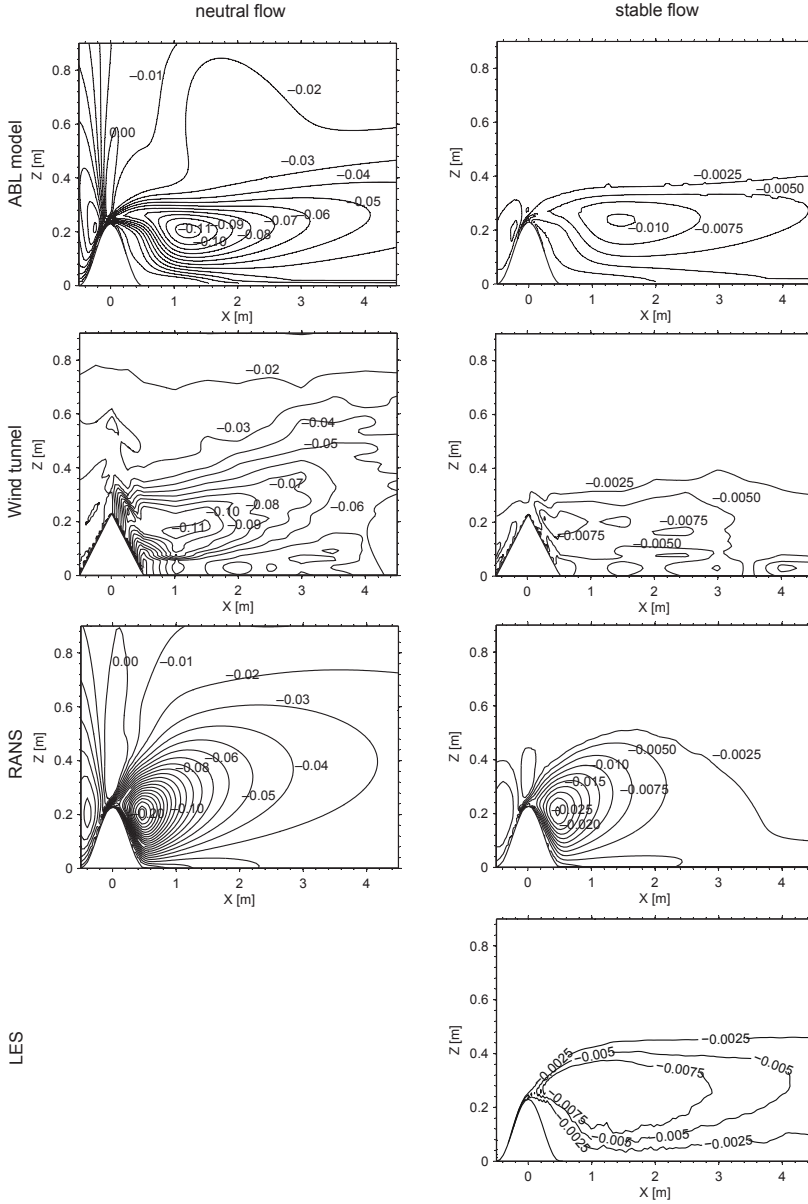
Figure 5.3: Contour plots of momentum flux $\overline{u'w'}$ (in m²s⁻²) in a vertical plane across the hill for neutral (left column) and stable flow (right column). Simulation results are shown along with measurements and RANS results from Ross et al. (2004) and LES results from Wan and Porté-Agel (2011).
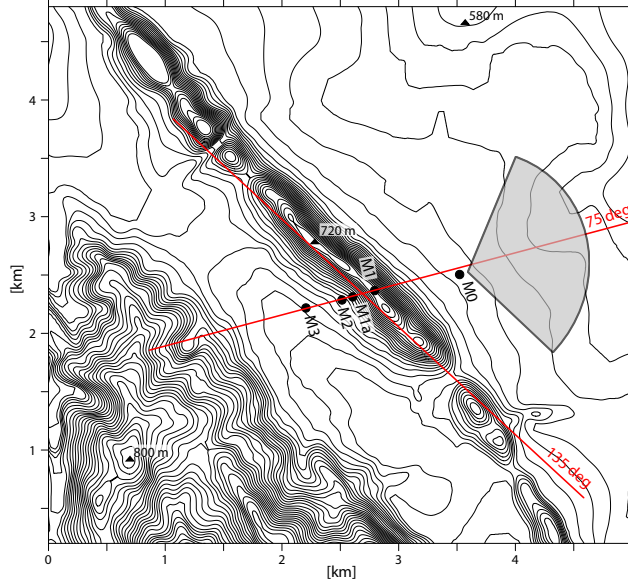
Figure 5.4: Contour map of surrounding terrain including mast positions M1,
M1a, M2 and M3 along the 75 ° transect, while the considered
wind direction of the present study is 135 °. The shaded area in-
dicates wind directions with near homogeneous inflow conditions.

5.2.1 Site description

The experimental site is located 15 km southeast of the village of Benakanahalli
(14 °10 ′34 ″ N, 75 °50 ′29 ″ E), and the measurements were conducted from
1st of February to 6th of April 2010. Five 80 m masts were erected along a
75 ° transect across the long almost two-dimensional 120 m high natural ridge
with slopes of around 30 ° (see Figure 5.4). All five masts were equipped with
sonic anemometers at five different heights. In addition temperature sensors
were mounted on the upstream mast M0 and in the soil nearby. Together with
measurements of heat flux from the sonic anemometers a good estimate of the
thermal stratification is thus obtained. The surrounding terrain is shown in
figure 5.5. There is a small village to the north, while the eastern and southern
directions are mainly covered by farmland: rice fields, corn plants and patches
of palms trees. This corresponds to a surface roughness of approximately $z_0 =$
0.1 m, which is used as an average roughness for the precursor simulations
and as a farfield roughness at the boundaries of the terrain domain. To take
roughness changes within the area into account, a roughness map is generated
as shown in 5.6. Based on the inspection of the landscape the wind coming from

Figure 5.5: Photo showing the Benakanahalli hill, seen from south-east. On the hill top the mast M1 is visible.
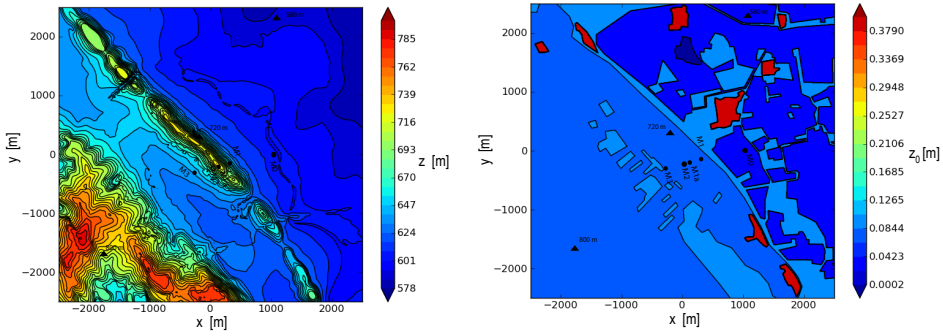
Figure 5.6: Left: elevation map around the Benakanahalli hill showing the height above sea level. Right: roughness map around the Benakanahalli hill showing the roughness length z_0.

between 35 ° and 135 ° were considered to have flat and close to homogeneous upstream conditions (indicated by shaded area in figure 5.4). This is ideal from a modeling perspective where simple upstream conditions are desired for validation purposes. Close to the 135 ° direction, however, the incoming wind shows slight perturbations from the otherwise ideal homogeneous conditions: small hills and a lake that are encountered 4-6 km upstream lead to internal boundary-layers and enhanced turbulence.

5.2.2   Experimental data

In figure 5.7 the wind rose of the resulting dataset, measured by the sonic at 75 m at mast M0, is presented. The experiment was designed for easterly winds and the transect was chosen accordingly. During the experiment, however, the
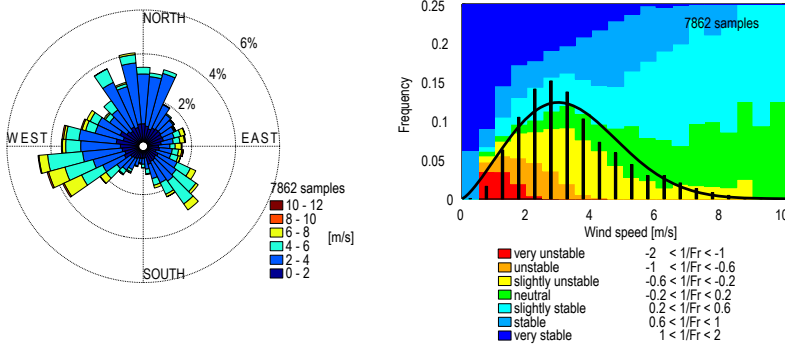
Figure 5.7: Wind climate as observed at the 75 m sensor of mast M0. Left: distribution of wind directions. Right: Frequency distribution of wind speeds together with fitted Weibull distribution (black). Colors denote 7 different stability classes that are classified based on the Froude number (equation 5.2).

wind blew predominantly from westerly and south easterly directions. With the instrumented transect located at 75 ° the experiment has not been ideal with only a fraction of the wind coming from this direction. The prevailing west-southwest wind direction is, from a modeling point of view, far from ideal, since the wind accelerates downhill from high elevations to the west, resulting in non-homogeneous upstream conditions. General for all wind directions is the very low wind speed (typically less than 4 m/s) and relatively high turbulence levels (larger than 20 %) due to the large surface roughness of the terrain. Having low wind speeds together with a very pronounced daily cycle of surface temperature, the wind is strongly affected by thermal stratification.

This can be seen in the right plot of figure 5.7 where the frequency distribution of wind speeds and their Weibull fit is plotted. The colors in the background denote different stabilities and are classified based on the Froude number:

$$Fr = \frac{\pi U}{N_{bv} W_T}, \tag{5.2}$$

where W_T is a characeristic length scale of the terrain and N_{bv} is the Brunt–Väisälä frequency:

$$N_{bv} = sign\left(\frac{\partial \theta}{\partial z}\right) \sqrt{\frac{g}{\theta_0} \left|\frac{\partial \theta}{\partial z}\right|}. \tag{5.3}$$

The Froude number is a non-dimensional parameter that is widely used to classify different flow structures that occur for non-neutral flow over mountains, and can be seen as a natural wavelength of the terrain. The Brunt–Väisälä frequency describes the buoyancy oscillations that occur when an air parcel in stratified flow is moved vertically away from its original position.

In the present case the Froude number was used to classify the observed wind climate at mast M0 into seven stability classes (see figure 5.7). The vertical temperature gradient is determined based on the two top temperature sensors of mast M0 at 40 m and 75 m height. $W_T = 500$ m was chosen, since the Benakanahalli hill is around 500 m wide. As shown in figure 5.7, strong stabilities typically occur for low wind speeds, where buoyancy effects are strong compared to mechanical shear. For high wind speeds, on the other hand, the effect of buoyancy is comparably small and the flow tends to be neutrally stratified.

5.2.3 Results

The simulations over the Benakanahalli hill are divided in two parts. First, a dataset of three consecutive days is extracted from the measurements, with the aim to model the observed diurnal variations. Second, data from the whole observational period is used and binned based on wind direction, wind speed and stability (Froude number). Then several diurnal cycles for different wind speeds and wind directions are simulated, and the computed results are binned accordingly, and compared against the measurements.

5.2.3.1 Precursor simulation

The goal is to reconstruct the vertical structure of the flow field for different stabilities as observed at the mast M0. Figure 5.8 shows the modeled and observed evolution of the velocity at 75 m and the temperature at 10 m at mast M0. The observed data represents a 3 day average shown with the corresponding error bars. Since the observed soil temperature has less amplitude than the 10 m temperature, the wall temperature to force the model was adjusted in order to match the observed temperature at 10 m (grey line in figure 5.8). The resulting modeled temperature at 10 m therefore follows the observed temperature well, having the same amplitude and a similar distribution of minima and maxima (black line in figure 5.8). The observed soil temperature is measured 2 cm in the ground. The observations show a decrease of wind speed around noon before the maximum temperature is reached at 16:00. This decrease of wind speed is delayed in the modeled results. Having the wall temperature and
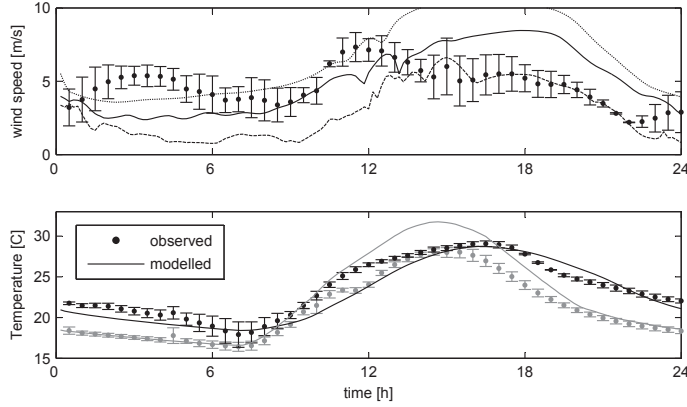
Figure 5.8: Time series of modeled and observed data at M0. Top: wind speed at 75 m height. Model results are shown for different geostrophic winds: 10 m/s (dashed line), 14 m/s (solid line) and 18 m/s (dotted line). Bottom: temperature at 10 m height (black), and surface temperature (grey).

pressure gradient as the only model forcing, the day and night-time transitions are dictated by the surface temperature alone. Therefore the modeled wind speed will only drop after the surface temperature drops as well. Using the temperature distribution from figure 5.8, one cannot expect the simulation to match the three days of measurements exactly. During a period of just three days the observed statistics might very well be influenced by large scale effects and advection. The influence of these effects is not included in the model, since the model forcing is determined based on local measurements at mast M0 alone. Applying a constant geostrophic wind of course limits the comparability with the extracted dataset, as such perfect cases do not occur in reality. The magnitude and direction of the geostrophic wind will in reality never be constant in time. Numerical tests show that the choice of the geostrophic wind has a significant effect on the resulting ABL flow: figure 5.8 shows the simulated evolution of the velocity at 75 m at mast M0 for different geostrophic winds. However, with the focus on stability, it was decided to compare the modeled and observed results for different stability classes, rather than adjusting the geostrophic wind to match the measurements. To evaluate the representation of stability effects in the model, non-dimensionalized velocity profiles for different stability classes are compared against the measurements. The Obukhov length determined in 10 m height is used to classify different stable and unstable conditions. Figure 5.9 shows the corresponding averaged dimensionless velocity profiles for different stability classes. Stability conditions for both modeled and observed results are categorized based on the Obukhov length: very stable $z/L > 0.2$, stable 1×10^{-3}
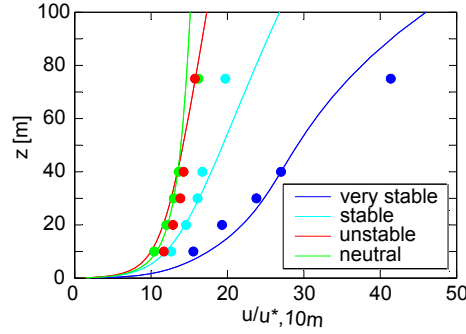
Figure 5.9: Averaged dimensionless velocity profiles for different stability classes. Stability conditions are categorized based on different Obukhov lengths.

$< z/L < 0.2$, neutral $-1 \times 10^{-3} < z/L < 1 \times 10^{-3}$ and unstable $z/L < -1 \times 10^{-3}$. The plot is based on observational data covering the whole field experiment (3 months), and simulation results from one representative diurnal cycle (1 day) with a geostrophic wind of 14 m/s. Despite the lack of data concerning the exact model forcing, the modeled results are in good agreement with the observations, and the ABL model satisfactorily reproduces the effects of stability on the resulting velocity profiles.

5.2.3.2   Case A: 3 consecutive days of data

In this section the diurnal cycle simulated above is used to simulate the flow across the Benakanahalli hill. The idea of running a precursor simulation is to reconstruct the upstream conditions, so that the modeled flow field agrees with the observations at the upstream mast M0.

However, during the observational period the upstream conditions are not ideal: for the 135 ° direction both the measurements and simulations at M0 indicate a significant influence of the terrain upstream (the terrain is sloping and there is a small hill and a lake located 4 km and 6 km upstream). This limits the comparability of the results as the inflow conditions at M0 are not homogeneous and it is difficult to match the modeled an observed results at the upstream mast M0. Instead of comparing results over the whole diurnal cycle, the analysis is limited to selected cases during the day for which modeled and observed upstream conditions at M0 compare sufficiently well. Two cases are selected that show similar upstream conditions at M0 for wind speed and wind direction at 75 m and stratification at 10 m (the bulk Richardson number is used

as a measure for stability): 1:00 at night, corresponding to stable conditions
and 12:00 at noon, corresponding to unstable conditions (see Figure 5.8). Both
cases are sufficiently far away from morning and evening transitions where the
ABL flow is highly transient and shows large variations within a rather short
time, which would further complicate the comparability of modeled and ob-
served results. Figure 5.10 illustrates the results obtained for the selected cases
at the masts M0, M1 and M3. Differences between the ASL model and the
ABL model are compared against measurements. Simulation results and mea-
surements are available in 10 min intervals, and all data shown in figure 5.10 are
averages over five such intervals (resulting in 50 min averages) plotted together
with the corresponding standard deviations. Velocity profiles are shown on the
left and the turning of the wind with height is shown on the right. The very dif-
ferent velocity fields during stable and unstable conditions are induced by the
combined effects of Coriolis and stability over complex terrain. These effects
cause the differences between the ASL and the ABL model. This shows that
the atmosphere cannot be treated as neutral and that including these effects in
the ABL model significantly improves the predicted velocity field. The result
are qualitative comparisons of the ABL flow patterns of modeled an observed
results. The available data for the selected 3 day period did not allow a mean-
ingful quantitative comparison since the wind at mast M0 is influenced by the
upstream terrain, so no "undisturbed" upstream conditions are available where
the airflow is in equilibrium.

5.2.3.3   Case B: 3 months of data

The previous case considered data from only three consecutive days. This only
allowed for a qualitative comparison. The general behavior of the wind profiles
and the wind direction for stable and unstable conditions is captured correctly by
the model. A different approach is now used in a second case: all measurement
data is considered (except for wind speeds smaller than 2 m/s), and the resulting
10 min averages are binned according to wind direction (30 degree bins), wind
speed (2 m/s bins) and Froude number (classification based on Froude number
range shown in figure 5.7). Then simulations of diurnal cycles are performed for
different wind directions (one for each wind direction bin every 30 degree) and
for different geostrophic winds (10,12,14,16 and 18 m/s). This equals a total of
70 diurnal cycles. During the simulations the flow properties are sampled every
30 s at all mast positions. The model results are then binned in the same way
as the measurements: the 30 s samples are transformed into 10 min averages
and then binned according to wind direction, wind speed and Froude number.
The result of this approach are two datasets of measured and simulated data
that are stored separately in three-dimensional matrices.
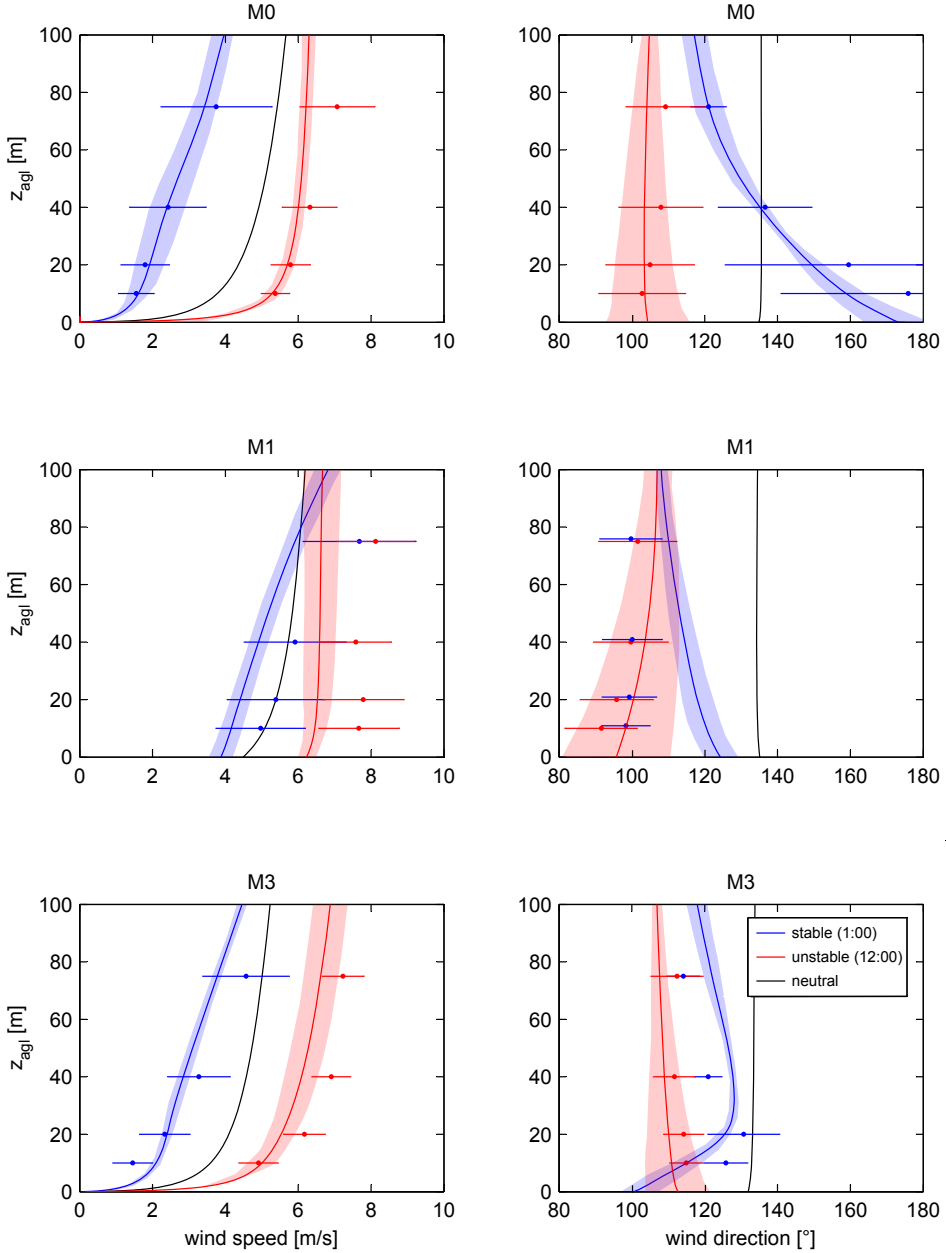
Figure 5.10: Velocity profiles (left) and wind directions (right) for masts M0, M1 and M3. Results from the ASL model (black) and the ABL model compared against measurements (blue: stable conditions at 1:00; red: unstable conditions at 12:00). All data points are 40 min averages, and the error bars and shaded error regions show the corresponding standard deviation.

Since the observational period was only 3 months and wind speeds were very low (less than 4 m/s, see figure 5.7) the resulting dataset was far from ideal. Additionally, the predominant wind direction was from the west (around the 250 degree direction), while the measurement campaign was designed for easterly winds, with the masts located on a 75 degree transect. When binning the dataset into 30 degree bins, the standard deviations get large due to the small number of samples. Therefore wind direction bins 4 to 6 are averaged together. For these bins the measured wind profiles show a similar behavior, and the inflow conditions are close to homogeneous. A total of 1680 10 min samples are available.

Wind speed profiles for different stability classes are shown in figure 5.11 for masts M0, M1 and M3. The masts M1a and M2 are omitted, since the wind in the wake of the hill has shown to be very sensitive to the incoming wind direction. The numerical and observational wind profiles are non-dimensionalized with the top sensor (75 m) of each mast, and all data is based on 10 min averages. Also shown are the standard deviations of the measurements. Generally, the behavior of the wind profiles for the different stability classes is captured correctly by the model, and results lie within the standard deviations. Note that for mast M1 the neutral (green) and unstable (red) model results are on top of each other. Also note that strongly stable and unstable conditions do not occur during the model runs, and are only observed in the measurements for very low wind speeds.

In figure 5.12 the behavior of different flow parameters is shown as a function of stability. Numerical and observational results for wind bins 4 to 6 are considered. The top plots show the observed wind climate for the given sector: wind direction and wind speed distributions are shown together with the distribution of the 7 different stability classes. The wind shear is determined from the 20 m and 75 m sensors of each individual mast, and the turbulence intensity and the tilt angle are determined at the 75 m sensor. The behavior of the wind shear, shown in the second line, is captured correctly by the model, however, it tends to be slightly overpredicted. The turbulence intensity in the third line tends to be underpredicted by the ABL model. For stable conditions the modeled turbulence levels are too low, and the ABL is less mixed, resulting in stronger shear. During the long nighttime regime, stable temperature gradients continue to suppress turbulence in the model. Over flat terrain, this behavior agrees with measurements (see GABLS2 test case 4.4). For flow over terrain, however, it seems that the additional turbulence that in generated by terrain is underestimated by the model. The bottom line in figure 5.12 shows the tilt angle as function of stability. For the upstream mast M0 the tilt angle is zero on average, which reflects the horizontal homogeneity of the incoming flow. On the hill top, as shown in the middle plot for mast M1, the tilt angle generally shows high values for unstable cases and decreasing values for stable cases. This reflects that during unstable conditions the flow is well mixed, and turbulence

effectively communicates topography changes up to higher heights and the flow is deflected upwards by the hill. During stable conditions, the flow is decoupled from the ground due to low turbulence. Therefore topography changes are 'felt' less by the flow at higher heights compared to unstable cases. Downstream of the hill at mast M3 the wind has returned to close to homogeneous conditions again, and shows close to zero tilt angle, similar to the upstream mast M0.

5.3   Summary and Discussion

In this section the ABL model is used to compute flow over complex geometries using curvilinear grids. Two test cases are considered, and generally the ABL model shows significant improvement in predicting the airflow during non-neutral conditions compared the a purely neutral ASL model. The first test case of a steep hill in the wind-tunnel is, however, no ideal test case, since the flow is not at full scale. The resulting wake region in the lee of the hill is overpredicted when compared against the measurements, but agrees well with LES results.

The second test case uses the dataset of the Benakanahalli field experiment. Within a first approach, three consecutive days of data are selected, that show a pronounced diurnal cycle. The ABL model is used to simulate this cycle, and numerical tests show that the results are sensitive to the pressure forcing that drives the flow. Adjusting the geostrophic wind to better match the measurements is certainly possible, but is not the aim of the present work. Instead, stable and unstable conditions are selected where modeled and observed inflow conditions (wind speed and wind direction) at the upstream mast M0 agree. For these cases both velocity profiles and the turning of the wind with height at the masts M1 and M3 are generally predicted well. An optimization of the applied pressure gradient to better match the real conditions can improve the results. However, information on a larger scale is needed to determine how the geostrophic wind behaved during an observational period.

In summary the results show that the implemented modifications are applicable and significantly improve the simulated results compared to purely neutral simulations. Despite the lack of information about boundary and initial conditions and simplifications concerning the model forcing, the ABL model captures effects that are missing in the ASL model.
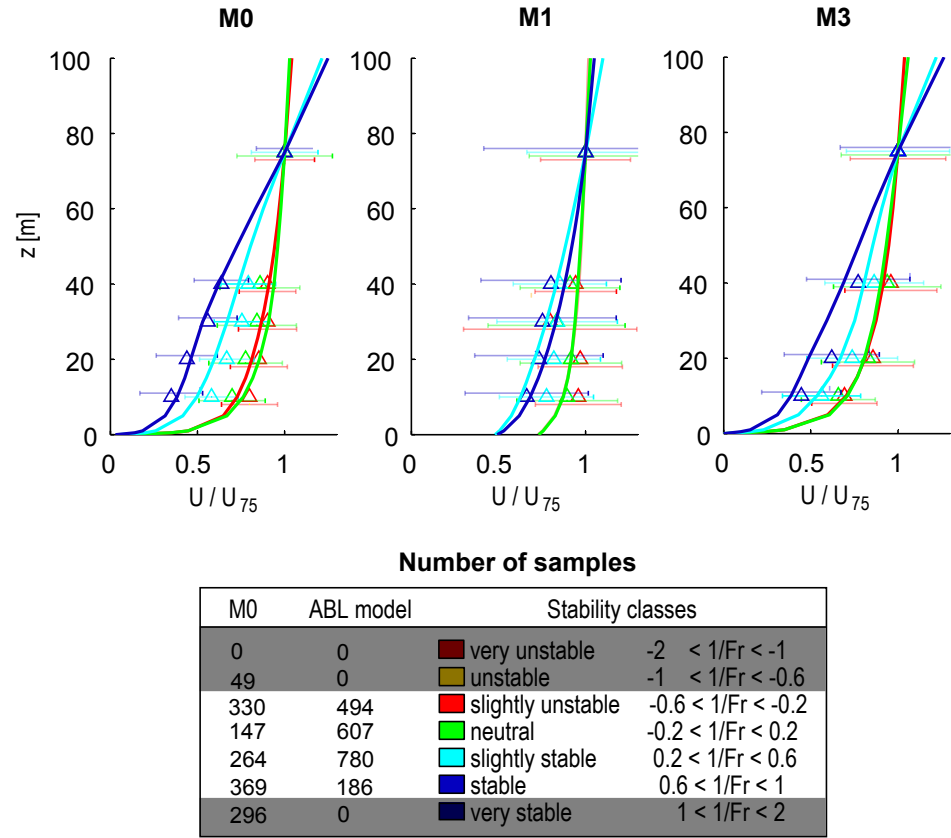
Figure 5.11: Non-dimensional averaged velocity profiles for masts M0, M1 and M3. Results from the ABL model (solid lines) are compared against measurements (triangles with error bars showing the standard deviation). Colors denote different stability classes.
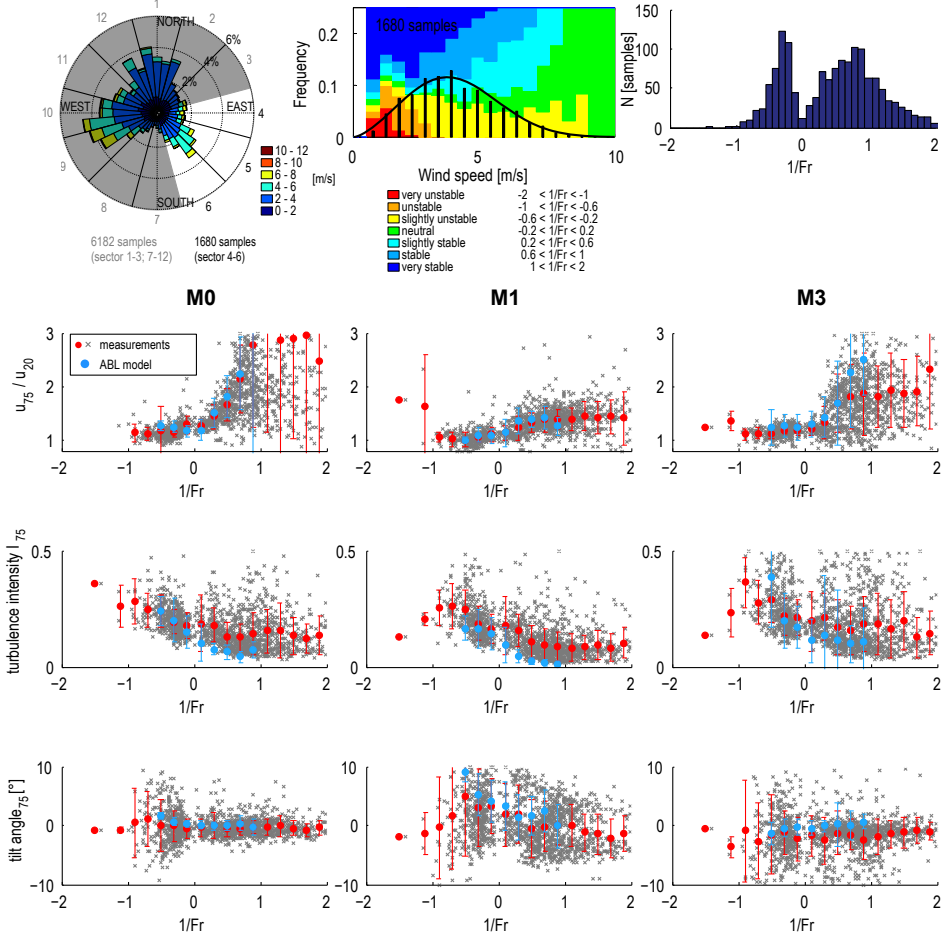
Figure 5.12: 1st line: measured wind statistics for 75 m sensor at M0 (wind speed, and wind direction distribution with Weibull fit, and distribution of Froude number classes); 2nd line: wind shear for masts M0, M1 and M3; 3rd line: turbulence intensity for masts M0, M1 and M3; 4th line: tilt angle for masts M0, M1 and M3.

CHAPTER 6

Conclusions

The present study presents an ABL model that aims at describing the non-neutral wind flow within the whole ABL over complex terrain. The model is successfully validated using several test cases.

For neutral ABL flow, two test cases over flat terrain are considered, and the implemented Coriolis effect and the length-scale limited k-ϵ turbulence model prove applicable. Computed profiles for the velocity components agree well with measurements from the Leipzig and the Cabauw test case. For non-neutral ABL flow over flat terrain diurnal cycles are simulated, where a time varying surface temperature reflects different stability conditions that typically occur within the ABL throughout one day. The implementation of the modified k-ϵ model and of the potential temperature equation prove applicable and the ABL model that now accounts for Coriolis and stability effects generally performed well.

To simulate non-neutral ABL flow over complex terrain, a method using unsteady inlet boundary conditions is developed. To determine the inlet profiles for wind speed, temperature and the turbulent quantities a precursor simulation is run. The resulting vertical profiles are then used as inlet conditions on the lateral boundaries of the terrain domain. Two test cases are considered to assess the model for flows over terrain. First, a wind-tunnel test case is used to validate the ABL model for stably stratified flow over a steep hill. Although this test case is of limited value to validate the ABL model, the applicability of

the model for flows over terrain using curvilinear grids was shown. Finally, the dataset from the Benakanahalli field experiment is used to validate the model for non-neutral flows over complex terrain at full scale. Due to very low wind speeds and an unfavorable predominant wind direction during the observational period, the available dataset was, however, not ideal. Numerical results are compared against the dataset for different stability classes, and the model generally captures the non-neutral behavior of the flow satisfactorily.

The advantage of the presented RANS model framework is its general applicability. All implementations in the ABL model are tuning free, and except for general site specific simulation parameters, no additional model coefficients need to be specified before the simulation. The developed ABL model significantly improves predictions when compared to the neutral ASL model. In summary the results show that the implemented modifications are applicable and reproduce the main flow characteristics for neutral and non-neutral flow over flat and complex terrain.

CHAPTER 7

Future work

Although the approach presented in the present work to model non-neutral ABL flows has shown significant improvements over neutral ABL models, several issues require further investigation. For flow over complex terrain, the modeled turbulent kinetic energy levels have shown to be underestimated. This is especially evident during stable cases, where modeled turbulence is basically eradicated completely, which is not supported by the observations from the Benakanahalli hill. Another validation study over complex terrain, that is not included in the present report, has shown the same issue. Furthermore it became evident that for extremely complex sites with large height differences within the area of interest (> 500 m), numerical instabilities can occur, that are connected to the coupling of the buoyancy forces with the momentum equations. Therefore the implementation of the force allocation model, that usually avoids this issue, needs further investigation.

The implemented turbulence model from Sogachev et al. (2012) is based on simplifications and represents a compromise between accuracy and computational cost. Most of the validation cases have been carried out over homogeneous flat terrain, therefore more extensive tests are necessary to confirm that the formulations and model coefficients are appropriate for modeling non-neutral ABL flows over complex terrain. Another issue, as pointed out by Sogachev et al. (2012), is that the current formulation of the buoyancy related terms is based on the global Mellor-Yamada length scale formulation. A formulation using local

similarity instead could be beneficial, but was omitted due to numerical issues.

Research on two-equation modeling for non-neutral ABL flows is ongoing, and new models or variants of existing models can be expected in the future. Especially the relationships for buoyancy and canopy related terms, are expected to receive special attention. Also other physical processes could be included into the presented microscale modeling approach. The present study is based on the dry air assumption, while observations have shown that humidity impacts ABL flows (Geernaert and Larsen, 1993; Sempreviva and Højstrup, 1998; Barthelmie et al., 2010). Humidity has been shown to have a significant impact on the atmospheric stability, and Cañadillas et al. (2007) show that the contribution from humidity on the virtual potential temperature can be as high as 25 %. Humidity can be included in the model via an additional equation for water vapour (Arya, 2001). Additionally, the atmosphere could be coupled to the underlying soil as described in Steeneveld et al. (2006), instead of prescribing humidity and temperature at the surface. Another important feature of the surface that could be included in the model are vegetation effects, and development of canopy models is ongoing (Sogachev et al., 2012).

Including new processes into existing ABL models requires a thorough model validation. Recent works, including the present study, have shown that validation of non-neutral ABL models represents a big challenge, and that experimental ABL data for different stability conditions is lacking (Meissner et al., 2009; Sogachev et al., 2012). During measurement campaigns, temperature data is often not sufficient to classify stability satisfactorily, or not available at all. Furthermore, measurements are usually only available close to the ground ($<$ 80 m), which raises the issue of initial and boundary conditions of numerical experiments, because they are not fully determined from the available data. More experimental datasets at full scale that focus on non-neutral flow are therefore necessary and crucial to better understand the physical processes and to further develop and validate ABL models. However, perfect test cases do not occur in reality and large scale atmospheric variations influence measured statistics. The lack of information about these parameters complicates the comparability of numerical and observational data.

Initial and boundary conditions for the present model could be improved based on model results from mesoscale simulations. Mesoscale simulations are able to provide information on large scales and resolve large scale features like frontal passages, sea breezes, mountain waves, large scale pressure systems, large scale subsidence inversions (gradually sinking air over a wide area) or large convective systems (Lundquist et al., 2010). Especially for non-neutral ABL flows, mesoscale meteorological models can provide information about the local stability distribution at a relatively high resolution, when local temperature measurements are not sufficient or not available (Meissner et al., 2009). Including

the effects of both mesoscale and microscale processes can improve ABL models, and several methods can be used to combine them.

The most direct approach is to use mesoscale models to provide more realistic initial and boundary conditions for microscale models, and a number of studies show significant improvements (Frank and Landberg, 1997; Castro et al., 2008; Baik et al., 2009; Tewari et al., 2010; Ely et al., 2012; Wang et al., 2013). Additionally, meso- and microscale models can be combined using nesting, where microscale models are implemented within mesoscale models (Lundquist et al., 2010). Another method is nudging, where variables within the domain of microscale models are forced towards observed or modeled large scale values (Yamada and Koike, 2011). All the above approaches combine meso- and microscale models, but processes at different scales are still modeled separately. Alternatively mesoscale models can be scaled down and applied with high horizontal resolution (Yamada, 2004; Yamada and Koike, 2011) and microscale models can be scaled up in order to resolve large scale features (Mochida et al., 2011). Additionally, hybrid methods have been developed using a combination of above approaches (Li et al., 2010). One major challenge of all the above approaches is to obtain consistency between the different models that use different parametrizations and different computational grids.

Another possible application of the developed ABL model is to study wind turbine wakes and loads on turbines in non-neutral atmospheric conditions. The importance of stratification on wake flows is still not sufficiently understood, and more detailed investigations can help to predict power losses and loads on turbines more accurately. A number of experimental studies report significant impacts of atmospheric stability on measured wakes, especially for offshore wind farms (Türk and Emeis, 2010; Hansen et al., 2012; Wharton et al., 2012; Schepers et al., 2012). Generally stable conditions lead to a larger power deficit and wake recovery tends to be slower. The influence of atmospheric stability on wakes and loads on turbines has also been studied numerically (Lange and Waldl, 2002; Sathe and Bierbooms, 2007; Barthelmie et al., 2009; Rados et al., 2009; Churchfield et al., 2012; Westerhellweg et al., 2013; Keck et al., 2013) and models that have been extended to include atmospheric stability tend to predict power losses and loads on turbines more accurately.

Finally, LES could be used to model the non-neutral ABL in order to get a more accurate solution of the turbulent flow field. A new method on how to provide non-neutral transient boundary conditions for LES simulations would have to be developed. Also the subgrid-scale turbulence model would need additional modification to account for buoyancy effects.

Appendix

8.1   Test case: 2D lid-driven square cavity

The simple geometry shown in figure 8.1 provides an appealing setting to study the combined forced and natural convection (mixed convection). The forced convection is induced by a shear force from the motion of the upper lid, whereas natural convection is induced by the differentially heated horizontal walls. Except for the lid, all walls are stationary (no-slip tangential and zero normal velocity boundary condition) and the vertical walls are adiabatic. Three cases are considered: 1) horizontal walls at same temperature (neutral case a) 2) top wall heated, bottom wall cooled (gravitationally stable case b) 3) top wall cooled, bottom wall heated (gravitationally unstable case c). The transient, laminar, 2D numerical simulations are performed for the following non-dimensional governing parameters: Reynolds number: $316 < Re < 5000$, Prandtl number $Pr = 0.71$ representative of air, Richardson number $0.1 < Ri < 10$. A mesh resolution of 128x128 was found to be sufficient for the present problem, and a convergence criterion of $\left|\phi^k - \phi^{k-1}\right| < 10^{-5}$ is used. Hence, iterations are terminated when the maximum between two successive iterations is smaller than 10^{-5}.
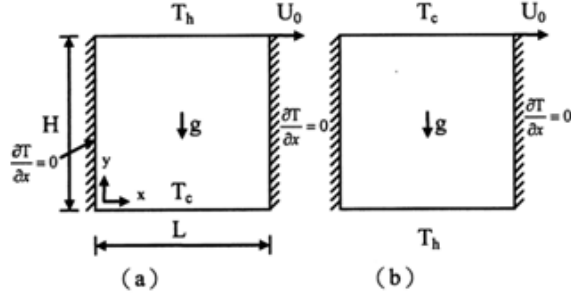
Figure 8.1: Physical domain and boundary conditions for cases (a) stable and (b) unstable. Figure taken from Cheng and Liu (2010).

8.1.1 Results

The streamlines and isothermal lines of the conducted simulations are visualized and the mid-plane velocity profiles are qualitatively compared against the results from (Babu and Korpela, 1993; Iwatsu and Hyun, 1995; Ghia et al., 1982) in figure 8.2. For reasons of brevity only $Re = 1000$ is presented. As the EllipSys solver employs the primitive variable formulation (velocity and pressure) to describe the flow, the stream function was generated from the axial velocity components by integrating over the physical domain in order to compare the results with earlier studies that used the vorticity-stream function formulation

$$u = \frac{\partial \Psi}{\partial y}, v = -\frac{\partial \Psi}{\partial x} \ , \tag{8.1}$$

$$\Omega = \frac{\partial v}{\partial x} - \frac{\partial u}{\partial y} \ . \tag{8.2}$$

The top left plot in figure 8.2 shows the steady state streamlines of case (a). The driven-lid generates a primary vortex that dominates the entire cavity, with small secondary eddies in the lower corners. Table 8.1 presents the quantitative comparison of the primary vortex for the neutral case. For case (b), shown in the second column of figure 8.2, the stable temperature gradient limits the main motion of the fluid to the upper region, resulting in an almost stagnant bottom region with vertically-linear isotherms (middle plot). The unstable case (c) promotes natural convection in the lower half of the cavity while the upper part is dominated by forced convection. The interaction of both results in the formation of two counter-recirculating eddies having a large temperature gradient between them. Qualitative comparisons of the flow patterns with earlier studies show good agreement, while quantitative comparison shows better than 96 % agreement for the strength and position of the primary vortex of case (a).

Table 8.1: Comparison of primary vortex to benchmark simulations (neutral case): stream function, Ψ, vorticity, Ω, location, x, y and error, $\Delta[\%]$. ABL denotes the current model.

Re	Ref.	Grid	Ψ	Δ	Ω	Δ	x	Δ	y	Δ
1000	(Erturk and Gokcol, 2004)	601x601	0.1190	1.70	2.0678	0.23	0.5300	0.48	0.5650	0.29
	(Ghia et al., 1982)	128x128	0.1180	0.86	2.0497	0.65	0.5313	0.72	0.5625	0.74
	(Zhang, 2000)	128x128	0.1188	1.59	2.0668	0.18	0.5313	0.72	0.5625	0.74
	(Botella and Peyret, 1998)	128x128	0.1189	1.70	2.0678	0.23	0.5308	0.63	0.5652	0.26
	(Bruneau and Saad, 2005)	128x128	0.1179	0.80	2.0508	0.60	0.5314	0.72	0.5625	0.74
	(Bruneau and Saad, 2005)	1024x1024	0.1190	1.69	2.0674	0.21	0.5314	0.72	0.5654	0.22
	(Cheng and Liu, 2010)	128x128	0.1169	0.03	2.0648	0.08	0.5314	0.72	0.5625	0.74
	ABL	128x128	0.1169		2.0630		0.5275		0.5667	
3200	(Ghia et al., 1982)	128x128	0.1204	2.03	1.9886	3.30	0.5165	0.60	0.5469	0.69
	(Zhang, 2000)	128x128	0.1202	1.86	1.9489	1.33	0.51563	0.77	0.53906	0.76
	(Cheng and Liu, 2010)	128x128	0.1198	1.60	1.9480	1.28	0.51563	0.77	0.53906	0.76
	ABL	128x128	0.1180		1.9230		0.51961		0.54314	
5000	(Erturk and Gokcol, 2004)	601x601	0.1222	3.99	1.9405	2.81	0.5150	0.63	0.5350	0.05
	(Ghia et al., 1982)	256x256	0.1190	1.37	1.8602	1.39	0.5117	0.01	0.5352	0.02
	(Zhang, 2000)	128x128	0.1181	0.66	1.9062	1.06	0.5156	0.75	0.5391	0.70
	(Bruneau and Saad, 2005)	256x256	0.1206	2.74	1.9125	1.38	0.5156	0.75	0.5352	0.02
	(Bruneau and Saad, 2005)	2048x2048	0.1220	3.80	1.9327	2.41	0.5147	0.56	0.5352	0.02
	(Cheng and Liu, 2010)	128x128	0.1182	0.75	1.9090	1.20	0.5156	0.75	0.5391	0.70
	ABL	128x128	0.1173		1.8861		0.5118		0.5353	

This positive agreement shows that the solver is adequate to solve the mixed convection problem like the one presented. Simulating this coupled convective heat transfer problem shows that the governing equations including temperature are solved correctly within a two-dimensional domain.
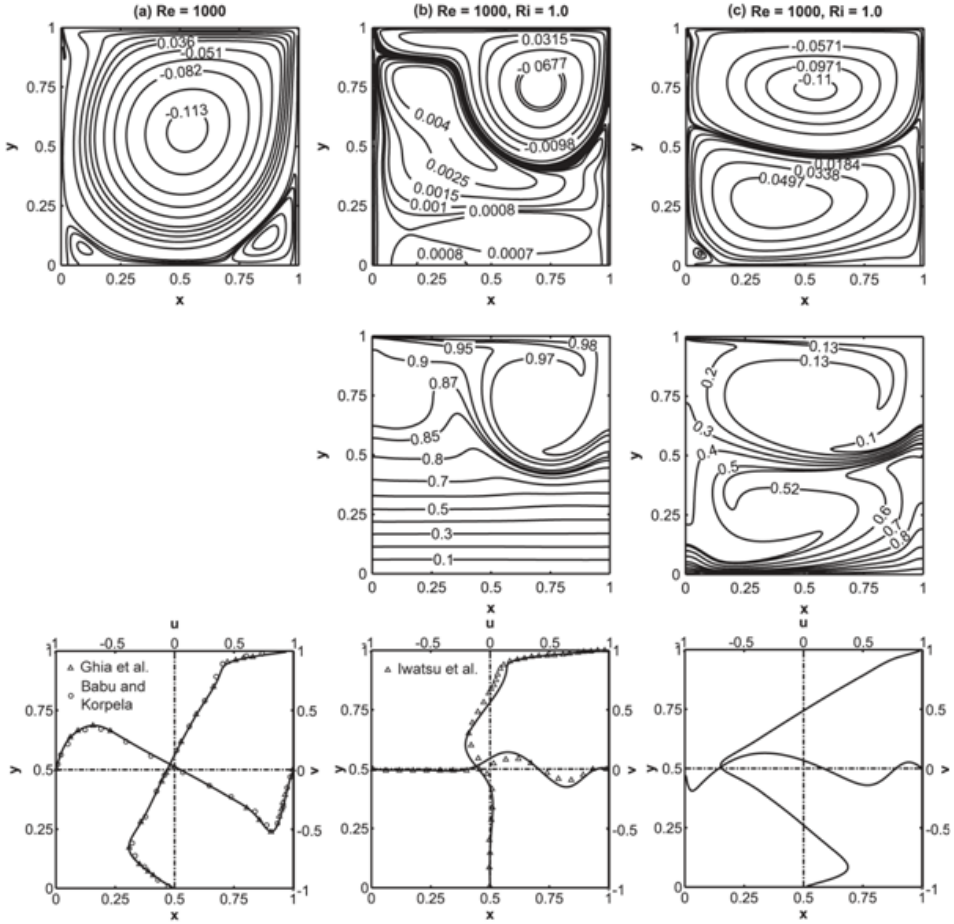
Figure 8.2: Top: visualization of streamlines. Middle: isothermal lines. Bottom: mid-plane velocity profiles. Lines denote model results, and symbols are numerical results from Babu and Korpela (1993); Iwatsu and Hyun (1995) and Ghia et al. (1982), for cases (a) neutral, (b) stable and (c) unstable.

Bibliography

Alinot, C. and Masson, C. (2005). k–ϵ model for the atmospheric boundary layer under various thermal stratifications. *J Sol Energ-T ASME*, 127(4):438–443.

ANSYS (2010). *ANSYS CFX-Pre User's Guide Release 13*. ANSYS.

ANSYS (2011). *ANSYS FLUENT User's Guide Release 14*. ANSYS.

Anthes, R. A., Kuo, Y.-H., Benjamin, S. G., and Li, Y.-F. (1982). The evolution of the mesoscale environment of severe local storms: Preliminary modeling results. *Mon Weather Rev*, 110(9):1187–1213.

Apsley, D. D. and Castro, I. P. (1997). A limited-length-scale κ–ϵ model for the neutral and stably-stratified atmospheric boundary layer. *Boundary-Layer Meteorol*, 83(1):75–98.

Arya, P. S. (2001). *Introduction to Micrometeorology*. Academic Press.

Ayotte, K. W., Finnigan, J. J., and Raupach, M. R. (1999). A second-order closure for neutrally stratified vegetative canopy flows. *Boundary-Layer Meteorol*, 90(2):189–216.

Babu, V. and Korpela, S. A. (1993). On the direct solution of poisson's equation on a non-uniform grid. *J Comput Phys*, 104(1):93–98.

Badger, J., Barthelmie, R., Frandsen, S., and Christiansen, M. (2006). Mesoscale modelling for an offshore wind farm. In *Proceedings: European Wind Energy Association, Brussels, 2006*.

Baik, J.-J., Park, S.-B., and Kim, J.-J. (2009). Urban flow and dispersion simulation using a CFD model coupled to a mesoscale model. *J Appl Meteorol*, 48(8):1667–1681.

Barthelmie, R., Frandsen, S., Hansen, K., Schepers, J., Rados, K., Schlez, W., Neubert, A., Jensen, L., and Neckelmann, S. (2009). Modelling the impact of wakes on power output at nysted and horns rev. In *Proceedings: EWEC 2009 - European Wind Energy Conference & Exhibition, Marseille, France.*

Barthelmie, R. J., Sempreviva, A. M., and Pryor, S. C. (2010). The influence of humidity fluxes on offshore wind speed profiles. *Ann Geophys*, 28(5):1043–1052.

Basu, S. and Porté-Agel, F. (2006). Large-eddy simulation of stably stratified atmospheric boundary layer turbulence: A scale-dependent dynamic modeling approach. *J Atmos Sci*, 63(8):2074–2091.

Beaucage, P., Brower, M. C., and Tensen, J. (2012). Evaluation of four numerical wind flow models for wind resource mapping. *Wind Energy*.

Bechmann, A. (2006). Large-eddy simulation of atmospheric flow over complex terrain. Risø-phd-28(en), Risø National Lab., Roskilde, Denmark.

Bechmann, A., Sørensen, N. N., Berg, J., Mann, J., and Réthoré, P.-E. (2011). The bolund experiment, part ii: Blind comparison of microscale flow models. *Boundary-Layer Meteorol*, 141:245–271.

Beljaars, A. C. M., Walmsley, J. L., and Taylor, P. A. (1987). A mixed spectral finite-difference model for neutrally stratified boundary-layer flow over roughness changes and topography. *Boundary-Layer Meteorol*, 38(3):273–303.

Berg, J., Bechmann, A., Courtney, M., Koblitz, T., Hristov, Y. V., Berg, J., Bechmann, A., Courtney, M., Koblitz, T., and Hristov, Y. V. (2012). In the wake of bolund: Benakanahalli - stratification and complex terrain. In *Proceedings: EWEA 2012 - European Wind Energy Conference & Exhibition, Copenhagen, Denmark.*

Berg, J., Mann, J., Bechmann, A., and Courtney, M. S. (2010). The bolund experiment, part i: Flow over a steep, three-dimensional hill. *Boundary-Layer Meteorol*, 141:219–243.

Berge, E., Gravdahl, A. R., Schelling, J., Tallhaug, L., and Undheim, O. (2006). Wind in complex terrain. a comparison of wasp and two cfd-models. In *Proceedings: EWEC 2006 - European Wind Energy Conference & Exhibition, Athens, Greece.*

Bergström, H. (2001). Boundary-layer modelling for wind climate estimates. *Wind Engineering*, 25(5):289–299.

Blackadar, A. K. (1962). The vertical distribution of wind and turbulent exchange in a neutral atmosphere. *J Geophys Res*, 67(8):3095–3102.

Blocken, B., Carmeliet, J., and Stathopoulos, T. (2007). CFD evaluation of wind speed conditions in passages between parallel buildings-effect of wall-function roughness modifications for the atmospheric boundary layer flow. *J Wind Eng Ind Aerod*, 95(9-11):941–962.

Blocken, B., Janssen, W., and van Hooff, T. (2012). CFD simulation for pedestrian wind comfort and wind safety in urban areas: General decision framework and case study for the eindhoven university campus. *Environ Modell Softw*, 30:15–34.

Botella, O. and Peyret, R. (1998). Benchmark spectral results on the lid-driven cavity flow. *Computers & Fluids*, 27(4):421–433.

Brost, R. A. and Wyngaard, J. C. (1978). A model study of the stably stratified planetary boundary layer. *J Atmos Sci*, 35(8):1427–1440.

Bruneau, C.-H. and Saad, M. (2005). The 2D lid-driven cavity problem revisited. *Computers & Fluids*, 35(3):326–348.

Businger, J. A., Wyngaard, J. C., Izumi, Y., and Bradley, E. F. (1971). Flux-profile relationships in the atmospheric surface layer. *J Atmos Sci*, 28(2):181–189.

Cañadillas, B., Foreman, R., Kinder1, F., Emeis, S., and Neumann, T. (2007). First eddy-covariance measurements at fino1 the influence of humidity fluxes on atmospheric stability. In *Proceedings: The Science of Making Torque from Wind, Lyngby, Denmark*.

Castro, F. A., Palma, J. M. L. M., and Lopes, A. S. (2003). Simulation of the askervein flow. part 1: Reynolds averaged Navier–Stokes equations (k–ϵ turbulence model). *Boundary-Layer Meteorol*, 107(3):501–530.

Castro, F. A., Santos, C. M. P. S., and Palma, J. M. L. M. (2008). Parallelisation of the CFD code of a CFD-NWP coupled system for the simulation of atmospheric flows over complex terrain. In *High Performance Computing for Computational Science - VECPAR 2008*, number 5336 in Lecture Notes in Computer Science, pages 27–38. Springer Berlin Heidelberg.

CD-adapco (2006). *CCM User Guide STAR-CD Version 4.02*. CD-adapco.

Cheng, T. S. and Liu, W.-H. (2010). Effect of temperature gradient orientation on the characteristics of mixed convection flow in a lid-driven square cavity. *Computers & Fluids*, 39(6):965–978.

Churchfield, M. J., Lee, S., Michalakes, J., and Moriarty, P. J. (2012). A numerical study of the effects of atmospheric and wake turbulence on wind turbine dynamics. *J Turb*, page 14.

Clarenc, T., Girard, N., Delaunay, D., and Chantelot, A. (2007). Wind farm production assessment in complex terrain new validations of meteodyn wt. In *Proceedings: EWEC 2006 - European Wind Energy Conference & Exhibition, Milan, Italy.*

Clarke, R. H. (1971). *The Wangara experiment : boundary layer data.* Melbourne : C.S.I.R.O. Limited distribution.

Detering, H. W. and Etling, D. (1985). Application of the e-ϵ turbulence model to the atmospheric boundary layer. *Boundary-Layer Meteorol*, 33:113–133.

Duynkerke, P. G. (1988). Application of the k–ϵ turbulence closure model to the neutral and stable atmospheric boundary layer. *J Atmos Sci*, 45(5):865–880.

Dyer, A. J. (1974). A review of flux-profile relationships. *Boundary-Layer Meteorol*, 7(3):363–372.

Ely, A., Stuart, P., Zhu, M., Palma, J., Rodrigues, C., and Chertovskih, R. (2012). Mesoscale and cfd coupling: An improved technique for predicting microscale wind. In *Proceedings: EWEA 2012 - European Wind Energy Conference & Exhibition, Copenhagen, Denmark.*

Erturk, E. and Gokcol, C. (2004). Fourth order compact formulation of navier-stokes equations and driven cavity flow at high reynolds numbers. *Int J Numer Meth Fl*, 50:421–436.

Finnigan, J. (2007). Turbulent flow in canopies on complex topography and the effects of stable stratification. In Gayev, Y. A. and Hunt, J. C. R., editors, *Flow and Transport Processes with Complex Obstructions*, number 236 in NATO Science Series, pages 199–219. Springer Netherlands.

Frank, H. P. and Landberg, L. (1997). Modelling the wind climate of ireland. *Boundary-Layer Meteorol*, 85(3):359–377.

Franke, J., Hellsten, A., Schlunzen, K. H., and Carissimo, B. (2011). The COST 732 best practice guideline for CFD simulation of flows in the urban environment: a summary. *Int J of Environment and Pollution*, 44(1/2/3/4):419.

Freedman, F. R. and Jacobson, M. Z. (2003). Modification of the standard ϵ-equation for the stable abl through enforced consistency with Monin–Obukhov similarity theory. *Boundary-Layer Meteorol*, 106(3):383–410.

Geernaert, G. and Larsen, S. (1993). On the role of humidity in estimating marine surface layer stratification and scatterometer cross section. *J Geohys Res*, 98(C1):927–932.

Ghia, U., Ghia, K., and Shin, C. (1982). High-re solutions for incompressible flow using the navier-stokes equations and a multigrid method. *J Comput Phys*, 48(3):387–411.

Gravdahl, A. R. and Harstveit, K. (2000). Windsim - flow simulations in complex terrain. In *5th German Wind Energy Conference, Wilhelmshaven, Germany.*

Hanjalic, K. and Launder, B. E. (1972). A reynolds stress model of turbulence and its application to thin shear flows. *J Fluid Mech*, 52(04):609–638.

Hanna, S. R., Brown, M. J., Camelli, F. E., Chan, S. T., Coirier, W. J., Kim, S., Hansen, O. R., Huber, A. H., and Reynolds, R. M. (2006). Detailed simulations of atmospheric flow and dispersion in downtown manhattan: An application of five computational fluid dynamics models. *B Am Meteorol Soc*, 87(12):1713–1726.

Hansen, K. S., Barthelmie, R. J., Jensen, L. E., and Sommer, A. (2012). The impact of turbulence intensity and atmospheric stability on power deficits due to wind turbine wakes at horns rev wind farm. *Wind Energy*, 15(1):183–196.

Hargreaves, D. and Wright, N. (2007). On the use of the k-ϵ model in commercial CFD software to model the neutral atmospheric boundary layer. *J Wind Eng Ind Aerod*, 95(5):355–369.

Högström, U. (1996). Review of some basic characteristics of the atmospheric surface layer. *Boundary-Layer Meteorol*, 78(3-4):215–246.

Huser, A. and Jahre, P. (1997). Application of k–ϵ model to the stable ABL: pollution in complex terrain. *J Wind Eng Ind Aerod*, 68:425–436.

Iwatsu, R. and Hyun, J. M. (1995). Three-dimensional driven-cavity flows with a vertical temperature gradient. *Int J Heat Mass Transfer*, 38(18):3319–3328.

Jackson, P. S. and Hunt, J. C. R. (1975). Turbulent wind flow over a low hill. *Quart J Roy Meteor*, 101(430):929–955.

Jacobson, M. Z. (2005). *Fundamentals of Atmospheric Modeling.* Cambridge University Press, 2 edition.

Katul, G. G., Mahrt, L., Poggi, D., and Sanz, C. (2004). One- and Two-Equation models for canopy turbulence. *Boundary-Layer Meteorol*, 113(1):81–109.

Keck, R.-E., de Maré, M., Churchfield, M. J., Lee, S., Larsen, G., and Aagaard Madsen, H. (2013). On atmospheric stability in the dynamic wake meandering model. *Wind Energy.*

Kiranoudis, C., Voros, N., and Maroulis, Z. (2001). Short-cut design of wind farms. *Energy Policy*, 29(7):567–578.

Klipp, C. L. and Mahrt, L. (2004). Flux-gradient relationship, self-correlation and intermittency in the stable boundary layer. *Quart J Roy Meteor*, 130(601):2087–2103.

Koblitz, T., Bechmann, A., Berg, J., Sogachev, A., Sørensen, N., and Réthoré, P.-E. (2012a). Atmospheric stability and complex terrain - comparing measurements and cfd. In *Proceedings: The Science of Making Torque from Wind, Oldenburg, Germany*.

Koblitz, T., Bechmann, A., Sogachev, A., and Sørensen, N. N. (2012b). Atmospheric stability in cfd, representation of the diurnal cycle in the atmospheric boundary layer. In *Proceedings: EWEA 2012 - European Wind Energy Conference & Exhibition, Copenhagen, Denmark*.

Koblitz, T., Bechmann, A., Sogachev, A., and Sørensen, N. N. (2012c). Modification of cfd code to model the atmospheric boundary layer. In *Proceedings: 13th International Conference on Wind Engineering, Amsterdam, Netherlands*.

Koblitz, T., Bechmann, A., and Sørensen, N. (2010). The 2d lid-driven cavity–validation of cfd code to model non-neutral atmospheric boundary layer conditions. In *Proceeding: 6th PhD Seminar on Wind Energy in Europe, Trondheim, Norway*, pages 157–160.

Lange, B. and Waldl, H.-P. (2002). Modelling of offshore wind turbine wakes with the wind farm program FLaP. *Wind Energy*, 6(1):87 – 104.

Launder, B. E., Reece, G. J., and Rodi, W. (1975). Progress in the development of a reynolds-stress turbulence closure. *J Fluid Mech*, 68(03):537.

Launder, B. E. and Spalding, D. B. (1974). The numerical computation of turbulent flows. *Comp Meth Appl Mech Engineer*, 3:269–289.

Lettau, H. (1950). A re-examination of the Leipzig wind profile considering some relations between wind and turbulence in the frictional layer. *Tellus*, 2(2):125–129.

Li, L., Zhang, L.-J., Zhang, N., Hu, F., Jiang, Y., C.-Y-Xuan, and Jiang, W.-M. (2010). Study on the micro-scale simulation of wind field over complex terrain by rams/fluent modeling system. In *Proceedings: 5th Int. Symposium on Computational Wind Engineering, Chapel Hill, USA*.

Li, X., Zimmerman, N., and Princevac, M. (2008). Local imbalance of turbulent kinetic energy in the surface layer. *Boundary-Layer Meteorol*, 129(1):115–136.

Lundquist, J. K., Mirocha, J. D., and Kosovic, B. (2010). Nesting large-eddy simulations within mesoscale simulations for wind energy applications. In *Proceedings: 5th Int. Symposium on Computational Wind Engineering, Chapel Hill, USA*.

Lutgens, F. K. and Tarbuck, E. J. (2013). *The atmosphere: an introduction to meteorology*. Pearson, Boston.

Mason, P. J. and Thomson, D. J. (2007). Large-eddy simulations of the neutral-static-stability planetary boundary layer. *Quart J Roy Meteor*, 113(476):413–443.

Maurizi, A., Palma, J., and Castro, F. (1998). Numerical simulation of the atmospheric flow in a mountainous region of the north of portugal. *J Wind Eng Ind Aerod*, 74–76:219–228.

McNaughton, K. (2009). The rise and fall of monin-obukhov theory. *AsiaFlux Newsletter*, 30:1–4.

Meissner, C., Gravdahl, A. R., and Steensen, B. (2009). Including thermal effects in cfd simulations. In *Proceedings: EWEC 2009 - European Wind Energy Conference& Exhibition, Marseille, France.*

Mellor, G. L. and Yamada, T. (1974). A hierarchy of turbulence closure models for planetary boundary layers. *J Atmos Sci*, 31:1791–1806.

Michelsen, J. A. (1992). Basis3d-a platform for development of multiblock pde solvers. Technical report afm, Technical University of Denmark.

Michelsen, J. A. (1994). Block structured multigrid solution of 2d and 3d elliptic pde solvers. Technical report afm, Technical University of Denmark.

Mochida, A., Iizuka, S., Tominaga, Y., and Lun, I.-F. (2011). Up-scaling cwe models to include mesoscale meteorological influences. *J Wind Eng Ind Aerod*, 99:187–198.

Monin, A. S. and Obukhov, A. M. (1954). Basic laws of turbulent mixing in the surface layer of the atmosphere. *Tr Akad Nauk SSSR Geophys Inst*, 24(151):163–187.

Mortensen, N., Bowen, A., Antoniou, I., Mortensen, N., Bowen, A., and Antoniou, I. (2006). Improving WAsP predictions in (too) complex terrain. In *Proceedings: EWEC 2006 - European Wind Energy Conference & Exhibition, Athens, Greece.*

Mortensen, N., Heathfield, D., Myllerup, L., Landberg, L., and Rathmann, O. (2005). Wind atlas analysis and application program: Wasp 8 help facility (online). Technical report, Technical University of Denmark.

OpenFOAM-Foundation (2013). *OpenFOAM The Open Source CFD Toolbox User Guide Version 2.2.2*. OpenFOAM–Foundation.

Panofsky, H. A. and Dutton, J. A. (1984). *Atmospheric turbulence: models and methods for engineering applications*. Wiley.

Parente, A. and Gorlé, C. (2011). Improved k–ϵ model and wall function formulation for the RANS simulation of ABL flows. *J Wind Eng Ind Aerod*, 99(4):267–278.

Patankar, S. (1980). *Numerical Heat Transfer and Fluid Flow*. Taylor & Francis, 1 edition.

Patankar, S. and Spalding, D. (1972). A calculation procedure for heat, mass and momentum transfer in three-dimensional parabolic flows. *Int J Heat Mass Transfer*, 15(10):1787–1806.

Pielke, R. (2002). *Mesoscale meteorological modeling*. Academic Press, San Diego.

Pieterse, J. and Harms, T. (2013). CFD investigation of the atmospheric boundary layer under different thermal stability conditions. *J Wind Eng Ind Aerod*, 121:82–97.

Pontiggia, M., Derudi, M., Busini, V., and Rota, R. (2009). Hazardous gas dispersion: A CFD model accounting for atmospheric stability classes. *Journal of Hazardous Materials*, 171(1–3):739–747.

Pope, S. B. (2000). *Turbulent flows*. Cambridge University Press, UK, 1 edition.

Probst, O. and Cárdenas, D. (2010). State of the art and trends in wind resource assessment. *Wind Energy*, 3(6):1087–1141.

Rados, K. G., Prospathopoulos, J. M., Stefanatos, N. C., Politis, E. S., Chaviaropoulos, P. K., and Zervos, A. (2009). Cfd modeling issues of wind turbine wakes under stable atmospheric conditions. In *Proceedings: EWEC 2009 - European Wind Energy Conference & Exhibition, Marseille, France*.

Réthoré, P.-E. and Sørensen, N. N. (2012). A discrete force allocation algorithm for modelling wind turbines in computational fluid dynamics: A discrete force allocation algorithm. *Wind Energy*, 15(7):915–926.

Rhie, C. and Chow, W. (1982). A numerical study of the turbulent flow past an isolated airfoil with trailing edge separation. In *3rd Joint Thermophysics, Fluids, Plasma and Heat Transfer Conference*, Fluid Dynamics and Co-located Conferences. American Institute of Aeronautics and Astronautics.

Richards, P. and Hoxey, R. (1993). Appropriate boundary conditions for computational wind engineering models using the k–ϵ turbulence model. *J Wind Eng Ind Aerod*, 46-47:145–153.

Riddle, A., Carruthers, D., Sharpe, A., McHugh, C., and Stocker, J. (2004). Comparisons between FLUENT and ADMS for atmospheric dispersion modelling. *Atmospheric Environment*, 38(7):1029–1038.

Rodi, W. (1987). Examples of calculation methods for flow and mixing in strat-
ified fluids. *J Geophys Res-Oceans*, 92(C5):5305–5328.

Ross, A. N., Arnold, S., Vosper, S. B., Mobbs, S. D., Dixon, N., and Robins,
A. G. (2004). A comparison of wind-tunnel experiments and numerical sim-
ulations of neutral and stratified flow over a hill. *Boundary-Layer Meteorol*,
113(3):427–459.

Sathe, A. and Bierbooms, W. (2007). Influence of different wind profiles due
to varying atmospheric stability on the fatigue life of wind turbines. *J Phys:
Conf Ser*, 75(1):012056.

Schepers, J. G., Obdam, T. S., and Prospathopoulos, J. (2012). Analysis of wake
measurements from the ECN wind turbine test site wieringermeer, EWTW.
Wind Energy, 15(4):575–591.

Schlichting, H. (1968). *Boundary-Layer Theory*. Springer.

Schonfeld, D. (1980). A survey of numerical models for wind prediction. Tda
progress report, DSN Engineering section.

Sempreviva, A. M., Barthelmie, R. J., and Pryor, S. C. (2008). Review of
methodologies for offshore wind resource assessment in european seas. *Surv
Geophys*, 29(6):471–497.

Sempreviva, A. M. and Højstrup, J. (1998). Transport of temperature and
humidity variance and covariance in the marine surface layer. *Boundary-
Layer Meteorol*, 87(2):233–253.

Sogachev, A. (2009). A note on two-equation closure modelling of canopy flow.
Boundary-Layer Meteorol, 130:423–435.

Sogachev, A., Kelly, M., and Leclerc, M. (2012). Consistent two-equation clo-
sure modelling for atmospheric research: Buoyancy and vegetation implemen-
tations. *Boundary-Layer Meteorol*, pages 1–21.

Sogachev, A. and Panferov, O. (2006). Modification of two-equation models to
account for plant drag. *Boundary-Layer Meteorol*, 121:229–266.

Sørensen, N. N. (1995). General purpose flow solver applied to flow over hills.
Technical report risø-r-827(en), Risø National Lab., Roskilde, Denmark.

Sørensen, N. N. (1998). Hypgrid2d a 2-d mesh generator. Technical report,
Technical University of Denmark.

Sørensen, N. N., Bechmann, A., Johansson, J., Myllerup, L., Botha, P., Vinther,
S., and Nielsen, B. S. (2007). Identification of severe wind conditions using a
reynolds-averaged navier-stokes solver. In *Proceedings: The Science of Making
Torque from Wind, Lyngby, Denmark*.

Spalart, P. R. and Rumsey, C. L. (2007). Effective inflow conditions for turbulence models in aerodynamic calculations. *AIAA Journal*, 45(10):2544–2553.

Stathopoulos, T. (2002). The numerical wind tunnel for industrial aerodynamics: Real or virtual in the new millennium? *Wind Struct*, 5:193–208.

Steeneveld, G. J., van de Wiel, B. J. H., and Holtslag, A. A. M. (2006). Modeling the evolution of the atmospheric boundary layer coupled to the land surface for three contrasting nights in CASES-99. *J Atmos Sci*, 63(3):920–935.

Stull, R. B. (1988). *An Introduction to Boundary Layer Meteorology*. Springer, softcover reprint of the original 1st ed. 1988 edition.

Svensson, G., Holtslag, A., Kumar, V., Mauritsen, T., Steeneveld, G., Angevine, W., Bazile, E., Beljaars, A., de Bruijn, E., Cheng, A., Conangla, L., Cuxart, J., Ek, M., Falk, M., Freedman, F., Kitagawa, H., Larson, V., Lock, A., Mailhot, J., Masson, V., Park, S., Pleim, J., Söderberg, S., Weng, W., and Zampieri, M. (2011). Evaluation of the diurnal cycle in the atmospheric boundary layer over land as represented by a variety of single-column models: The second GABLS experiment. *Boundary-Layer Meteorol*, 140(2):177–206.

Taylor, P. A. and Teunissen, H. (1987). The askervein hill project: overview and background data. *Boundary-Layer Meteorol*, 39:15–39.

Taylor, P. A., Walmsley, J. L., and Salmon, J. R. (1983). A simple model of neutrally stratified boundary-layer flow over real terrain incorporating wavenumber-dependent scaling. *Boundary-Layer Meteorol*, 26(2):169–189.

Tewari, M., Kusaka, H., Chen, F., Coirier, W. J., Kim, S., Wyszogrodzki, A. A., and Warner, T. T. (2010). Impact of coupling a microscale computational fluid dynamics model with a mesoscale model on urban scale contaminant transport and dispersion. *Atmospheric Research*, 96(4):656–664.

Texier, O., Bezault, C., Girard, N., Houbart, J.-C., and Pham, S. (2012). Results of integration of atmospheric stability in wind power assessment through cfd modeling. In *Proceedings: EWEA 2012 - European Wind Energy Conference & Exhibition, Copenhagen, Denmark*.

Thanh, C. V., Yasunobu, A., and Takashi, A. (2002). A k–ϵ turbulence closure model for the atmospheric boundary layer including urban canopy. *Boundary-Layer Meteorol*, 102(3):459–490.

Türk, M. and Emeis, S. (2010). The dependence of offshore turbulence intensity on wind speed. *J Wind Eng Ind Aerod*, 98(8–9):466–471.

Troen, I., Mortensen, N. G., and Lundtang-Petersen, E. (1987). *WAsP - Wind Atlas analysis and Application Program. User's Guide. Release 1.0*. Risø National Laboratory.

Troen, I. and Petersen, E. L. (1989). *European Wind Atlas*. Risø National Laboratory, Roskilde.

Undheim, O., Andersson, H. I., and Berge, E. (2006). Non-linear, microscale modelling of the flow over askervein hill. *Boundary-Layer Meteorol*, 120(3):477–495.

van Ulden, A. P. and Holtslag, A. A. M. (1980). The wind at heights between 10m and 200m in comparison with the geostrophic wind. In E. C. commission, L., editor, *J Proc Sem Radioactive Releases*, volume 1, pages 83–92.

Vendel, F., Lamaison, G., Soulhac, L., Volta, P., Donnat, L., Duclaux, O., and Puel, C. (2010). Modelling diabatic atmopsheric boundary layer using a rans cfd code with a k-epsilon turbulence closure. In *Proceedings: 13th Conference on Harmonisation within Atmospheric Dispersion Modelling for Regulatory Purposes, Paris, France.*

Wallace, J. M. and Hobbs, P. V. (2006). *Atmospheric science: an introductory survey*. Academic Press.

Walmsley, J. L., Taylor, P. A., and Keith, T. (1986). A simple model of neutrally stratified boundary-layer flow over complex terrain with surface roughness modulations (MS3DJH/3R). *Boundary-Layer Meteorol*, 36(1-2):157–186.

Wan, F. and Porté-Agel, F. (2011). Large-eddy simulation of stably-stratified flow over a steep hill. *Boundary-Layer Meteorol*, 138:367–384.

Wang, Y., Basu, S., and Manuel, L. (2013). Coupled mesoscale-large-eddy modeling of realistic stable boundary layer turbulence. Technical Report 1307.2484.

Westerhellweg, A., Cañadillas, B., Kinder, F., and Neumann, T. (2013). Wind flow conditions in offshore wind farms: Validation and application of a CFD wake model. 3(1):27–34.

Wharton, S., Lundquist, J. K., and Marjanovi, N. (2012). Synergistic effects of turbine wakes and atmospheric stability on power production at an onshore wind farm. Technical Report LLNL-TR-524756.

Wichmann, M. and Schaller, E. (1986). On the determination of the closure parameters in higher-order closure models. *Boundary-Layer Meteorol*, 37(4):323–341.

Wilcox, D. C. (1998). *Turbulence Modeling for CFD*. Dcw Industries, Incorporated, 2nd edition.

Wyngaard, J. C. (1975). Modeling the planetary boundary layer Ǔ extension to the stable case. *Boundary-Layer Meteorol*, 9(4):441–460.

Wyngaard, J. C., Coté, O. R., and Rao, K. S. (1974). Modeling the atmospheric boundary layer. *Adv. Geophys.*, 7(18A):193–211.

Yamada, T. (2004). Merging cfd and atmospheric modeling capabilities to simulate airflows and dispersion in urban areas. *Int J Comput Fluid D*, 13:329–341.

Yamada, T. and Koike, K. (2011). Downscaling mesoscale meteorological models for computational wind engineering applications. *J Wind Eng Ind Aerod*, 99(4):199–216.

Yang, W., Quan, Y., Jin, X., Tamura, Y., and Gu, M. (2008). Influences of equilibrium atmosphere boundary layer and turbulence parameter on wind loads of low-rise buildings. *J Wind Eng Ind Aerod*, 96(10–11):2080–2092.

Zhang, J. (2000). Numerical simulation of 2D square driven cavity using fourth order compact finite difference schemes. *Comput Math Appl*, 45(1–3):43–52.

Zilitinkevich, S. S. and Esau, I. N. (2002). On integral measures of the neutral barotropic planetary boundary layer. *Boundary-Layer Meteorol*, 104(3):371–379.